Mission analysis of space-based telescopes to detect impacting near-Earth objects

Master Thesis

Olga Ramírez Torralba

Technische Universiteit Delft

TU Delft

MISSION ANALYSIS OF SPACE-BASED TELESCOPES TO DETECT IMPACTING NEAR-EARTH OBJECTS

Master Thesis

by

Olga Ramírez Torralba

Master of Science

in Aerospace Engineering

at the Delft University of Technology

to be defended publicly on Thursday March 5, 2020 at 1 PM.

Student number:	4731808	
Project duration:	May 20, 2019 – January 22, 2020	
Supervisors:	Dr. M. J. Heiligers,	TU Delft, supervisor
	Dr. R. Jehn,	European Space Agency, supervisor
Thesis committee:	Dr. Ir. P.N.A.M. Visser,	Committee chair
	Dr. M. J. Heiligers,	Supervisor
	Dr. S. Speretta,	External examinator
	Dr. D. Koschny,	Additional

An electronic version of this thesis is available at http://repository.tudelft.nl/.

TU Delft Delft University of Technology

PREFACE

Dear family, friends and colleagues,

it seems that I finally managed to do what once seemed to be impossible. After seven years of hard work and sacrifice, I am about to graduate. But don't get me wrong, I do not regret any single day. I cannot be prouder and more satisfied with all the knowledge and experience that I have gathered these past years of my life. While I was getting my bachelor's degree in aerospace engineering at the Universitat Politècnica de Catalunya, I worked on building self-discipline. When I was a master's student at the Delft University of Technology, I learned about the importance of being confident with your own work and ideas, but also trusting your team members. My last year at the European Space Operations Centre not only taught me about work ethic, but also assured me how cool space is, how little I still know about it, and how glad I am that I decided to study space exploration. And lastly, while I am writing this little thank-you note, I realised how I should have spent a teensy bit more time learning how to express gratitude. Well, it is too late now, but I will give it a try.

First, I would like to thank my parents, who fully supported me ~~these past years~~ my whole life, and my older brother, who was the person who told me to study aerospace engineering because "it was pretty fun". I feel very lucky to have been born in this family of engineers, who doesn't care how many masters, degrees and PhDs we have in total, because we still need our 2+ sweet hours to finish a simple 'Escape Room' board-game. Second, I would also like to thank my dear NEO team at ESOC, the so-called Planetary Defenders: Toni Santana, Michael Frühauf, Pablo Ramírez, Detlef Koschny, and my supervisor 'El Jefe' Rüdiger Jehn, who are probably the only people in this world who get excited when Earth is under attack (just kidding, of course). Although I am not an official member of the NEO team anymore, I know that you will always welcome me with a beer (or a few). I would also like to mention my 'Space Defenders' friends, the cuddly Miss Sophie and the spontaneous Michi, who I miss terribly and were always there for me with a good cup of tea (ready to spill). And last but definitely not least, I would like to express my gratitude to my amazing supervisor at TU Delft, Jeannette Heiligers, who not only made this thesis possible with her great ideas and insight, but was always available for me when I was worried about something and was in desperate need for advice. Now that I am about to start my career as an engineer, it is very comforting and encouraging to know that I have two incredible mentors, my supervisor and my mom, who are both very successful women in science and engineering, and also wonderful people that I aspire to be.

Olga Ramírez Torralba

Home, Barcelona, January 2020

ABSTRACT

In addition to the Sun and the eight known planets, our Solar System consists of countless smaller bodies, such as comets and asteroids, ranging from a few micrometres to hundreds of kilometres in size. The so-called near-Earth objects (NEOs) pertain to a minor population of small bodies that make threatening close approaches to Earth due to planetary perturbations. By definition, a NEO is a name given to any asteroid or comet with a perihelion distance of 1.3 au or less.

The major concern with NEOs is that they are a potential danger to life on Earth. From the kilometre-size Chicxulub asteroid impactor that killed the dinosaurs and wiped out almost 80% of life on the planet approximately 65 million years ago, to the metre-size Chelyabinsk asteroid impactor that injured nearly 1 500 people on 15 February 2013, plenty of evidence has confirmed the collisional hazard to Earth of NEOs. Recognising this threat, many projects have been developed worldwide with the aim of detecting these potential impactors, most of which are focused on ground-based surveys. However, ~20% of the Earth-threatening NEOs are estimated to be approaching us from the day-side, and are thus very difficult to detect using ground surveys. In order to observe such objects, space-based survey systems are the only solution. Over the last decade, several space-based capabilities have emerged in an effort to discover and catalogue NEOs in order to better quantify their risk of impact, yet little research has gone into dealing with the imminent-impacting NEOs.

The aim of this thesis is to design a space mission that places a telescope in-orbit in order to detect and provide warning for Earth-impacting NEOs, down to a size comparable to the Chelyabinsk asteroid, and also contribute to existing ground-based NEO surveys by scanning the region close to the Sun-Earth line, that ground surveys cannot reach. To this aim, two mission candidates envisioned in the preliminary literature study are designed in the same dynamical framework as the Earth-threatening NEOs, *i.e.*, the elliptic restricted three-body problem (ER3BP). The first mission candidate consists of a halo orbit about the artificial equilibrium point sub-L_1 of the Sun-Earth system, which is displaced with respect to the classical libration point L_1, along the Sun-Earth direction towards the Sun, through to the use of solar-sail propulsion. The second mission candidate consists of three periodic orbits about the libration points L_3, L_4 and L_5 of the Sun-Venus system. Then, the performance of both a visible and an infrared (IR) space-based telescope used in each of these two mission candidates is estimated by means of a space-based NEO survey simulation tool, which has been developed throughout this thesis.

Several scenarios of sky surveys are simulated in order to select the most suitable space-based NEO survey system based on a trade-off between obtained detection rates and warning times. For surveying Earth impacting NEOs down to 20 m in diameter, an IR space-based telescope placed at the Sun-Earth solar-sail displaced L_1 point is concluded to be the best option, mainly due to the long warning times obtained. Moreover, a space-based telescope surveying at IR wavelengths is able to contribute more to existing ground-based

NEO surveys, as it is able to detect NEOs that are missed by ground telescopes with enough warning time before impact. Finally, a preliminary mission analysis is performed in order to determine a time-optimal, solar-sail propelled transfer trajectory from Earth's vicinity to the Sun-Earth sub$-L_1$ region, which assumes a ride-share launch on ESA's Euclid mission to the Sun-Earth L_2 point and takes 427.25 days.

The work conducted in this thesis is key to solving the global concern with NEOs and is expected to fill the gap in our current understanding of space-based NEO surveys since, as of today, there is no sufficiently realistic proposal that focuses on discovering the very dangerous and imminent-impacting NEOs.

Contents

List of Figures

List of Tables

NOMENCLATURE

List of abbreviations

Abbreviation	Description
AEP	Artificial Equilibrium Point
CR3BP	Circular, Restricted, Three-Body Problem
CSS	Catalina Sky Survey
ER3BP	Elliptic, Restricted, Three-Body Problem
ESA	European Space Agency
ESOC	European Space Operations Centre
IEO	Inner-Earth Object
IM	Invariant Manifold
IR	Infrared
LPO	Libration Point Orbit
NEATM	Near-Earth Asteroid Thermal Model
NEO	Near-Earth Object
NEOCam	Near-Earth Object Camera
NEOPOP	Near-Earth Object Population Observation Program
PHA	Potentially Hazardous Asteroid
SDT	Science Definition Team
SE	Sun-Earth
SNR	Signal-to-Noise Ratio
SODA	System of Observation of Day-time Asteroids

SSA	Space Situational Awareness
SSO	Sun-Synchronous Orbit
STM	Standard Thermal Model
SV	Sun-Venus
TIR	Thermal infrared
VIS	Visible
WISE	Wide-field Infrared Survey Explorer

List of Roman symbols

Symbol	Description	Unit
D	Diameter	km
e	Eccentricity	-
f_{zod}	Correction factor for the zodiacal light noise	-
H	Absolute magnitude	-
m	Apparent magnitude	-
$\hat{\mathbf{n}}$	Solar-sail normal vector	-
N	Number of time steps	-
p_v	Visual albedo	-
$\mathbf{R}_1$	Position vector of the body with respect to the primary body in the ER3BP	-
r	Heliocentric distance	au
R_0	Heliocentric distance of the observer	au
X, Y, Z	Position coordinates in the pulsating-rotating reference frame	-
x, y, z	Position coordinates in the synodic reference frame	-
Z_0	Height above the ecliptic of the observer	au

List of Greek symbols

Symbol	Description	Unit
α	Phase angle	rad
α_s	Solar-sail cone angle	rad
β	Solar-sail lightness number	-
Δ	Geocentric distance	au
δ_s	Solar-sail clock angle	rad
η	Beaming parameter	-
λ	Wavelength	μm
$\lambda_\oplus, \beta_\oplus$	Geocentric ecliptic coordinates	rad
μ	Mass parameter	-
Ω_E	Effective potential function in the ER3BP	

Other notation, superscripts and subscripts

Symbol	Description
$\ddot{\square}$	Second-time derivative
$\dot{\square}$	First-time derivative
∇f	Gradient of the scalar field f
$\oplus$	From Earth
$\square'$	First derivative with respect to true anomaly
$\square''$	Second derivative with respect to true anomaly
$\square_0$	Initial condition

List of physical constants

Symbol	Description	Value
au	Astronomical unit	149 597 870.7 km

1

INTRODUCTION

This chapter briefly summarises the main work conducted in the literature study for this thesis. First, Section 1.1 describes the background and motivation behind the chosen topic. Then, Section 1.2 provides a good outline of the state-of-the-art space missions whose aim is to detect and track near-Earth objects (NEOs) using space-based surveys. Section 1.3 focuses on explaining the research work, relevance and novelty of this thesis. Section 1.4 formulates the research aim and research questions, as well as the sub-aims and sub-questions required to answer the research aim. The chapter ends with an outline of this thesis report in Section 1.5.

1.1. THE THREAT OF NEAR-EARTH OBJECTS

On 15 February 2013, a small asteroid of about 20 m entered the atmosphere over Chelyabinsk and exploded about 30 km above the city. The explosion unleashed an energy equal to 20 or 30 times the energy released in the Hiroshima atomic explosion and the resulting shock wave shattered many windows, injuring nearly 1 500 people. This asteroid pertains to a minor population of small bodies in our Solar System, the so-called NEOs, that make threatening close approaches to Earth due to planetary perturbations. By definition, a NEO is a name given to any asteroid or comet with a perihelion distance of 1.3 au or less (Lissauer and De Pater, 2013).

The major concern with near-Earth objects (NEOs) is that they are a potential danger to life on Earth. From the kilometre-size Chicxulub asteroid impactor that killed the dinosaurs and wiped out almost 80% of life on the planet approximately 65 million years ago, to the metre-size Chelyabinsk asteroid impactor, plenty of evidence has confirmed the collisional hazard to Earth of NEOs. Recognising this threat, many projects have been developed worldwide with the aim of detecting these potential impactors. To date, most efforts have focused on ground-based surveys carried out by 0.5 to 2 m telescopes operating at visible wavelengths,

such as the Catalina Sky Survey (CSS).

Current estimates agree that these surveys have discovered approximately 90% of NEOs larger than 1 km, ~30% of NEOs larger than 140 m and only ≤1% of those objects of the scale of the Tunguska and Chelyabinsk impactors (~20–50 m)(Stokes et al., 2017), and thus, a large fraction of the total population of existing NEOs is still unknown. For this reason, in 2005, the U.S. Congress authorised NASA to generate a catalogue that is more than 90% complete for all NEOs larger than 140 m by the year 2020 (Stokes et al., 2017). To this aim, NASA commissioned a Science Definition Team (SDT) in order to study the feasibility of extending the search of ground-based surveys for those NEOs with diameters down to 140 m. In the 2017 SDT report, they concluded that the satisfaction of this cataloguing objective required space-based search system(s), consisting of thermal infrared (TIR) and visible (VIS) telescopes.

While NASA is aiming at finding NEOs larger than 140 m, the Planetary Defence Office of the European Space Agency (ESA) has set its objectives to warn for close approaches or potential impact threats of smaller NEOs. To this aim, the activities on ground are focused on the deployment of the Flyeye telescope, which is ESA's first NEO survey telescope, designed to search for very small and faint NEOs that are expected to collide with Earth. Unfortunately, many of these Earth impactors will remain undiscovered before impact because they approach us from the day-side, and are thus very difficult to observe using ground-based telescopes. This was actually the case for the Chelyabinsk asteroid, which, despite our vast network of ground-based telescopes, remained completely unnoticed before the unfortunate event because it approached Earth from a direction very close to the Sun-Earth line. Literature estimates that approximately 15.6–19.9% of Earth impacting NEOs are approaching us from the Sun (Ramirez Torralba et al., 2019)(Farnocchia et al., 2012). In order to observe such objects, space-based survey systems are the only solution.

1.2. STATE-OF-THE-ART SPACE-BASED SURVEYS OF NEAR-EARTH OBJECTS

Space-based surveys offer a clear advantage over ground-based surveys due to their unique possibility to look back towards the Earth, and thus monitor those objects coming from the Sun. However, as of January 2020, there are only two space-based telescopes in-orbit with the aim of surveying NEOs.

First, NASA's Wide-field Infrared Survey Explorer (WISE) spacecraft was launched into an Earth Sun-synchronous orbit (SSO) on 14 December 2009 with the primary goal of imaging the entire sky at infrared (IR) wavelengths. When the frozen hydrogen, which was used to cool the telescope, was depleted in September 2010, the WISE mission continued the survey as NEOWISE for an additional four months in order to search for asteroids. Then, in September 2013, the mission was reactivated again with the primary goal of scanning the sky for NEOs, and more specifically those that could impact Earth. As of mid-December 2019, NEOWISE has characterised 1 069 NEOs and 185 comets (Mainzer et al., 2011a).

Second, the Canadian spacecraft Near-Earth Object Surveillance Satellite (NEOSSat) was launched into orbit as a secondary payload on 25 February 2013. This microsatellite has a 15 cm aperture optical telescope onboard, whose aim is to discover inner-Earth objects (IEOs), *i.e.*, those NEOs that are found orbiting the Sun within Earth's orbit. However, as the spacecraft was put into a very low Earth SSO, the area within a

solar elongation (the Sun-observer-object angle) of 45° is inaccessible. In addition, the small aperture of the telescope only allows the detection of rather bright asteroids (Abbasi et al., 2019). As of March 2019, NEOSSat operations continue into its fifth year and, so far, it has only performed astrometric observations of known NEOs.

In addition to those space missions that have already been launched, there are several proposals for space missions with the aim of detecting or tracking NEOs in literature. Among all these proposals, there are two that are still active and currently under development: NASA's Near-Earth Object Camera (NEOCam) and the Russian System of Observation of Day-time asteroids (SODA).

First, the NEOCam project is a proposed 0.5 m space-based IR telescope placed at the Sun-Earth L_1 Lagrangian point, which is designed to discover and characterise most of the potentially hazardous asteroids (PHAs) in the Solar System. The mission concept emerged from the success of WISE in discovering NEOs at IR wavelengths, and has been submitted to NASA's Discovery program in 2005, 2010 and 2015 (Mainzer et al., 2015). As of May 2019, this project is still under development but it is expected to be launched in 2024 (Milam et al., 2019a).

Then, since 2015, Shustov et al. (2019) have been working on the SODA project, whose aim is to detect and monitor "almost all" bodies larger than 10 m approaching Earth at distances less than 10^6 km from the Sun direction. The proposed SODA mission consists of one or two spacecraft placed in a halo orbit around the Lagrangian point L_1 of the Sun-Earth system and is equipped with three 30 cm space-based VIS telescopes each in order to increase the efficiency of the survey and for redundancy reasons (Shustov et al., 2019).

1.3. RESEARCH WORK, RELEVANCE AND NOVELTY

State-of-the-art space missions and proposals are focused on the discovery of NEOs and IEOs in order to catalogue them and, thus, better quantify their risk of impact. With the exception of the SODA project, there is no sufficiently realistic proposal that focuses on discovering imminent-impacting NEOs. Moreover, although SODA states that, in the case of finding a potential impactor, SODA is expected to be able to determine the atmospheric entry point and ensure warning times of at least four hours (Shustov et al., 2019), simulations or results that confirm these statements have not been found.

In this research, a space-based NEO survey system is designed with the aim of providing warning for Earth impactors. By means of a space-based NEO observation tool, that is developed throughout the research work, the performance of each space-based survey system is determined. The performance is defined in terms of the following results: detection rate (*i.e.*, number of observed and missed impacts), time between observation and impact (*i.e.*, warning time) and observed and missed impactors as a function of absolute magnitude and size. While NASA is aiming at finding NEOs larger than 140 m (Stokes et al., 2017)(Mainzer et al., 2015), this research work is focused on detecting and providing warning for potential impact threats of even smaller NEOs in the range of 22–140 m in diameter. To this aim, a synthetic population of Earth impactors, that is based on the accurate NEO population model developed by Granvik et al. (2018), is used in the simulations.

During the literature study, a total of four different mission candidates were considered and discussed,

and two potential mission candidates were selected (Ramirez Torralba, Olga, 2019). The first mission candidate consists of three periodic orbits about the Lagrange libration points L_3, L_4 and L_5 of the Sun-Venus system. The second one consists of a halo orbit about the artificial equilibrium point (AEP) sub-L_1 of the Sun-Earth system, which is displaced with respect to the classical libration point L_1, along the Sun-Earth direction towards the Sun, through the use of solar-sail propulsion. It is important to highlight that the use of a solar sail in the Sun-Earth L_1 region in order to displace the AEP towards the Sun and increase the warning time has never been envisioned for NEO detection. Therefore, it is very interesting to study how the performance of this space-based survey system improves with respect to the classical L_1 point, which is the proposed orbit location for both NEOCam and SODA projects.

Regarding the waveband of the space-based telescope, there is still an on-going debate about which one is best for surveying NEOs. In general, IR detectors are superior than visible ones because NEOs are easier to be detected in this region of the electromagnetic region (Müller, 2012). In addition, they allow characterisation of the size of the objects, which is a key parameter when determining the impact threat (Mainzer et al., 2011b). However, the main disadvantage of IR detectors is that they must be cooled to cryogenic temperatures in order to effectively work in this domain. This implies that they require some kind of on-board cooling system, which increases the payload mass of the spacecraft and/or limits the lifetime of the mission, if an active cooling system is necessary (Rodriguez, 2017). In the most recent 2017 NEO SDT report, Stokes et al. (2017) concluded that the best cataloguing capability (NEO characterisation) can be achieved by using an IR 0.5-m telescope and the best warning capability (NEO detection) can be achieved by using a visible 0.5-m telescope. For these reasons, it was not possible to reach a conclusion about which wavelength band is better during the literature study (Ramirez Torralba, Olga, 2019), and both IR and visible telescopes are considered. This comparison is key to put an end to this never-ending debate about which waveband is best for surveying impacting NEOs: the visible waveband, as stated by the SODA project, or the IR waveband, as stated by the NEOCam project.

Therefore, two different mission candidates and two wavelength bands are considered in the research work, and thus, a total of four space-based survey systems are modelled, evaluated and compared to make a decision on which is the most suitable space-based NEO survey system.

1.4. RESEARCH AIM AND RESEARCH QUESTIONS

The aim of this research is to design a space mission that places a telescope in-orbit in order to detect and provide warning for NEOs on a collision course with Earth, by determining the performance of both a VIS and TIR space-based telescope used in two mission candidates, and performing a mission analysis in order to determine a feasible transfer trajectory to such orbits.

The main research question is therefore defined as:

What is the best location and what are the best characteristics for a space-based telescope with the aim of efficiently detecting and providing warning for NEOs that are going to impact Earth?

The development of such a space-based survey system raises the following three sub-aims, each with its

own sub-question(s) that will be answered in this thesis:

- To select the best orbit location between a Venus-trailing orbit constellation and a halo orbit about the sub-L_1 of the Sun-Earth system.

    1. *How do the two orbit locations perform and compare in terms of NEO detection rate and warning time?*

- To determine the performance of a visible and an IR space-based telescope in providing warning for near-Earth objects.

    2. *Which wavelength band provides the longest warning time for impacting NEOs and/or largest detection rates?*

- To determine the performance of a NEO survey system consisting of both space- and ground-based surveys.

    3. *How does the combination of space- and ground-based survey systems perform in terms of NEO detection rate and warning time?*
    4. *How does the performance of the NEO survey system improve with multiple space-based telescopes?*

- To determine a feasible transfer trajectory in order to launch the selected space-based survey system into the operational orbit from Earth.

    5. *What transfer scheme from Earth results in a feasible trajectory to the chosen operational orbit?*

1.5. REPORT OUTLINE

This thesis report is organised as follows. First, Chapter 2 consists of the main content of the research, where all work conducted in this master thesis is discussed and presented in the form of a draft journal article. This draft article starts with an abstract and a brief introduction of the work, where the relevance and importance of the outcome are also explained. Next, a section on the dynamical models is included in order to define the dynamical framework of the study. Then, the following two sections are focused on the orbit design of the two mission candidates for the space-based telescope, a halo orbit around the sub$-L_1$ of the Sun-Earth system and vertical Lyapunov orbits around the L_3, L_4 and L_5 points of the Sun-Venus system, respectively. The space-based survey model that is implemented and used in the simulations is presented in the next section, which includes the definition of all relevant parameters, models and overall theoretical framework. Using this space-based survey model, the performance of each space-based survey system in providing warning for imminent Earth impactors is then determined and compared to existing ground-based surveys. Once the operational orbit of the space-based telescope is selected, the next section aims at finding a time-optimal, solar-sail propelled transfer trajectory from Earth's vicinity to the targeted orbit. The draft article ends with the conclusions derived in the main research work. Right after the journal article, this report includes another

conclusions section in Chapter 3, which answers the research questions defined in Section 1.4, and elaborates on the recommendations and future work. Lastly, at the end of this thesis report, an appendix is included related to the verification and validation of the models and algorithms that have been used throughout the research work.

2

Journal Article

Mission analysis of space-based telescopes to detect impacting near-Earth objects

Olga Ramírez Torralba
Astrodynamics and Space Missions, Delft University of Technology, 2629 HS, Delft, The Netherlands

Recognising the threat of near-Earth objects (NEOs) to life on Earth, many projects have been developed worldwide with the aim of detecting potential impactors, most of which are focused on ground-based surveys. However, ~20% of the Earth-threatening NEOs are estimated to be approaching us from the day-side, and are thus very difficult to detect using ground surveys. Over the last decade, several space-based capabilities have emerged in an effort to discover and catalogue NEOs in order to better quantify their risk of impact, yet little research has gone into dealing with imminent-impacting NEOs. The aim of this paper is to design a space mission that places a telescope in-orbit in order to detect and provide warning for Earth-impacting NEOs down to 20 m in size, by determining the performance of both a visible and an infrared (IR) space-based telescope used in two mission candidates. The first mission candidate consists of a halo orbit about the artificial equilibrium point sub-L_1 of the Sun-Earth (SE) system, which is displaced with respect to the classical L_1 point, along the SE direction towards the Sun, through the use of solar-sail propulsion. As second mission candidate, three vertical Lyapunov orbits about the libration points L_3, L_4 and L_5 of the Sun-Venus system are considered. A trade-off between detection rates and warning times is conducted to determine the most suitable space-based NEO survey system. It is concluded that an IR space-based telescope placed at the SE solar-sail displaced L_1 point is the best option because of the long warning times obtained and the beneficial contribution to existing ground-based NEO surveys. A preliminary mission analysis is also conducted to determine a solar-sail propelled transfer trajectory to the SE sub$-L_1$ region, assuming a ride-share launch on ESA's Euclid mission.

Nomenclature

Abbreviation

AEP	=	Artificial Equilibrium Point
CR3BP	=	Circular Restricted Three-Body Problem
ER3BP	=	Elliptic Restricted Three-Body Problem
FOR	=	Field of Regard

FOV = Field of View

IEO = Inner-Earth Object

IR = Infrared

LPO = Libration Point Orbit

NEATM = Near-Earth Asteroid Thermal Model

NEO = Near-Earth Object

QE = Quantum Efficiency

SE = Sun-Earth

SNR = Signal-to-Noise Ratio

SV = Sun-Venus

STM = Standard Thermal Model

TIR = Thermal infrared

TOF = Time of flight

VIS = Visible

Roman symbols

A_{eff} = Effective aperture area of the detector, m^2

A_x, A_z = In-plane and out-of-plane amplitudes of the periodic orbit

$\mathbf{a}_s$ = Solar-sail acceleration, ms^{-2}

B_e = Signal of the background noise, e^-

e = Eccentricity

F_A, F_B = Irradiance of the object and the background at the detector, $\text{Wm}^{-2}\text{m}^{-1}$

f = True anomaly, rad

H = Absolute magnitude

k_{dark} = Dark current noise, e^-s^{-1}

k_{read} = Readout noise, e^-

m = Apparent magnitude

m_1, m_2 = Mass of the primary and secondary bodies of the restricted three-body problem

$\hat{\mathbf{n}}$ = Solar-sail normal vector

$\mathbf{p}_i$,$\mathbf{P}_i$ = Decision vector at node i in the CR3BP and the ER3BP

p_{px} = Percentage of light within the centre pixel

p_v = Visual albedo

r = Distance between the object and the Sun, au

$\mathbf{R}$ = Position vector of the solar-sail spacecraft with respect to the barycentre in the ER3BP

$\mathbf{r}$ = Position vector of the solar-sail spacecraft with respect to the barycentre in the CR3BP

$\mathbf{R}_i$ = Position vector of the solar-sail spacecraft with respect to the i body in the ER3BP

$\mathbf{r}_i$ = Position vector of the solar-sail spacecraft with respect to the i body in the CR3BP

$\mathrm{S_e}$ = Signal of the object, $\mathrm{e^-}$

s_1, s_2 = Frequencies of the long- and short-period motion of the linear system

t = Dimensionless time

t_{exp} = Exposure time, s

t_{euclid} = Time that the solar-sail spacecraft travels together with Euclid

U = Effective potential function in the CR3BP

W_α, W_δ = Weights of the sail attitude terms in the weight matrix

x, y, z = Position coordinates in the synodic reference frame

X, Y, Z = Position coordinates in the pulsating-rotating reference frame

Greek symbols

α = Phase angle, rad

α_s, δ_s = Solar-sail cone and clock angles, rad

β = Solar-sail lightness number

Δ = Distance between the object and the observer, au

ϵ_I = Infeasibility of the transfer trajectory

ϵ_R, ϵ_V = Error in dimensionless position and velocity

η = Beaming parameter

λ_i = Eigenvalue i

λ = Wavelength, μm

μ = Mass parameter

σ = Solar-sail loading, $\mathrm{gm^{-2}}$

ρ = Semi-latus rectum

τ = Optical transmission

τ_f = Insertion point along the target halo orbit

$\Phi(t_f, t_0)$ = State transition matrix

Ω_E = Effective potential function in the ER3BP

ω_{xy}, ω_z = In-plane and out-of-plane frequencies of the periodic orbit

ω = Angular velocity of the synodic reference frame, $\mathrm{rads^{-1}}$

Other notation, superscripts and subscripts

$\dot{\square}$, $\ddot{\square}$	=	First- and second-time derivatives
$\square'$, $\square''$	=	First and second derivatives with respect to true anomaly
$\tilde{\square}$	=	Motion with respect to the libration point
$\square_0$, $\square_f$	=	Initial and final segments of the near-feasible transfer trajectory
∇f	=	Gradient of the scalar field f
A_i,B_i,C_i,S_i	=	Constant coefficients

I. Introduction

The major concern with near-Earth objects (NEOs) is that they are a potential danger to life on Earth. From the kilometre-size Chicxulub asteroid impactor that killed the dinosaurs and wiped out almost 80% of life on the planet approximately 65 million years ago, to the metre-size Chelyabinsk asteroid impactor that injured nearly 1 500 people on 15 February 2013, plenty of evidence has confirmed the collisional hazard of NEOs to Earth. Recognising this threat, many projects have been developed worldwide with the aim of detecting these potential impactors. To date, most efforts have focused on ground-based surveys with optical telescopes, such as the Catalina Sky Survey, which have successfully discovered approximately 90% of NEOs larger than 1 km and ~30% of NEOs larger than 140 m [1]. However, approximately 15.6–19.9% of Earth-threatening NEOs are estimated to be approaching Earth directly from the day-side [2][3], and are thus very difficult to detect using ground surveys.

Space-based surveys offer a clear advantage over ground-based surveys due to their unique possibility to look back towards the Earth, and thus monitor those objects coming from the Sun with enough time before impact. As of January 2020, there are only two space-based telescopes in-orbit with the aim of surveying NEOs: NASA's NEOWISE mission, whose aim is to scan the sky at infrared (IR) wavelengths in order to search for Earth-threatening NEOs [4], and the Canadian spacecraft NEOSSat, which was launched in 2013 with a 0.15 m optical telescope onboard, with the aim of discovering inner-Earth objects (IEOs). In addition to these space missions that are already operational, similar proposals can be found in literature, such as NASA's NEOCam and the Russian SODA project. The NEOCam project is a proposed 0.5 m space-based IR telescope placed at the Sun-Earth (SE) L_1 point, which is designed to discover and characterise most of the potentially hazardous asteroids larger than 140 m [5][6]. The SODA project also proposes placing one or two spacecraft at the SE L_1 point, but equipped with three 30 cm space-based visible (VIS) telescopes with the aim of detecting and monitoring "almost all" bodies larger than 10 m approaching Earth from the day-side [7].

State-of-the-art space missions and proposals are focused on the discovery of NEOs and IEOs in order to catalogue them and, thus, better quantify their risk of impact. With the exception of the SODA project, there is no sufficiently realistic proposal that focuses on discovering imminent-impacting NEOs with enough time in advance of impact. In

this paper, a space-based survey system is designed with the aim of efficiently detecting and providing warning for Earth-impacting NEOs, in the range of 22–140 m in diameter, as well as contributing to the observations obtained by existing ground-based surveys. To this aim, two mission candidates are envisioned.

The first mission candidate consists of a halo orbit about the artificial equilibrium point (AEP) sub$-L_1$ of the Sun-Earth system, which is displaced with respect to the classical libration point L_1, along the Sun-Earth direction towards the Sun, through the use of solar-sail propulsion. Solar sails are a propellant-less form of spacecraft propulsion system, where sunlight exerts a pressure on a large mirror-like structure, generating a force that can be controlled by the sail's orientation and parameters. The concept of solar sailing was first envisioned during the 1920s but did not became a reality until 2010 with JAXA's IKAROS [8] and NASA's NanoSail D2 missions [9]. By using the continuous acceleration generated by the solar sail, it is possible to obtain an orbit around an equilibrium point closer to the Sun than the classical L_1 point. The use of solar sails in the Sun-Earth sub$-L_1$ region has never been envisioned for NEO detection, but is expected to significantly increase the warning time of the observed impacting NEOs with respect to the classical L_1 point, which is the proposed location for both NEOCam and SODA projects.

The second mission candidate is designed in the Sun-Venus (SV) system. The work by [5] suggests to place the space-based telescope into a Venus-trailing orbit as it will allow to observe the IEOs when they are closest to the Sun and at their brightest. The idea in this paper is to place three space-based telescopes into periodic orbits about the Lagrange libration points L_3, L_4 and L_5 of the SV system, instead of only one in a Venus-trailing orbit, such that there will always be one telescope between the Earth and the Sun at an advantageous location to discover approaching NEOs.

In addition to these two mission candidates, both the visible and thermal infrared (TIR) wavebands are considered for the space-based telescope. In general, IR detectors are superior to visible ones because NEOs are easier to be detected in this region of the electromagnetic region [10], and they allow characterisation of the size of the objects, which is a key parameter when determining the impact threat [11]. However, in the most recent 2017 NEO SDT report [1], it was concluded that, while the best cataloguing capability is achieved by a 0.5 m IR telescope, the best warning capability is achieved by a 0.5 m VIS telescope.

Therefore, two different orbit locations and two wavelength bands are considered in this paper, and thus, a total of four space-based survey systems are modelled. The performance of each space-based survey system in providing warning for impacting NEOs is then determined in terms of detection rate and warning time, and compared to the performance obtained by existing ground-based surveys. Ultimately, the best NEO survey system is determined by performing a trade-off between obtained detection rates and warning times, required number of space-based telescopes and integration with existing ground-based surveys. Once the most suitable mission candidate is selected, a preliminary mission analysis is performed in order to determine a feasible transfer trajectory from Earth's vicinity to the chosen operational orbit.

This paper is organised as follows: first, Section II describes the dynamical framework of the study. The design of

the orbits for both mission candidates, *i.e.*, a halo orbit around the sub$-L_1$ of the SE system and vertical Lyapunov orbits around the L_3, L_4 and L_5 points of the SV system, is explained in Sec. III and Sec. IV, respectively. Then, Section V describes the space-based survey model that is implemented and used in the simulations of the sky surveys, and defines all relevant parameters for the space-based telescopes in both wavebands. Using this space-based survey model, the performance of each space-based survey system in providing warning for imminent Earth impactors is determined in Sec. VI, and the best NEO survey system consisting of both space- and ground-based surveys is identified. Once the operational orbit of the space-based telescope is selected, Section VII performs a preliminary mission analysis with the aim of finding a time-optimal, solar-sail propelled transfer trajectory from Earth's vicinity to the targeted operational orbit, assuming a ride-share launch with ESA's Euclid spacecraft towards the Sun-Earth L_2 region. Lastly, the main conclusions derived in the paper are presented in Sec. VIII.

II. Dynamical Models

This section describes the dynamical framework that is used in this paper. First, the circular restricted three-body problem (CR3BP) is defined in Sec. II.A. Then, Section II.B presents the solar-sail model that is considered in this work to represent the performance of the solar sail. The section ends with the description of the elliptic restricted three-body problem (ER3BP) in Sec. II.C.

A. Circular Restricted Three-Body Problem

The CR3BP describes the motion of a body with negligible mass (*i.e.*, the solar-sail spacecraft), under the gravitational influence of two much larger primary bodies, with masses m_1 (the Sun) and m_2 (the planet, *i.e.*, Earth or Venus), that move in circular orbits about their common barycentre. In addition, the gravitational attraction of the small mass on the larger bodies is neglected. The CR3BP is formulated in a synodic reference frame, $S\,(x, y, z)$, as shown in Figure 1 and defined as follows: the origin coincides with the barycentre of the system, the x-axis is defined by the line passing through the two massive bodies and points in the direction of the smaller primary body, m_2, the z-axis points in the direction perpendicular to the plane in which the two massive bodies move and, lastly, the y-axis completes the right-handed reference frame. The synodic reference frame rotates at a constant angular velocity ω about the z-axis, *i.e.*, $\boldsymbol{\omega} = \omega\hat{\mathbf{z}}$.

During the formulation of the equations of motion, new units are introduced: $m_1 + m_2$ is chosen as the unit of mass, the distance between the two massive bodies as the unit of length, and $1/\omega$ as the unit of time. As a result, the dimensionless masses of the two massive bodies become $m_1 = 1 - \mu$ and $m_2 = \mu$, with the mass parameter $\mu = m_1/(m_1 + m_2)$. Then, as illustrated in Fig. 1, the two massive bodies are located at distances μ and $1 - \mu$ along the x-axis, respectively, with respect to the barycentre. Lastly, choosing $1/\omega$ as the unit of time yields $\omega = 1$, which implies that one dimensionless orbital period of the two primaries around their common barycentre is equal to 2π.

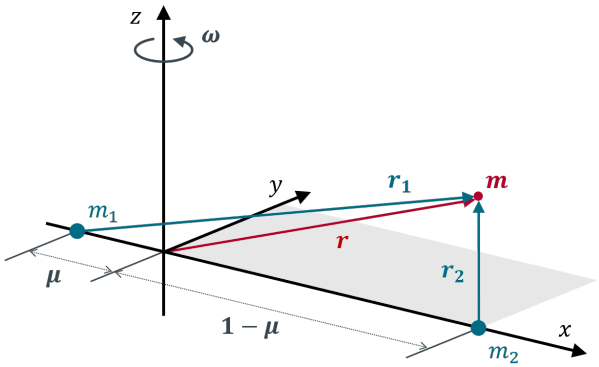

Fig. 1 Schematic of the circular restricted three-body problem.

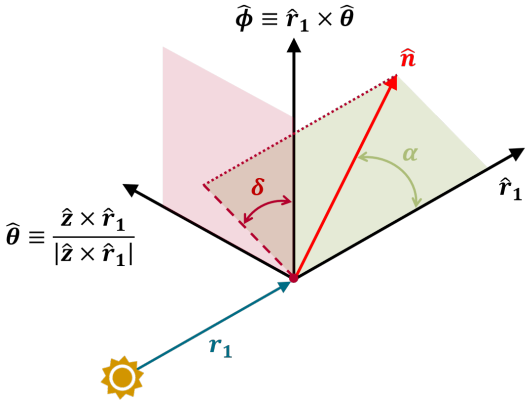

Fig. 2 Attitude of the solar sail.

In this reference system, the motion of a body is described by [12]:

$$\ddot{\mathbf{r}} + 2\omega \times \dot{\mathbf{r}} - \nabla U = \mathbf{a} \tag{1}$$

where $\dot{\square}$ indicates differentiation with respect to the dimensionless time t, $\mathbf{r} = [x \quad y \quad z]^T$ is the position vector of the body (see Fig. 1) and U is the effective potential function, that accounts for both the gravitational and centrifugal acceleration, given by [12]:

$$U(x, y, z) = \frac{1}{2}\left(x^2 + y^2\right) + \frac{1-\mu}{\|\mathbf{r}_1\|} + \frac{\mu}{\|\mathbf{r}_2\|} \tag{2}$$

where $\mathbf{r}_1$ and $\mathbf{r}_2$ are the position vectors of the body with respect to the primary bodies m_1 and m_2, respectively, defined as $\mathbf{r}_1 = [(\mu + x) \quad y \quad z]^T$ and $\mathbf{r}_2 = [x - (1-\mu) \quad y \quad z]^T$. The left-hand side of Eq. (1) represents the ballistic CR3BP and the right-hand side contains the perturbing acceleration, $\mathbf{a}$, which in this work only includes the solar-sail acceleration, $\mathbf{a}_s$, defined next in Sec. II.B.

B. Solar-Sail Model

In this paper, an ideal solar-sail model is considered. The ideal solar-sail model assumes that the sail is a perfectly reflecting mirror, *i.e.*, specular reflection of the incoming photons. As a result, the solar-sail acceleration vector acts perpendicular to the solar-sail surface, in the direction $\hat{\mathbf{n}}$ defined in Fig. 2. The attitude of the sail is described using two angles defined in a sail-centred orthogonal reference frame $B(\hat{\mathbf{r}}_1, \hat{\boldsymbol{\theta}}, \hat{\boldsymbol{\phi}})$, as shown in Fig. 2: the cone angle, α_s, and the clock angle, δ_s. In this reference frame, the sail normal vector is defined as follows:

$$\hat{\mathbf{n}}|_{\mathrm{B}} = \begin{bmatrix} \cos\alpha_s \\ \sin\alpha_s \sin\delta_s \\ \sin\alpha_s \cos\delta_s \end{bmatrix} \tag{3}$$

which can be expressed in the synodic reference frame by applying the following transformation:

$$\hat{\mathbf{n}} = \mathrm{R}\hat{\mathbf{n}}|_{\mathrm{B}} \tag{4a}$$

$$\mathrm{R} = \begin{bmatrix} \hat{\mathbf{r}}_1 & \hat{\boldsymbol{\theta}} & \hat{\boldsymbol{\phi}} \end{bmatrix} \tag{4b}$$

where definitions for $\hat{\boldsymbol{\theta}}$ and $\hat{\boldsymbol{\phi}}$ can be found in Fig. 2. The solar-sail acceleration is then given by [13]:

$$\mathbf{a}_s = \beta \frac{1-\mu}{r_1^2} \left(\hat{\mathbf{r}}_1 \cdot \hat{\mathbf{n}}\right)^2 \hat{\mathbf{n}} \tag{5}$$

where the parameter β is the so-called lightness number, which is a function of the spacecraft mass-to-sail area ratio σ and the critical solar-sail loading parameter $\sigma^* = 1.53 g/m^2$ [13]:

$$\beta = \frac{\sigma^*}{\sigma} \tag{6}$$

The lightness number is the performance index of the solar sail. For short- and mid-term solar-sail missions, taking into account recent advancements in solar-sail technology, this parameter is expected to reach values up to $\beta \approx 0.02$ and $\beta \approx 0.1$, respectively [14]; *e.g.*, NASA's Sunjammer was estimated to have a solar-sail lightness number of $\beta = 0.0363$ [15]. This mission intended to demonstrate the propellant-less propulsion potential of solar sails, similar to JAXA's IKAROS and NASA's NanoSail D2 missions in 2010, but was unfortunately cancelled before launch in October 2014.

In the literature, other performance models for solar sails exist, such as the optical force model [16] and the parametric force model [17], which take into account non-ideal properties of the sail that produce a component of the force tangential to the sail's surface. However, for the purpose of performing a preliminary mission analysis and a study of the use of space-based telescopes to detect imminent Earth impactors, the ideal solar-sail model is considered sufficient.

C. Elliptic Restricted Three-Body Problem

The operational orbits of the space-based telescope will be designed in the framework of the solar-sail ER3BP, mainly because the impacting trajectories of the NEOs have been determined in this dynamical model [2]. The fundamental difference between the CR3BP and the ER3BP is that the ER3BP takes into account the elliptic nature

of the orbits of the two primaries. Consequently, the equations of motion of the ER3BP explicitly contain the time through the true anomaly f, and are thus non-autonomous. This implies that any periodic solution of the solar-sail ER3BP must have a period which is an integer multiple of one year [18].

The ER3BP is formulated using a pulsating-rotating reference frame, $P(X, Y, Z)$, which is defined exactly as the S-frame, but that, due to the eccentricity of the orbits of the primaries, is a pulsating-rotating frame that rotates with a non-uniform angular velocity. As a result, the position of the primaries are always located along the X-axis at distances $1-\mu$ and μ, respectively, from the barycentre.

In the pulsating-rotating reference frame, the motion of the solar-sail spacecraft is described by [18]:

$$\begin{aligned} X'' - 2Y' &= \frac{1}{1+e\cos f}\left(\frac{\partial \Omega_E}{\partial X} + a_{s,X}\right) \\ Y'' + 2X' &= \frac{1}{1+e\cos f}\left(\frac{\partial \Omega_E}{\partial Y} + a_{s,Y}\right) \\ Z'' + Z &= \frac{1}{1+e\cos f}\left(\frac{\partial \Omega_E}{\partial Z} + a_{s,Z}\right) \end{aligned} \tag{7}$$

where $\square'$ indicates differentiation with respect to the secondary body's true anomaly f, e is the eccentricity of the orbit of the secondary body (the planet, *i.e.*, Earth or Venus), $\mathbf{a}_s = \begin{bmatrix} a_{s,X} & a_{s,Y} & a_{s,Z} \end{bmatrix}^T$ is the solar-sail acceleration defined by Eq. (5) and

$$\Omega_E(X, Y, Z) = \frac{1}{2}\left(X^2 + Y^2 + Z^2\right) + \frac{1-\mu}{\|\mathbf{R}_1\|} + \frac{\mu}{\|\mathbf{R}_2\|} \tag{8}$$

with $\mathbf{R}_1 = \begin{bmatrix} (\mu + X) & Y & Z \end{bmatrix}^T$ and $\mathbf{R}_2 = \begin{bmatrix} X - (1-\mu) & Y & Z \end{bmatrix}^T$.

The pulsating-rotating coordinates, $\mathbf{R} = (X, Y, Z)$, are related to the rotating coordinates, $\mathbf{r} = (x, y, z)$, via the equation $\mathbf{r} = \rho\mathbf{R}$, with the semi-latus rectum $\rho = \frac{1-e^2}{1+e\cos f}$. Therefore, when $e = 0$, Eq. (7) reduces to the circular case defined in Eq. (1), with the pulsating-rotating coordinates equalling the rotating coordinates [18].

III. Solar-Sail Halo Orbits in the Sun-Earth Three-Body System

This section covers the design of the first operational orbit candidate of the space-based telescope. First, the orbit requirements that must be considered in the design process are defined in Sec. III.A. Then, Section III.B introduces the concept and computation of AEPs in the solar-sail CR3BP. The section ends with a step-by-step explanation of the orbit design process in Sec. III.C.

A. Orbit Requirements

The orbit design in the SE system is mainly driven by the solar-sail performance, the space-based telescope performance requirements, the detectability of NEOs, the constraints associated to the numerical algorithms and the expected lifetime of the mission. The requirements are therefore defined as follows:

- The solar-sail lightness number shall be selected within the mid-term possibility of values up to $\beta = 0.1$.
- The solar-sail orbit shall lie outside a solar exclusion zone cone of half-angle 5° about the Earth-Sun line in order to ensure undisturbed communications with Earth [19].
- The solar-sail orbit shall be located as far from the Earth as possible in order to increase the warning times for the detected impacting NEOs.
- The solar-sail orbit shall have a period equal to one synodic year or a multiple thereof in order to be periodic in the ER3BP.
- The operational orbit of the space-based telescope shall be designed for and maintained over a lifetime of five years, which corresponds to the expected lifetime of similar space missions (*e.g.*, NASA's NEOCam [6]).

The first requirement is one of the reasons why solar-sail halo orbits are preferred over quasi-periodic orbits, known as Lissajous orbits, that can also be found in the vicinity of the collinear libration points. In this section, the orbit design is thus focused on determining solar-sail halo orbits.

B. Artificial Equilibrium Points

Artificial equilibrium points (AEPs) are locations within the Sun-Earth CR3BP where the solar-sail spacecraft can remain stationary. Such AEPs can be determined by finding the equilibrium solutions in the solar-sail CR3BP, *i.e.* finding those locations at which $\ddot{\mathbf{r}} = \dot{\mathbf{r}} = 0$ in Eq. (1). As derived in [16], the required solar-sail lightness number to maintain an AEP is:

$$\beta = \frac{r_1^2}{1-\mu} \frac{\nabla U \cdot \hat{\mathbf{n}}}{(\hat{\mathbf{r}}_1 \cdot \hat{\mathbf{n}})^2} \tag{9}$$

It is possible to observe that the required lightness number is only a function of the position of the solar-sail spacecraft within the CR3BP synodic reference frame. This means that, for a given sail lightness, a set of AEPs can be determined, generating contour surfaces [15]. Since the solar-sail orbit shall be around the x-axis of the Sun-Earth system in order to detect all NEOs coming from all possible directions with respect to the ecliptic plane, Eq. (9) can thus be used to determine the required sail lightness number to maintain different on-axis AEPs, at distances x_{AEP} from the barycentre, as shown by the black solid line in Fig. 3a. As expected, a larger sail lightness number is required to maintain an AEP farther from Earth and obtain a longer warning time for imminent impactors compared to a space-based telescope at the classical L_1 point.

C. Solar-Sail Halo Orbits

The generation of solar-sail halo orbits around a sub$-L_1$ AEP in the ER3BP starts by determining halo orbits around the sub$-L_1$ AEP of the CR3BP. According to [16], there are two solar-sail attitudes that allow obtaining solar-sail halo orbits around a sub$-L_1$ AEP of the CR3BP: either the sail normal is directed along the Sun–sail line or the sail normal is directed along the Sun–Earth line. In this paper, the attitude of the sail is fixed to be directed along the Sun–sail

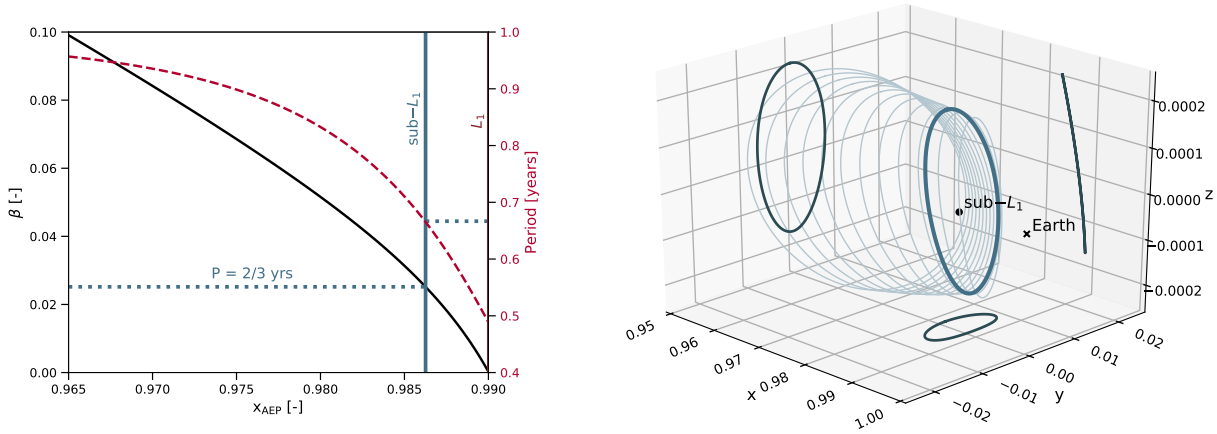

(a) Required sail lightness number to maintain an AEP on the Sun-Earth line at a distance x_{AEP} from the barycentre and orbital period (in synodic years) of the resulting halo orbit around that AEP in the CR3BP.

(b) Halo orbits around the x-axis of the Sun-Earth system. The solar-sail halo orbit highlighted in blue has an orbital period of approximately 2/3 of a synodic year and orbits about the sub$-L_1$ point at $x_{\text{AEP}} = 0.9862576$ with $\beta = 0.02518$.

Fig. 3 Halo orbits about the sub$-L_1$ point in the solar-sail Sun-Earth CR3BP.

line, *i.e.*, $\alpha_s = 0$. The computation of solar-sail halo orbits around AEPs in the CR3BP is then conducted following the approach in [20] and [21]. In this approach, the equations of motion are first approximated about the sub$-L_1$ AEP by linearisation and expansion of the potential function and solar-sail acceleration terms with a Taylor series to third order. Since this third-order solution is only a periodic approximation to the solution of the full non-linear system, the integration of the generated initial conditions through the equations of motion (given in Eq. (1)) result in an orbit that quickly drifts away from the AEP. To solve this, a differential correction scheme is applied to correct the initial conditions and numerically obtain integrated solutions to the non-linear equations. Details on this numerical technique can be found in [22]. However, the differential corrector only converges for solar-sail halo orbits with a very small out-of-plane amplitude ($A_z \sim 10^{-3}$). In order to increase the out-of-plane amplitude, such that the orbit lies outside the solar exclusion zone, a continuation scheme is applied with the z-coordinate of the initial state, z_0, as the continuation parameter.

Once periodic orbits are found in the CR3BP, a second continuation scheme is applied in order to obtain periodic orbits in the solar-sail ER3BP. Since for $e = 0$ the ER3BP reduces to the circular case, the eccentricity e can be used as the continuation parameter from a known solar-sail halo orbit in the CR3BP ($e = 0$) to a solar-sail halo orbit in the ER3BP with the required e of the planet, *i.e.*, $e = 0.0167$ of Earth.

However, as discussed in Sec. II.C, due to the non-autonomous nature of the ER3BP, any periodic solution of the solar-sail ER3BP must have a non-dimensional orbital period of $2\pi k$, where k is an integer. This implies that the initial orbit in the solar-sail CR3BP, which is used as the initial guess in the continuation algorithm, also needs to have an orbital period of k synodic years. The dashed line in Fig. 3a represents the orbital period of several solar-sail

halo orbits, with out-of-plane amplitudes of $A_z \sim 10^{-4}$, in the CR3BP around different AEPs, as a function of the x-coordinate of the AEP and, therefore, as a function of the sail lightness number. As the lightness number increases, and thus the AEP is farther from the Earth, it is possible to see that the orbital period approaches the Earth's orbital period.

Nonetheless, there are no solar-sail halo orbits with a period of one synodic year for $\beta \leq 0.1$. Therefore, instead, a periodic orbit with a period equal to a fraction of the synodic period is used as a starting point; *e.g.*, two revolutions of a halo orbit with a period of $\frac{1}{2}(2\pi)$ or three revolutions of a halo orbit with a period of $\frac{2}{3}(2\pi)$, can be used as initial guess to find solar-sail halo orbits with periods of one and two synodic years, respectively. It is possible to see in Fig. 3a that solar-sail halo orbits with periods equal to $\frac{1}{2}(2\pi)$ can only be found in the neighbourhood of the classical L_1 point, *i.e.*, with $\beta = 0.0$, and thus the advantage of using solar-sail propulsion for increasing the warning time is lost. Therefore, a solar-sail halo orbit with a period equal to $\frac{2}{3}(2\pi)$ is selected, which is plotted and highlighted in blue in Fig. 3b. The dotted horizontal and solid vertical lines in Fig. 3a indicate the value for β and x_{AEP}, respectively, of this SE halo orbit with an orbital period equal to ≈2/3 of a synodic year in the CR3BP: $\beta = 0.02518$ and $x_{\text{AEP}} = 0.9862576$.

Figure 4 shows a family of solar-sail halo orbits with $\beta = 0.02518$ about the sub$-L_1$ point at $x_{\text{AEP}} = 0.9862576$ in the solar-sail Sun-Earth CR3BP. They have been obtained by applying a continuation scheme, with z_0 as the continuation parameter, to the initial state of the small-amplitude solar-sail halo orbit with period of $\approx 2/3$ synodic years highlighted previously in Fig. 3b. As the out-of-plane amplitude of the halo orbit increases, the orbital period of the halo orbit varies: it slowly increases until reaching a maximum, and then drops rapidly. Two periodic orbits are found with a period of exactly $2/3$ years that lie outside the solar exclusion zone: a small-amplitude solar-sail halo orbit (the solid line in Fig. 4) and a large-amplitude solar-sail halo orbit (the dotted line in Fig. 4). Since the large-amplitude orbit

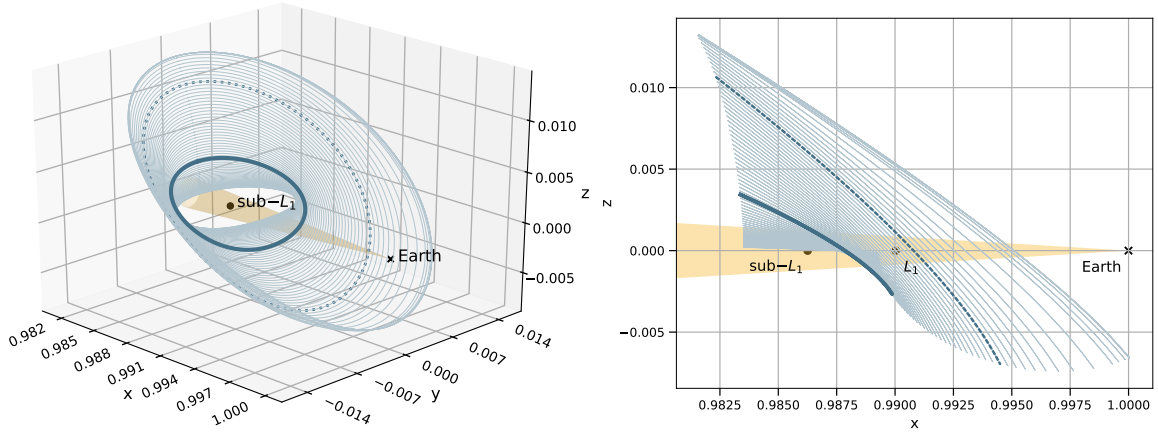

(a) Three-dimensional view. **(b) Projection on the *xz*-plane.**

Fig. 4 Family of solar-sail halo orbits with $\beta = 0.02518$ about the sub$-L_1$ point at $x_{\text{AEP}} = 0.9862576$ in the solar-sail Sun-Earth CR3BP. The yellow cone indicates the solar exclusion zone.

reaches the vicinity of the classical L_1 point, the small-amplitude solar-sail halo orbit is preferred and selected. The initial conditions of that orbit are:

$$\mathbf{x}_{\text{SE–CR3BP},0} = \begin{bmatrix} 0.98337903 & 0 & 0.00343505 & 0 & 0.01153356 & 0 \end{bmatrix}^T \tag{10}$$

Now that a solar-sail halo orbit in the CR3BP with a suitable period is found, the second continuation scheme in e is applied: starting with three revolutions of the periodic orbit in the CR3BP, with initial conditions given in Eq. (10), and increasing e by a suitably small value ($\sim 10^{-6}$), a new periodic orbit in the ER3BP is found by updating the initial conditions with a differential corrector. This differential correction scheme largely follows the method introduced by [22], but a constraint is introduced in order to ensure that the period of the resulting orbit is kept equal to two synodic years. As a result, all three components of the initial state, x_0, z_0 and $\dot{y}_0$, are allowed to vary. The implementation of such constraint is described in full detail in [23].

In Fig. 5, one period of the resulting solar-sail halo orbit in the ER3BP is plotted in the pulsating-rotating reference frame. The resulting initial conditions in the solar-sail ER3BP are as follows:

$$\mathbf{X}_{\text{SE–ER3BP},0} = \begin{bmatrix} 0.98333196 & 0 & 0.00343505 & 0 & 0.01154518 & 0 \end{bmatrix}^T \tag{11}$$

Note that this periodic orbit has a period equal to two synodic years, *i.e.*, 4π, as the initial guess for the continuation scheme consisted of three revolutions around a solar-sail orbit in the CR3BP with period equal to $\frac{2}{3}(2\pi)$. This can be

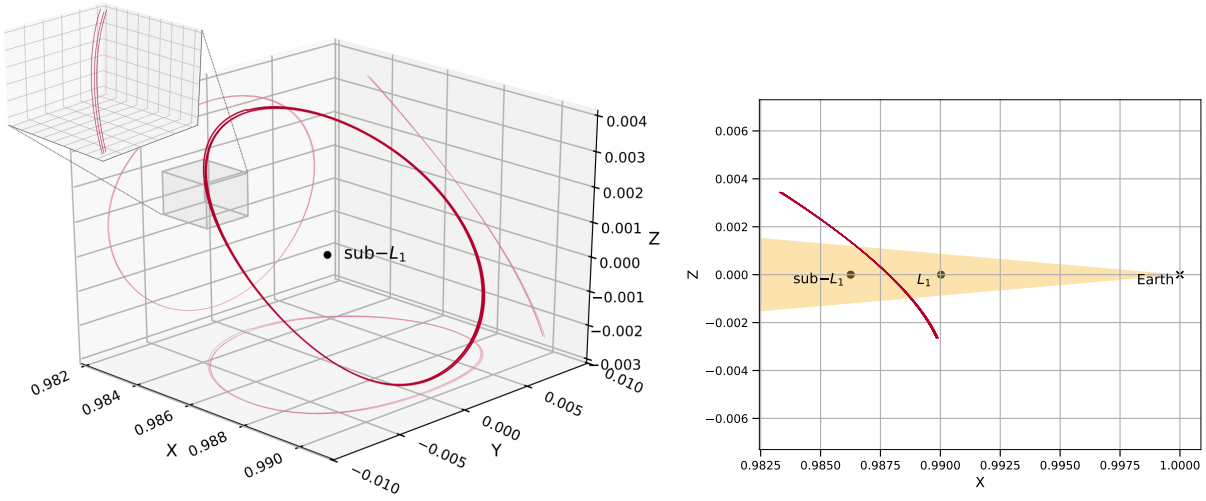

(a) Three-dimensional view. **(b) Projection on the *XZ*-plane.**

Fig. 5 Solar-sail halo orbit in the ER3BP with period equal to two synodic years, *i.e.*, 4π. Note that the indicated locations of the sub$-L_1$ and L_1 points are instantaneous and only hold valid when the distance between Sun and the Earth is 1 au.

observed in Fig. 5a, which shows the solar-sail spacecraft going around the sub$-L_1$ a total of three times.

Finally, the orbit of the space-based telescope is designed for an operational lifetime of five years. To this aim, the initial conditions of the solar-sail halo orbit in the ER3BP, given in Eq. (11), are integrated for three revolutions, *i.e.*, six synodic years. Unfortunately, due to the large instability of the dynamics in the ER3BP, the solar-sail spacecraft quickly drifts away from the orbit after approximately one and a half revolutions. To solve this, a multiple shooting differential correction scheme is used in order to find a continuous trajectory that is close to the periodic orbit in Fig. 5. Details of the implementation of this method can be found in [24]. As initial guess for the multiple shooting method, the solar-sail halo orbit in the ER3BP consisting of three revolutions (see Fig. 5) is patched consecutively three times. Then, this reference trajectory is divided into segments, and two differential correction levels are applied. The first level adjusts the velocities at each patch-point along the trajectory by using a differential corrector, resulting in a trajectory that is continuous in position but not in velocity, and must thus perform a ΔV at each patch-point. The second level then adjusts the positions and epochs at each patch-point using a least-squares method that is designed to minimise the total ΔV cost of the trajectory. The result of the multiple shooting scheme is a trajectory that satisfies the dynamics of Eq. (7) along each segment, but presents a slight discontinuity in position and velocity at each patch-point. In this paper, the discontinuities at each patch-point have been limited to 10^{-10} in position and 10^{-5} in velocity, which correspond to a deviation of ~ 15 m and ~ 0.3 m/s. The resulting trajectory is designed for a dimensionless time of 12π, *i.e.*, six synodic years. The plot of this trajectory is not shown in this paper because it does not provide any additional insight to what has been shown previously in Fig. 5.

IV. Vertical Lyapunov Orbits in the Sun-Venus Three-Body System

This section covers the design of the second mission candidate for the operational orbit of the space-based telescope. First, the orbit requirements that must be considered in the design process are defined in Sec. IV.A. Then, Section IV.B discusses how to describe the libration point orbits (LPOs) that are found in the vicinity of the collinear and triangular libration points of the Sun-Venus system. The section ends with a step-by-step explanation of the orbit design process for both LPOs around the collinear and triangular libration points, in Sec. IV.C and Sec. IV.D, respectively.

A. Orbit Requirements

The orbit design in the SV system is driven by fewer requirements than the SE case for the following reasons. First, orbits in the SV system are already located close enough to the Sun and the addition of solar-sail propulsion is thus not required, as far as the design of the orbit is concerned, to displace the orbit. Second, the orbit is no longer constrained to remain outside the solar exclusion zone. This implies that families of LPOs other than halo orbits can be considered. As a matter of fact, halo orbits only exist in the vicinity of the collinear libration points [25], while the traditional Lissajous and Lyapunov orbits can also be found around the SV L_4 and L_5 points. Therefore, the orbit design in the

SV case is mainly driven by the detectability of NEOs and the expected lifetime of the mission. For all three orbits, the requirements are defined as follows:

- The LPO shall have an out-of-plane motion with an amplitude similar to the solar-sail halo orbit around the Sun-Earth sub$-L_1$ point*.
- The operational orbit of the space-based telescope shall be designed for and maintained over a lifetime of five years, which corresponds to the expected lifetime of similar space missions (*e.g.*, NASA's NEOCam [6]).

B. Libration Point Orbits

Similar to the design process followed in Sec. III, the generation of LPOs in the ER3BP starts by determining LPOs in the CR3BP. The motion of an LPO is first approximated by linearisation of the equations of motion of the ballistic CR3BP, given in Eq. (1) with $\mathbf{a} = 0$, about the libration point. The general form of this first-order solution is [26]:

$$\tilde{x} = \sum_{i=1}^{6} A_i e^{\lambda_i t} \qquad \tilde{y} = \sum_{i=1}^{6} B_i e^{\lambda_i t} \qquad \tilde{z} = \sum_{i=1}^{6} C_i e^{\lambda_i t} \tag{12}$$

where $\tilde{\square}$ denotes the motion with respect to the libration point, A_i, B_i and C_i represent constant coefficients and λ_i are the eigenvalues of the linear system. The stability of the non-linear system for motion about the libration points is determined by the eigenvalues, or characteristic roots, of the linear system. Since the eigenvalues occur in conjugate pairs, the linearised motion of an LPO is defined stable if all λ_i are different and purely imaginary. In the case of the collinear points, the system yields two real eigenvalues of opposite sign, which means that the motion about these equilibrium points is generally unstable. However, the other four eigenvalues consist of two conjugate pairs of imaginary eigenvalues, which indicate the potential for generating stable periodic orbits by selecting the appropriate initial conditions that excite only the oscillatory modes. In the case of the triangular points, all four eigenvalues are purely imaginary for $\mu < 0.03852$. Since for the SV system, $\mu_{\text{Sun-Venus}} = 2.448 \cdot 10^{-6}$, the non-linear behaviour near L_4 and L_5 is expected to be oscillatory and bounded [26].

C. Vertical Lyapunov Orbits about the L_3 Libration Point

For initial conditions that produce pure oscillatory motion, the general form of the solution for motion near the collinear libration points is described as follows [12]:

$$\begin{aligned} x' &= -A_x \cos\left(\omega_{xy} t + \Phi_{xy}\right) \\ y' &= k A_x \sin\left(\omega_{xy} t + \Phi_{xy}\right) \\ z' &= A_z \sin\left(\omega_z t + \Phi_z\right) \end{aligned} \tag{13}$$

*This requirement is defined in order to have a fair comparison between both orbit locations in the following evaluation of the performance of each space-based telescope.

where $\langle A_x, \omega_{xy} \rangle$ and $\langle A_z, \omega_z \rangle$ are the in-plane and out-of-plane amplitudes and frequencies, respectively, k is a constant denoting a relationship between μ and the position of the libration point, and Φ_{xy} and Φ_z represent generic phase angles. Equation (13) describes a three-dimensional motion that is quasi-periodic since the in-plane and the out-of-plane frequencies, ω_{xy} and ω_z, are generally different. This motion results in the so-called Lissajous orbit, which is a quasi-periodic LPO. Halo orbits are then special Lissajous orbits, in which ω_{xy} and ω_z are forced to match. As a result, A_x, A_z, Φ_{xy} and Φ_z are constrained.

The most well-known method to generate initial guesses for periodic halo orbits in the CR3BP is the one described in [27], which applies the method of successive approximations to the first-order solution, given in Eq. (13), in order to derive a third-order solution for the periodic motion about the collinear points. However, as explained in [25], this method cannot be used to obtain halo orbits in the L_3 case because the third-order expansions are no longer convergent. Furthermore, although the halo family associated to L_3 does exist, as shown in [22], the resulting orbits are very large, and are thus not useful for the purpose of this paper.

For these reasons, a different approach is proposed in this paper. First, a family of Lissajous quasi-periodic orbits is obtained by generating initial conditions using the first-order solution given in Eq. (13), where A_x and A_z are design parameters and the remaining parameters are computed using the expressions in [28]. Then, since the resulting LPOs are not periodic, a multiple shooting differential correction scheme is applied, similar to the one implemented in Sec. III.C but slightly modified such that the periodicity of the orbit is added as a constraint [24]. For the L_3 case, the discontinuities at each patch-point have been limited to 10^{-14} in position and 10^{-13} in velocity, which are negligible and can be attributed to truncation errors.

Figure 6 shows the resulting trajectories around the L_3 point in the Sun-Venus CR3BP. It is possible to see that the Lissajous family has bifurcated into two different families of LPOs: planar Lyapunov orbits (in red) and vertical

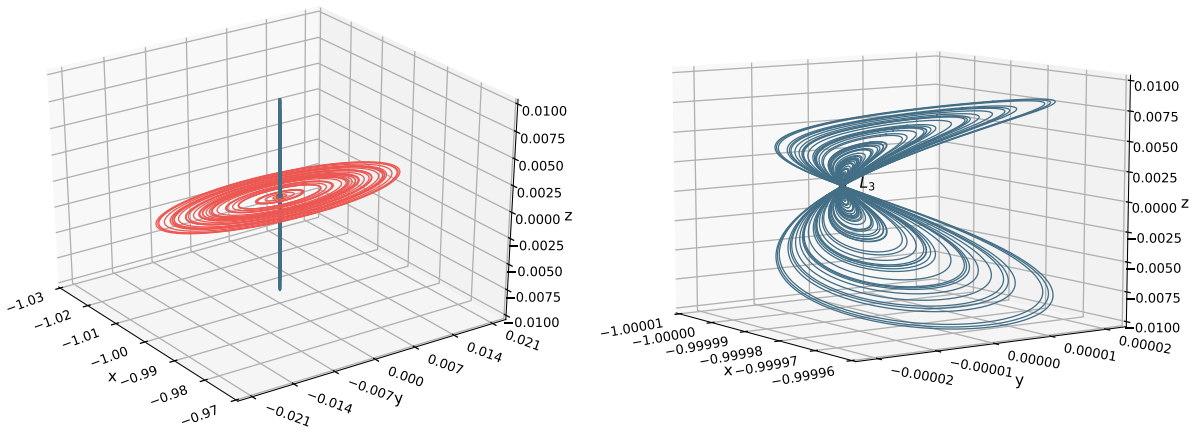

(a) Three-dimensional view. **(b) Zoomed-in three-dimensional view.**

Fig. 6 Family of planar and vertical Lyapunov orbits around the L_3 point in the Sun-Venus CR3BP.

Lyapunov orbits (in blue, see Fig. 6b). Both families of LPOs are periodic with a period equal to $\sim 2\pi$, *i.e.*, one Venus synodic year, which corresponds to approximately 225 sidereal days. Out of these two options, a vertical Lyapunov orbit is preferred due to the out-of-plane motion. The selected one is highlighted in Fig. 7 and has an out-of-plane amplitude of $A_z \sim 500\,000$ km, which is approximately equal to the z-amplitude of the first orbit candidate.

Vertical Lyapunov orbits around the L_3 point are found to be very stable within the framework of the CR3BP, unlike the vertical Lyapunov orbits around the L_1 and L_2 libration points, which are known to be very unstable. After nine revolutions, *i.e.*, ~ 5.5 sidereal years, the dimensionless errors in position and velocity with respect to the initial conditions are smaller than 10^{-12}.

Finally, a continuation scheme in e is applied to obtain the vertical Lyapunov orbit in the ER3BP: starting with the selected vertical Lyapunov orbit highlighted in Fig. 7 and increasing e by a suitably small value ($\sim 10^{-5}$), a new periodic orbit in the ER3BP is found by consecutively updating the initial reference trajectory with the multiple shooting differential corrector until reaching Venus' eccentricity, *i.e.*, $e = 0.00677$. Figure 8 shows the resulting trajectory in the Sun-Venus ER3BP during the expected operational lifetime of the mission.

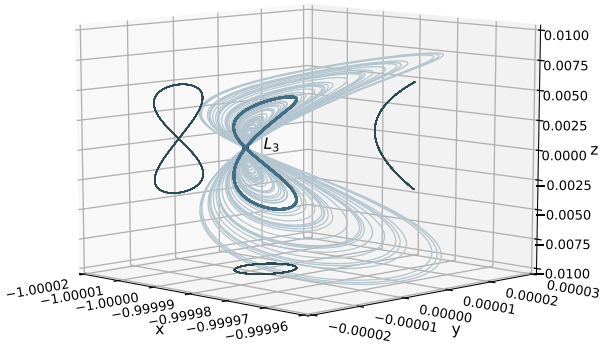

Fig. 7 Family of vertical Lyapunov orbits around the L_3 point in the Sun-Venus CR3BP. The selected vertical Lyapunov orbit is highlighted in blue.

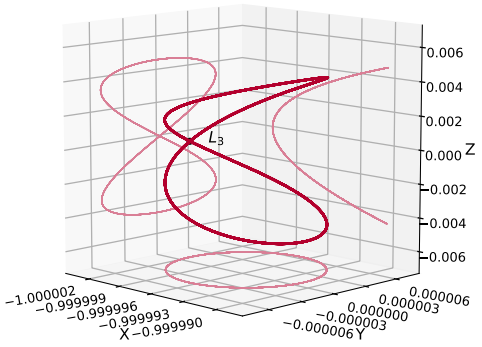

Fig. 8 Vertical Lyapunov in the Sun-Venus ER3BP. Note that the indicated location of the L_3 point is only valid when the distance Sun-Venus is 0.72 au.

D. Vertical Lyapunov Orbits about the Triangular Libration Points

The study of the stability of the linear system concludes that the motion about the triangular libration points is bounded and stable. This linearised motion can thus be described by [12]:

$$\begin{aligned}
\tilde{x} &= C_1 \cos s_1 t + S_1 \sin s_1 t + C_2 \cos s_2 t + S_2 \sin s_2 t \\
\tilde{y} &= \bar{C}_1 \cos s_1 t + \bar{S}_1 \sin s_1 t + \bar{C}_2 \cos s_2 t + \bar{S}_2 \sin s_2 t \\
\tilde{z} &= C_1 \cos t + C_2 \sin t
\end{aligned} \tag{14}$$

where C_i, S_i, $\bar{C}_i$ and $\bar{S}_i$ represent constant coefficients and s_1 and s_2 are the two frequencies of the linear system. Equation (14) thus shows that the motion in the z-direction oscillates with the same period as the rotation of the S-frame, whereas the motion in the xy-plane is a superposition of two periodic motions: one long-period motion with frequency s_1 and one short-period motion with frequency s_2. Since the period of motion in the xy-plane differs from the one in the z-direction, Eq. (14) describes a Lissajous orbit. Using the method defined in [12], a Lissajous family of quasi-periodic orbits is determined by selecting appropriate initial conditions, which delete the long-period motion terms in Eq. (14).

Subsequently, the same approach as in Sec. IV.C is followed. By means of a multiple shooting differential corrector, and adding the periodicity as a constraint, periodic orbits around the L_4 and L_5 points in the Sun-Venus CR3BP are determined from the quasi-periodic Lissajous orbits, as shown in Fig. 9 for the L_4 case. It is possible to observe that, similar to the dynamics around the L_3 point, the Lissajous family around the triangular libration points also bifurcates into families of planar and vertical Lyapunov orbits. Moreover, just like in the L_3 case, both families of LPOs have a period equal to $\sim 2\pi$ and are also very stable. Note that the results for the family of periodic orbits around the L_5 point is not included in this paper for brevity, but they are found to be symmetric with the L_4 case with respect to the xz-plane, and the same conclusions can thus be drawn.

The selected vertical Lyapunov orbit around the L_4 point is highlighted in Fig. 9b, which follow the same criterion as for the L_3 case; they both have an out-of-plane amplitude of approximately 500 000 km. Together with the selected vertical Lyapunov orbit around the L_5 point, these LPOs in the Sun-Venus CR3BP are then used as starting point for the continuation scheme in e, which has already been explained previously in Sec. IV.C.

Finally, all three vertical Lyapunov orbits around the L_3, L_4 and L_5 libration points in the Sun-Venus ER3BP are

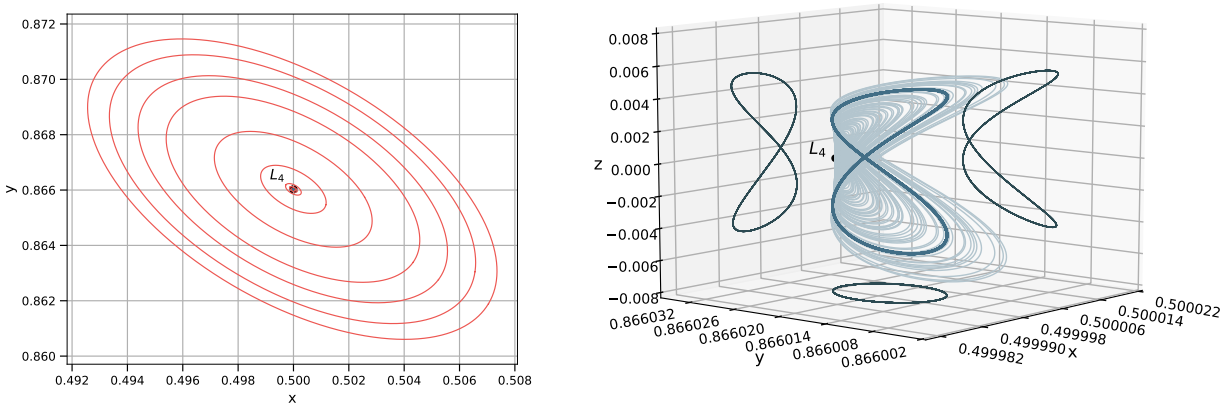

(a) Projection on the xy-plane. **(b) Three-dimensional view.**

Fig. 9 Family of planar and vertical Lyapunov orbits around the L_4 point in the Sun-Venus CR3BP.

represented in Fig. 10. Note that the Z-axis is not to scale.

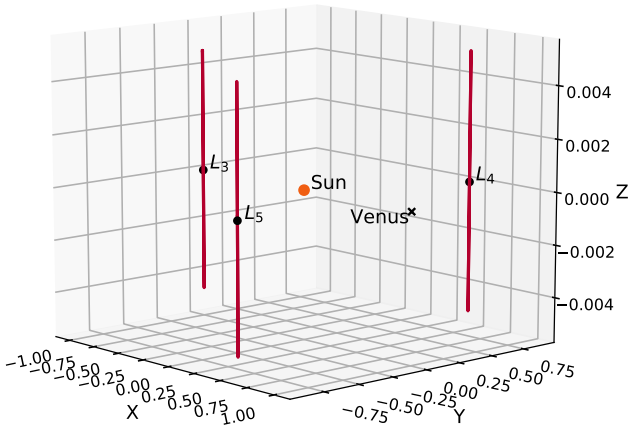

Fig. 10 Selected vertical Lyapunov orbits around the L_3, L_4 and L_5 libration points in the Sun-Venus ER3BP.

V. Space-based Survey Model

This section defines the relevant parameters, models and overall theoretical framework of the space-based survey model that is implemented and used in the simulations. First, the performance characteristics of both visible and thermal infrared space-based surveys are presented in Sec. V.A. Then, the viewing constraints and field of regard (FOR) of each orbit candidate are defined in Sec. V.B. Section V.C introduces the four different populations of synthetic Earth impactors that are used to estimate and evaluate the performance of each survey system at providing warning for impacting NEOs. The section ends with a brief explanation of how the detection of NEOs is simulated and implemented in the space-based survey model in Sec. V.D.

A. Performance Characteristics

The performance characteristics for both VIS and TIR space-based surveys are summarised in Table 1. These requirements have been taken from NASA's 2017 NEO SDT Report [1], which constitutes the most comprehensive results to date regarding both ground- and space-based NEO surveys. In [1], a total of 17 survey solutions were simulated and evaluated in order to estimate the performance achievable by a NEO survey system based on current technology. Table 1 presents the characteristics of the telescope and the detector used in the best-case scenario obtained in [1] for both VIS and TIR space-based telescopes. The performance characteristics of the telescope and the detector are assumed to be independent of the orbit location.

Table 1 Performance characteristics for both VIS and TIR space-based surveys at the sub$-L_1$ point of the Sun-Earth system and at the L_3, L_4 and L_5 points of the Sun-Venus system [1].

Parameter	VIS	TIR
Aperture [m]	0.5	0.5
Waveband [μm]	0.4–1	6–10
FOV [°]	10.6×5.3	1.7×7.13
Pixel scale [″/pixel]	2	3
Exposure time [s]	24	180
Detector type	E2V CCD	HgCdTe
Pixel size [μm]	10	18
Image FWHM [″]	1	4
Dark current [e^-/s]	<0.001	<200
Readout noise [e^-]	4	<30
Quantum efficiency [%]	88	60
Optical Transmission [%]	100	100
Well depth [e^-]	90 000	65 000
Point-source sensitivity (SNR = 5)[†]	21.7 Vmag	150 μJy

B. Viewing Constraints and Search Regions

Literature suggests that potential impactors are most likely to be found by searching the space inside Earth's orbit, *i.e.*, at small solar elongations (the Sun-observer-object angle in the ecliptic) [29]. These asteroids are also the most hazardous because they approach us from the day-side, and are thus very difficult to observe using ground-based telescopes. Therefore, it is desirable to design a space-based survey system that is able to look as close to the Sun as possible and back towards the Earth in order to monitor these objects coming from the Sun.

The viewing zones for both TIR and VIS telescopes at each location are presented in Table 2, specified as ranges in solar elongation and Sun-centred ecliptic latitude. For space-based surveys, especially at mid-IR wavelengths, the Sun imposes the most significant constraint on the search regions, as thermal loading imposes constraints on the minimum solar elongations [5]. Figure 11 shows the search regions at IR wavelengths for both surveys at the SE sub$-L_1$ point (left) and at the SV L_5 point (right) as red-shaded areas. Note that the same search regions are defined for the SV L_3 and L_4 points. Through the use of a Sun-shield, a space mission at the SE sub$-L_1$ point is able to point in any direction from a solar elongation of ±45° to ±125°. Instead, the search region of a space mission at the SV L_3, L_4 and L_5 points is centred at opposition (*i.e.*, at a solar elongation of 180°) and can point down to a solar elongation of 105°.

At visible wavelengths, the main difficulty is to exclude the fully sun-lit Earth and Moon from the instrument's

[†]The point-source sensitivity indicates the 'faintest' object that the telescope can detect. It is defined differently for the VIS and TIR telescopes; at VIS wavelengths, it expresses the limiting apparent visual magnitude that the telescope can detect with a detection threshold of SNR equal to five. At IR wavelengths, the metric used is the noise equivalent spectral irradiance (NESI), in units of micro-Janksy (μJy), with a detection threshold set at five times the NESI, which is equivalent to SNR=5. Furthermore, since the point-source sensitivity at IR wavelengths varies with ecliptic latitude, longitude and heliocentric distance, it is specified near the midpoint of the viewing zones for each survey, or $(0°, 90°)$ for the SE L_1 and $(0°, 180°)$ at 0.7 au heliocentric distance for the SV $L_{3,4,5}$.

Table 2 Viewing zones for both VIS and TIR space-based surveys at the sub$-L_1$ point of the Sun-Earth system and at the L_3, L_4 and L_5 points of the Sun-Venus system.

Viewing zones	Location	VIS	TIR
Solar elongation [°]	SE sub$-L_1$	±(60-160)	±(45-125)
	SV $L_{3,4,5}$	180±120	180±75
Ecliptic latitude [°]	SE sub$-L_1$	±80	±42
	SV $L_{3,4,5}$	±80	±42

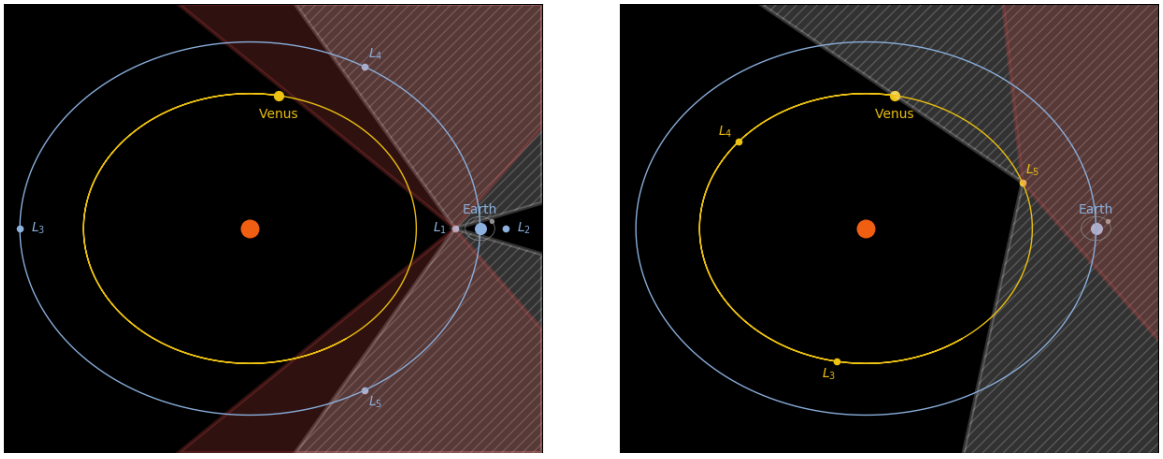

(a) Search region for a space-based telescope at the L_1 point of the Sun-Earth system. Note that the same search region is defined for the sub$-L_1$ point.

(b) Search region for a space-based telescope at the L_5 point of the Sun-Venus system. Note that the same search regions are defined for the L_3 and L_4 points.

Fig. 11 Search regions for both surveys at the SE L_1 point (left) and at the SV L_3, L_4 and L_5 points (right). The white-dashed area represents the search region at VIS wavelengths and the red-shaded area represents the search region at IR wavelengths. The orbits and locations of Earth, Venus and the Moon are not to scale.

field-of-view (FOV), as well as to limit the impact of stray light. These viewing constraints are incorporated in terms of keep-out zones for the Sun, Moon and Earth, as illustrated in Fig. 11, which shows the search regions at VIS wavelengths as white-dashed areas. The keep-out zone required for the Sun is implemented by considering an exclusion angle of 60° for both orbit locations. The keep-out zone for the Earth and the Moon is incorporated with an exclusion angle of 20°, but only for the space-based survey at the SE sub$-L_1$ point. Regarding the survey at the SV L_3, L_4 and L_5 points, the software ignores those frames where the Earth and/or the Moon are in the FOV[‡].

C. Synthetic Population of Impacting Near-Earth Objects

For all simulations of space-based surveys in this paper, the population of synthetic Earth-impacting NEOs generated in [2] is used to estimate the detection rate and evaluate the effectiveness of each survey system at providing warning

[‡]Venus is expected not to be in the FOV of the VIS space-based telescope at detection, as NEOs are the brightest, and most likely thus to be detected, at opposition.

for NEOs. This population of Earth impactors is based on the most updated NEO population model developed in [30], and is thus distributed in a range of absolute magnitude H. This means that each orbit is associated to one NEO with a given size, for a given albedo p_v. The population contains a total of 2 451 Earth impactors in the range $H = 23 - 30$. The corresponding size can be estimated with [31]:

$$D = \frac{1.329 \cdot 10^6}{\sqrt{p_v}} 10^{-0.2H} \tag{15}$$

where D is diameter of the object, in metres. Therefore, for a default albedo of 0.14, this population of synthetic NEOs contains objects with diameters from $\sim$ 90 m down to $\sim$ 4 m. Nonetheless, for the purpose of determining the performance of a survey system at detecting NEOs of all sizes, in this paper, the physical properties of each object of the population are detached from its orbital elements. It is thus assumed that there is no correlation between physical size and orbit[§].

While NASA is aiming at finding NEOs larger than 140 m [1][5], this paper is focused on detecting and providing warning for potential impact threats of smaller NEOs. To this aim, four different synthetic populations of impactors are used in the simulations:

- Population #1: follows the expected size-frequency distribution [1].
- Population #2: assumes the same absolute magnitude for all objects, $H = 22$.
- Population #3: assumes the same absolute magnitude for all objects, $H = 24$.
- Population #4: assumes the same absolute magnitude for all objects, $H = 26$.

For an albedo of 0.14, the lower boundary of $H = 22$ corresponds to a diameter of $\sim$ 140 m, which is NASA's cataloguing objective, while the upper boundary of $H = 26$ corresponds to $\sim$ 22 m, which is approximately the size of the Chelyabinsk asteroid impactor. In the first population, the absolute magnitude for each object is thus randomly assigned within the range of absolute magnitudes between $H = 22$ and $H = 26$, according to the distributions given in [1].

Figure 12 shows the cumulative number of impacting NEOs as a function of the diameter and albedo for all four populations. Since the albedo is typically unknown, three different values of p_v are assumed: 0.05 and 0.25, which are the lower- and upper-value of the range of albedos of the vast majority of main-belt asteroids[¶], and the default value of 0.14 that is often used [30].

D. Detectability of Near-Earth Objects

Whether an object can be detected in an image or not, depends on its Signal-to-Noise Ratio (SNR), *i.e.*, the ratio of the signal (the NEO) to the noise, at the detector. The computation of the SNR follows the approach defined in [33]

[§]The same assumption has been done previously in similar works, such as in [32].

[¶]Minor Planet Center. URL `https://www.minorplanetcenter.net/iau/Sizes.html` (Access date 2019-02-15)

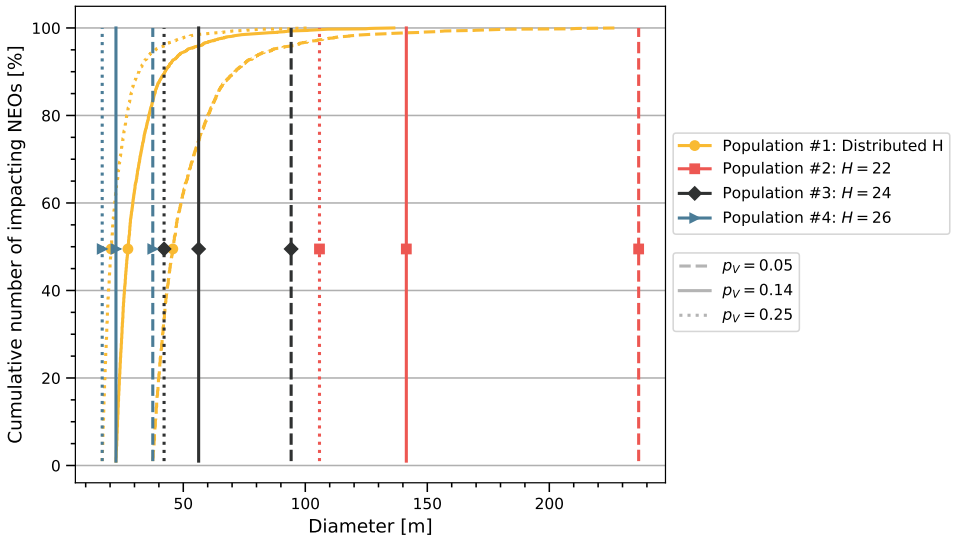

Fig. 12 Cumulative number of impacting NEOs as a function of the diameter and albedo p_v.

and [34], which only looks at the SNR in the centre pixel. Due to the Gaussian shape of the light source, it can be assumed that most of the light is collected in the centre pixel, and only the percentage of light within this centre pixel is thus considered. The SNR within the centre pixel is computed with [34]:

$$\mathrm{SNR} = \frac{\mathrm{S_e}}{\left(\mathrm{S_e} + k_{\mathrm{dark}} t_{\mathrm{exp}} + k_{\mathrm{read}}^2 + \mathrm{B_e}\right)^{1/2}} \tag{16}$$

where $\mathrm{S_e}$ is the object's signal in electrons, $\mathrm{B_e}$ is the background's signal in electrons, and the rest of the terms account for various noise sources at the detector (assumed to be independent). In this paper, the sources of noise considered are the dark current noise, $k_{\mathrm{dark}} t_{\mathrm{exp}}$, which is the electric current that flows without light, k_{dark}, during the exposure time t_{exp}, and the readout noise, k_{read}^2, which accounts for the loss of signal during the reading out of the charge from a single pixel [33].

Given the asteroid's irradiance at the detector, the object's signal in electrons is computed with:

$$\mathrm{S_e} = \frac{1}{hc} A_{\mathrm{eff}} t_{\mathrm{exp}} p_{\mathrm{px}} \int_{\lambda_1}^{\lambda_2} \mathrm{F_A}(\lambda) \tau(\lambda) \mathrm{QE}(\lambda) \lambda d\lambda \tag{17}$$

where A_{eff} is the effective aperture area of the sensor, p_{px} is the percentage of light within the centre pixel[‖], $\mathrm{F_A}(\lambda)$ is the object's irradiance at the detector as a function of wavelength λ, $\tau(\lambda)$ is the optical transmission as a function of wavelength, $\mathrm{QE}(\lambda)$ is the quantum efficiency of the detector as a function of wavelength, and λ_1–λ_2 is the waveband of the detector. Note that both QE and τ are assumed to be independent of wavelength in this paper, and are thus

[‖] Also known as straddle factor. It is computed using the approach in [34].

taken out of the integral. As a last remark, the calculation of the SNR first accounts for pixel saturation by limiting the maximum possible electrons in S_e to the well depth, and is then computed using Eq. (16).

Similarly, given some background irradiance, the background's signal in electrons is computed as follows:

$$B_e = \frac{1}{hc} A_{\text{eff}} t_{\text{exp}} \text{pixelscale}^2 \int_{\lambda_1}^{\lambda_2} F_B(\lambda)\tau(\lambda)\text{QE}(\lambda)\lambda d\lambda \tag{18}$$

where $F_B(\lambda)$ is the background's irradiance at the detector as a function of wavelength. The pixel scale is used to take into account the apparent size of a pixel of the telescope, *i.e.*, the FOV per pixel.

1. Object signal in visible spectrum

The determination of the object's signal depends on the wavelength band of the detector; for a visible detector, the signal is given by the optical brightness or apparent magnitude of the object. In this paper, the computation of the apparent magnitude of the object follows the approach used for Solar-System bodies. The apparent magnitude m is thus described by [35]:

$$m = H(1, \alpha) + 2.5 \log_{10}\left(\frac{r^2\Delta^2}{\phi(\alpha)}\right) \tag{19}$$

where r is the distance of the NEO from the Sun (in au), Δ is the distance of the NEO from the observer (in au), α is the phase angle (*i.e.*, the angle Sun-object-observer) and $\phi(\alpha)$ is the phase function [35]:

$$\phi(\alpha) = \frac{2}{3}\left(\left(1 - \frac{\alpha}{\pi}\right)\cos\alpha + \frac{1}{\pi}\sin\alpha\right) \tag{20}$$

The term $H(1, \alpha)$ in Eq. (19) is related to the opposition effect, *i.e.*, a surge in brightness observed when the object is near opposition ($\alpha = 0$). The opposition effect is described by computing the absolute magnitude of the NEO as a function of the phase angle [35]:

$$H(1, \alpha) = H - \frac{a}{1 + \alpha} + b \cdot \alpha \tag{21}$$

where the values a and b depend on the visual albedo, as described in [36] and [37]. Once the optical brightness of the NEO is computed, the irradiance at the detector F_A can be easily computed using the conversion from magnitude m to flux F, $F = 10^{0.4(M_\odot - m)} F_\odot$, where $F_\odot = 1366$ W/m^2 is the solar constant and $M_\odot = -26.8$ is the magnitude of the Sun in the standard V-filter (visual wavelength centred at 550 nm)**.

**Note that there is no dependency in the object's irradiance as it denotes a flux density, *i.e.*, energy per time and area over the complete wavelength band. This assumes the use of the standard V-filter from the so-called Johnson-Cousins UBVRI system [38][39]

2. Object signal in thermal infrared

For an infrared detector, the object's signal is given by the thermal emission of the object. The total emitted thermal radiation at different wavelengths is calculated by means of an asteroid thermal model. Two thermal models are considered in this paper: the Standard Thermal Model (STM) and the Near-Earth Asteroid Thermal Model (NEATM).

The STM assumes that the asteroid has a spherical shape, a negligible thermal inertia and that it is observed at opposition. Under these assumptions, the thermal emission from any point on the asteroid's surface can be considered to be in instantaneous equilibrium with the solar radiation absorbed at that point. Consequently, the temperature distribution on the surface is fixed. The STM is known to derive diameters that are systematically larger than other methods, which is attributed to thermal-infrared beaming[††]. To solve this, the so-called beaming parameter η is introduced, which is equal to $\eta = 0.756$ for the STM. Details on this 'refined' STM can be found in [40]. Similar to the STM, the NEATM assumes the asteroid to have a spherical shape and an STM-like temperature distribution, but with a parameter η that varies in order to fit the modelled fluxes and temperatures to the data. The default value for NEAs that is often used is $\eta = 1.2$ [31]. However, in this paper, the correlation with the phase angle found in [41] is used instead to determine the beaming parameter. Details on the NEATM can be found in [31].

In general, the literature suggests that the NEATM results in the most consistent agreement with the spectral types and radar sizes of NEAs. Furthermore, while the STM is only valid at phase angles up to 30°, the NEATM is valid at all phase angles. Nonetheless, for wavelengths longer than 8 μm, for which [40] estimated that the STM is reliable, the results derived by the STM do not significantly differ from the NEATM. Since the waveband of the TIR space-based telescope (6–10 μm) lies within the longer-wavelength part of the IR spectrum, both thermal models are implemented. For a random impacting NEO observed by the TIR telescope, Fig. 13 shows the computed thermal flux at observation time, using both the STM and NEATM, as a function of wavelength. It is possible to see that the two thermal models yield similar fluxes in the region of the TIR waveband (shown in red), concluding thus that both models can be used.

3. Background signal

The background signal (or sky brightness) is typically computed as a sum of different light contributions. For space-based sensors, the total background noise is a sum of the following sources: planets, stars, galaxies, zodiacal light and interstellar medium (only relevant in TIR mode). Figure 14 presents an overview of the brightness of the night sky outside the lower terrestrial atmosphere and at high ecliptic and galactic latitudes, as a function of wavelength. The wavebands of both VIS and TIR space-based telescopes are also shown in Fig. 14 as yellow and red shaded areas, respectively. At the IR wavelengths of the space-based telescope, the first and major contribution to the noise is due to the zodiacal light. The second contribution, which is from faint stars, is almost three orders of magnitude smaller, and

[††]The thermal emission is 'beamed' into the sun-ward direction, due to surface roughness, such that at small phase angles a larger-than-expected flux level is observed.

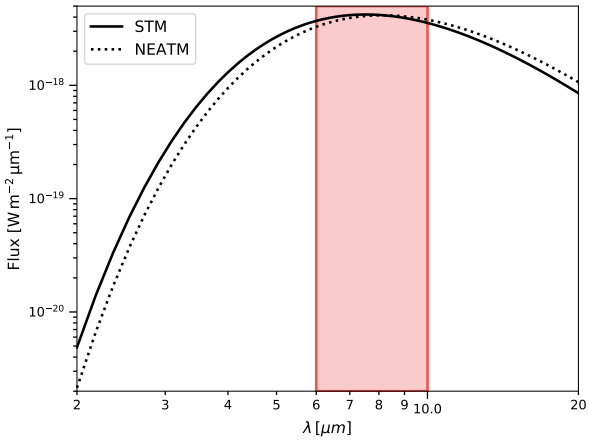

Fig. 13 Comparison of the thermal flux given by the STM and NEATM as a function of wavelength. The waveband of the TIR telescope is shown in red.

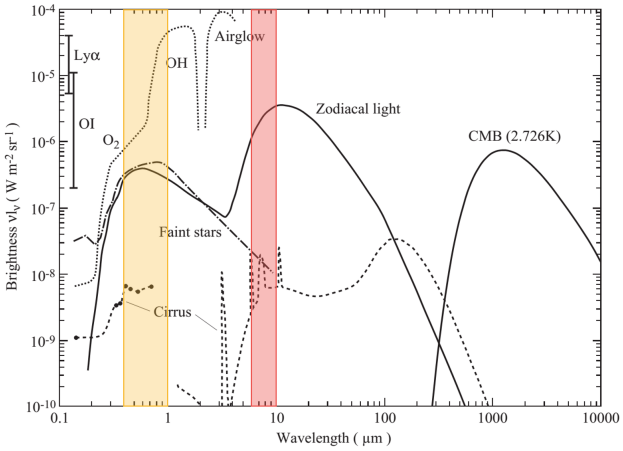

Fig. 14 Overview of the night-sky brightness outside the lower terrestrial atmosphere and at high ecliptic latitudes, as a function of wavelength. Source: [42].

can thus be neglected. On the other hand, at the VIS wavelengths of the space-based telescope, the contributions due to zodiacal light and starlight are of the same order[‡‡]. The implementation of the noise due to faint stars is outside the scope of this paper, as it includes the use of a patched stellar catalogue and discrete sources on the detector, which is in contradiction with the assumption of a Gaussian shape of the light source. To solve this, a limiting apparent visual magnitude is defined as a detection condition for the VIS space-based telescope. More details on the detection process are given next in Sec. VI.A. In this paper, the background signal is then mainly driven by the zodiacal light, neglecting thus the contribution of any other sources.

At VIS wavelengths, the background's irradiance due to zodiacal light has been taken from [43] and [42], which provide tabulated zodiacal fluxes as a function of ecliptic latitude and longitude. The zodiacal light data is given at a wavelength of 550 nm, in terms of $S10_\odot$[§§] units and on a grid of 5°×5°, which is sufficiently fine so that linear interpolation to arbitrary angles is accurate. Since the zodiacal light brightness is provided for an observer at Earth, the zodiacal background is assumed to vary with heliocentric distance according to Fig. 56 in [42] for the space-based surveys at other locations. At IR wavelengths, the background's irradiance due to the thermal emission from zodiacal dust is computed using the three-dimensional density model by [44]. This zodiacal light model consists of the integral along the line-of-sight of the product of a source function and a three-dimensional density distribution function, which is composed by three distinct components: a smooth cloud, three dust bands, and a circumsolar dust ring. The model is explained in full detail in [44]. Similar to the VIS case, the zodiacal brightness is computed for an observer at Earth, and it is thus assumed that the infrared zodiacal light varies with heliocentric distance according to Fig. 55 in [42] for the space-based surveys at other locations.

[‡‡]Note that the OH airglow emission below 2μm is not relevant for space-based telescopes as it is due to Earth's atmosphere, which is purposely left outside the viewing zones.

[§§]$S10_\odot$ is a unit of brightness, defined as solar type stars of tenth magnitude per degree squared ($S10_\odot = 1.28 \cdot 10^{-8}$ Wm^{-2}sr$^{-1}\mu^{-1}$) [42].

VI. Simulation of Sky Surveys

This section presents and discusses the results of the sky surveys using the different space-based survey systems considered. The section starts by stating all the assumptions that are considered in the simulations in Sec. VI.A. The performance of each space-based survey system in providing warning for imminent Earth impactors is determined and discussed in Sec. VI.B. These space-based observations are then compared to existing ground-based surveys in Sec. VI.C, in order to demonstrate the benefit and necessity of space-based surveys. Finally, Section VI.D estimates the improvement in the performance when not one but multiple space-based telescopes at the same location are considered.

A. Survey Simulation Assumptions

The space-based survey model assumes that a NEO is detected in an image when the following conditions are satisfied simultaneously:

- The NEO is inside the FOR of the telescope.
- The NEO is bright enough to be detected, *i.e.*, satisfies the sensitivity of the telescope (see Table 1).
- The SNR of the NEO is equal or greater than five.
- The Earth and/or the Moon are not in the FOV of the telescope.

Then, in order to observe an object moving with respect to the fixed stars, the survey needs to take a sequence of images of the same field of the sky shortly after each other in order to be able to form a tracklet, which is simply the assembly of at least two observations pertaining to a single object [45]. In general, two or three tracklets are required in order to uniquely determine the orbit of the object with classical methods for orbit determination. However, another way to determine the orbit of an object from only one tracklet is to apply the systematic ranging technique. This orbit determination algorithm is especially tailored to dealing with imminent impactors, for which the time interval covered by the observations is generally short and it is not possible to build more than one tracklet [46]. Therefore, in this paper, it is assumed that a NEO can be observed if at least one tracklet can be built, which consists of four detections/images taken $\sim$1 – 1.5 hours apart over a 9–hour span[¶¶].

As a last remark, the space-based surveys that are simulated do not follow any survey cadence. Instead, any NEO that satisfies the detection conditions for which a tracklet can be built is considered as a 'potential' observed object. During post-processing, the pointing direction during the surveying of each object is cross-checked in order to see whether the telescope would be able to cope with the sequence of observations. In case that more than one pointing direction during the same time interval appears to be required, the maximum number of non-overlapping observations of the objects with the longest warning times are kept and the rest are discarded.

[¶¶] This value has been taken from NASA's NEOCam's survey cadence [5].

Table 3 Detection rates for different orbit locations and wavebands of the space-based telescope, using four different populations of impacting NEOs and one year of observation window before impact.

Location	Band	p_v	Population #1 (Distributed H)		Population #2 (H=22)	Population #3 (H=24)	Population #4 (H=26)
			Unrefined	Refined			
SE sub$-L_1$	VIS	0.14	*91.76%*	48.27%	51.94%	45.74%	42.88%
	TIR	0.05	*59.34%*	40.08%	60.75%	51.37%	40.02%
		0.14	*58.83%*	39.09%	55.16%	43.57%	37.05%
		0.25	*56.83%*	36.64%	50.71%	24.39%	35.54%
SV $L_{3,4,5}$	VIS	0.14	*3.1%*	2.98%	48.59%	14.73%	0.69%
	TIR	0.05	*56.22%*	29.66%	48.10%	43.66%	20.97%
		0.14	*26.52%*	16.69%	44.92%	33.41%	6.28%
		0.25	*11.1%*	8.16%	43.61%	25.54%	1.26%

B. Detection and Warning Efficiency of each Space-based Survey System

As mentioned in Sec. I, two different mission candidates and two wavelength bands are considered, and thus, a total of four space-based survey systems are simulated. Using the four populations of Earth impactors and the space-based NEO observation tool, discussed previously in Sec. V, the performance of each space-based survey system is determined. The performance of each space-based survey system is defined in terms of the following results: detection rate (*i.e.*, number of observed and missed impacts), time between observation and impact (*i.e.*, warning time) and observed and missed impactors as a function of absolute magnitude and size.

Since the distribution of objects in the NEO population is in absolute magnitude H, and not in size, three different values of the albedo p_v have been considered in the simulations: 0.05, 0.14 and 0.25. However, at VIS wavelengths, the initial results from test simulations (see Appendix A) show that this parameter does not have a major impact on the results, and is thus set to a default value of 0.14. Furthermore, at IR wavelengths, the test simulations also show that the performance using the STM and the NEATM is very similar, but only the more accurate NEATM is considered in this section since it yields slightly worse results. More details on this software tuning are given in Appendix A.

Survey of Earth impactor population distributed in absolute magnitude

Table 3 presents the detection rates for each space-based survey system considered, using four different populations of impacting NEOs and an observation window of one year before impact. The first survey results to be discussed are the ones obtained using the Earth impactor population #1, which follows the expected distribution in H (see Sec. V.C).

First, regarding the orbit location of the space-based telescope, it is possible to see that the SE mission candidate clearly outperforms the SV case for both the VIS and TIR wavebands. Moreover, it is important to highlight that the 'un-refined' survey results for the SE mission candidate, which do not take into account the pointing direction of the

observations, show that the VIS case is able to detect approximately 90% of the objects, and the TIR case up to 60%. Since the NEO population consists of Earth impactors, the space-based telescope at the SE sub$-L_1$ point acts as a 24/7 security camera, that is able to capture (almost) all NEOs before impact. Therefore, this orbit location is ideal to detect Earth-impacting objects, much more in advance than with existing ground-based facilities, as will be discussed later in Sec. VI.C. Instead, the performance of the mission candidate at the SV L_3, L_4 and L_5 points highly depends on the likelihood of the NEO passing through the FOR on its collision course with Earth. Consequently, the detection rates are much smaller for the SV case than for the SE case but may improve if the observation window is longer.

Regarding the waveband, at first look, the space-based telescope at VIS wavelengths seems to perform slightly better than at IR wavelengths, as the best survey results are obtained using a VIS telescope at the SE sub$-L_1$ point, with a detection rate of almost 50% of the impactors. However, the considerable improvement of the SV results from the VIS to the TIR case indicates that surveying at TIR wavelengths is more effective. The slight improvement of the visible space-based telescope over the TIR one at the SE orbit location can be attributed to a FOR that is closer to Earth, thus observing the objects on their collision courses for a longer time. This is shown in the form of a histogram in Fig. 15, which represents the solar elongation, for an observer on Earth, at the moment of detection of all the observed impactors by both space-based surveys. It is possible to see how the TIR observations are mainly obtained at smaller solar elongations, from approximately 5° to 125°, while the VIS observations reach values up to 170°. Since many observations at visible wavelengths are made at larger solar elongations, *i.e.*, close to opposition ('behind' Earth), where the NEOs are at their brightest, the warning times for these observations are expected to be considerably shorter because the NEOs are most likely to also be closer to the impact point.

Figure 16 then shows the fraction of impactors observed as a function of the warning time for each space-based survey system considered and an albedo of 0.14, together with the ground-based results using ESA's Flyeye telescope, which are presented and discussed later in Sec. VI.C. This plot clearly shows the advantage of surveying NEOs in IR; *e.g.*, it detects almost 15% of the objects with a warning time of at least one month before impact, while the VIS telescope can only detect less than 5%. For the SE mission candidate, the two wavebands get the same detection rates for a warning time up to one week, and then the VIS one slowly starts to obtain larger detection rates for shorter warning times. Nonetheless, while all the detections made by the TIR telescope have a warning time of at least one day, there are many observations by the VIS telescope that have a warning time of less than 12 hours, which might not be long enough depending on the size of the object. For the SV mission candidate, the TIR case not only provides a larger detection rate, but also longer warning times. Since both VIS and TIR surveys at the SV $L_{3,4,5}$ points are centred at opposition (see Fig. 11b), the VIS space-based telescope does not have the additional advantage of a wider FOR over the IR telescope, as was noted above for the SE mission candidate. As a result, the TIR space-based telescope ultimately leads to better results for the same observation window.

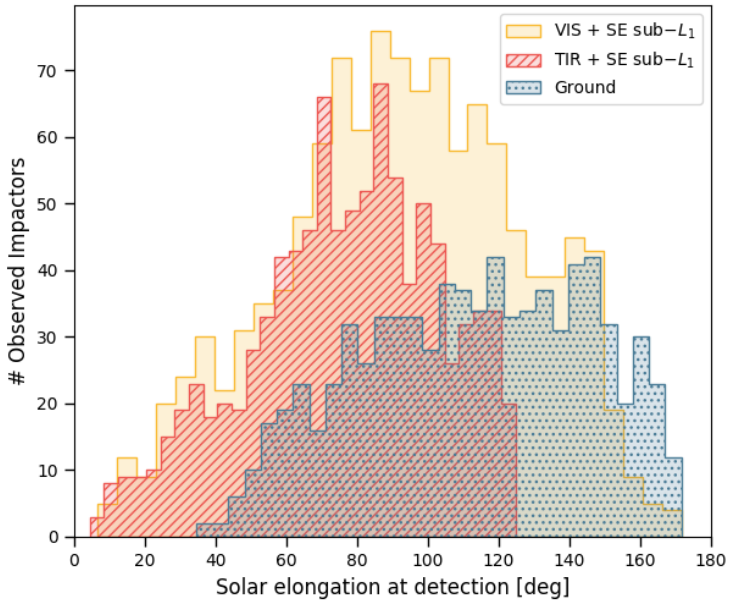

Fig. 15 Histogram of the solar elongation, from an observer on Earth, at the detection time of all the observed impactors by a VIS and TIR space-based survey at the SE sub$-L_1$ point, and a ground-based survey.

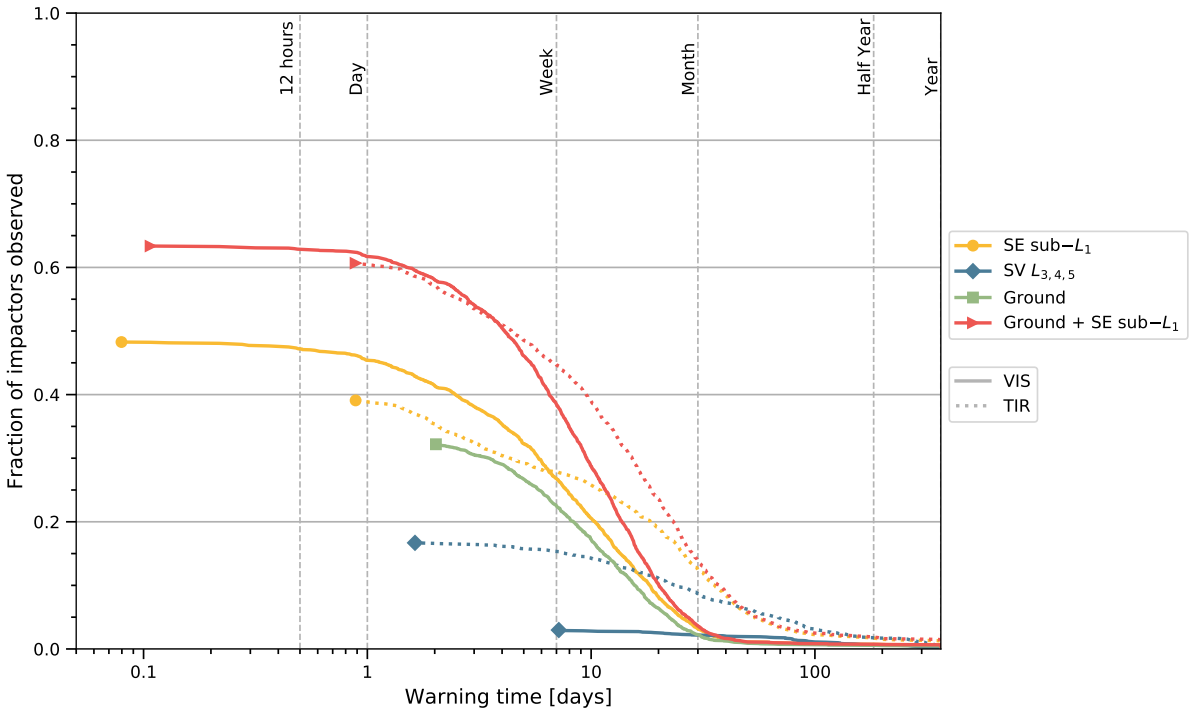

Fig. 16 The fraction of impactors observed at a given time before impact, for different orbit locations and wavebands of the space-based telescope, using NEO population #1. The ground-based results using ESA's Flyeye telescope are also presented individually and combined with the space-based survey results.

Survey of Earth impactor population for a constant absolute magnitude

This section discusses the survey results obtained using NEO populations #3, #4 and #5 (see Sec. V.C) in order to determine the performance of the space-based telescopes as a function of absolute magnitude and size. The detection rates for each space-based survey system considered are also presented in Table 3. In addition, Fig. 17 shows the fraction of impactors observed as a function of the warning time, for the three values of absolute magnitude considered.

First, for an absolute magnitude of $H = 22$ (population #2, see Fig. 17, top left), it is possible to see that the detection rates obtained in both mission candidates are fairly similar, with the SE case outperforming the SV case by only ∼3% and ∼10% at VIS and TIR wavelengths, respectively. Moreover, with similar detection rates, the SV mission candidate obtains longer warning times at VIS wavelengths than the SE case. This clear improvement over the first survey results indicate that, while the mission candidate at the SV L_3, L_4 and L_5 points is not a good option for observing the smaller objects in the population, *i.e.*, fainter than $H = 22$, it is a potential candidate for discovering larger NEOs. Furthermore, contrary to what was observed for NEO population #1, the detection rate for the SV case at VIS wavelengths is slightly better than at IR wavelengths. On the other hand, the mission candidate at the SE sub$-L_1$ case not only obtains longer warning times, but also detects more objects at IR wavelengths than at VIS.

Then, when considering fainter objects with an absolute magnitude of $H = 24$ (population #3, see Fig. 17, top right), the detection rates for the SV candidate starts to decrease more rapidly than the SE case, especially for the VIS waveband, which drops from almost 49% to approximately 15%. Therefore, the TIR waveband is again the better option for surveying NEOs with $H = 24$ with a detection rate of ∼33% obtained in the SV mission candidate, which also obtains significantly longer warning times. For the SE case and an absolute magnitude of $H = 24$, surveying at VIS wavelengths starts again to perform slightly better than at IR, with detection rates of ∼46% and ∼44%, respectively, which was not the case for $H = 22$. However, longer warning times are obtained by the TIR waveband.

Finally, for an absolute magnitude of $H = 26$ (population #4, see Fig. 17, bottom left), both the detection rates and warning times obtained are very similar (slightly worse) to the first survey results using the NEO population distributed in H, which is to be expected as it mostly contains small objects.

To summarise the analysis in this subsection and the previous subsection, a VIS space-based telescope located at the SV L_3, L_4 and L_5 points is a good candidate for the survey of larger and brighter objects than $H = 22$. However, considering that the expected size-frequency distribution of a NEO population consists mostly of smaller objects, the better candidate is either a VIS or TIR space-based telescope located at the SE sub$-L_1$ point. While a visible space-based telescope at this orbit location detects more objects, a TIR space-based telescope generally provides longer warning times. Next, Sec. VI.C performs a trade-off between these two wavebands in order to determine which option is better when combined with the observations performed by the existing ground-based surveys, and determines the benefit of launching a space-based telescope. Note that, for the following simulations and discussions, the population of Earth impactors to be used is #1 as it represents a more realistic population of NEOs.

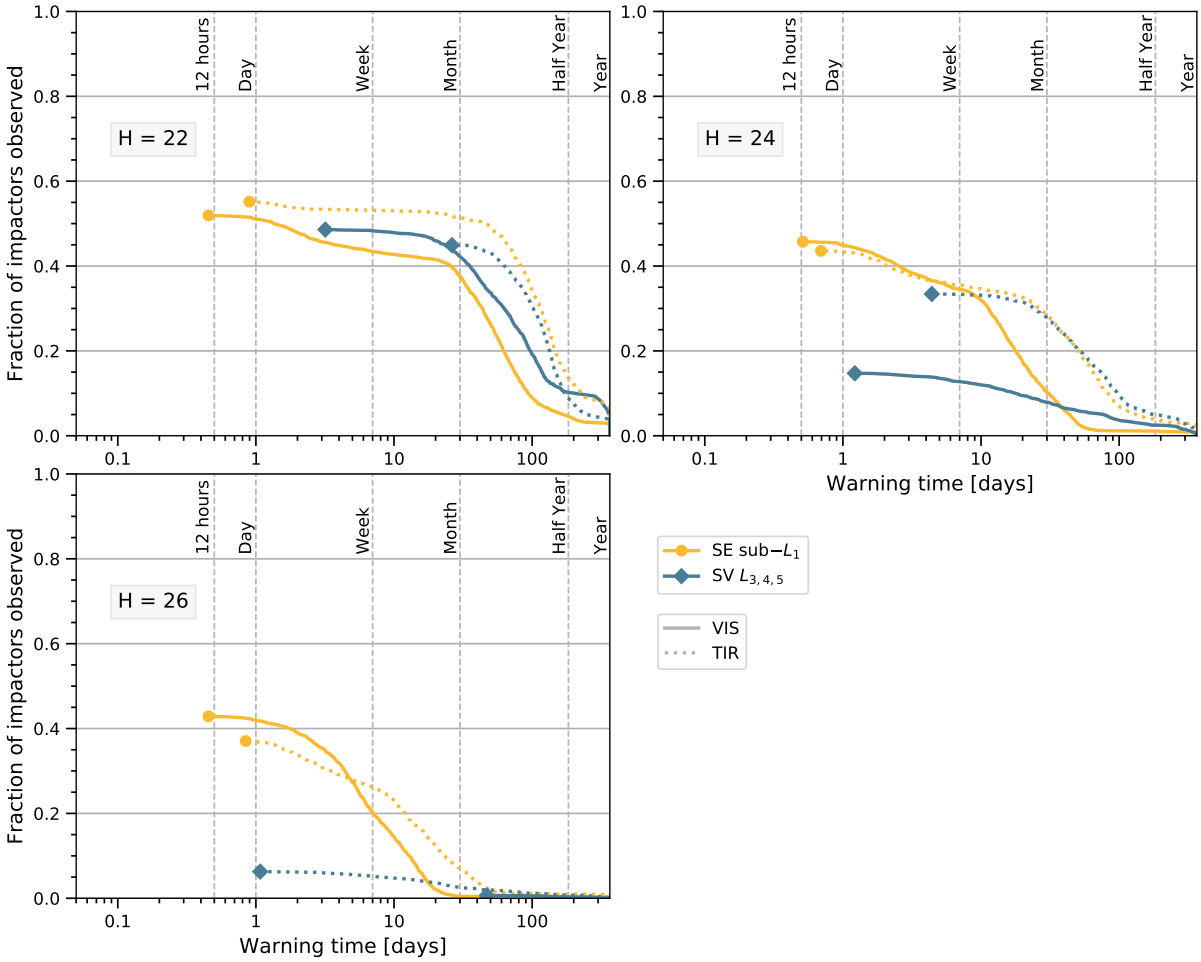

Fig. 17 The fraction of impactors observed at a given time before impact, for different orbit locations and wavebands of the space-based telescope, using NEO populations #2 (top left), #3 (top right) and #4 (bottom left).

C. Benefit of Space-based Surveys to existing Ground-based Surveys

Although it does not exist yet, ESA's first NEO survey telescope, the Flyeye telescope, is expected to be deployed in Monte Mufara (Sicily) in 2020 and is designed to search for the very small and faint NEOs that are expected to collide with Earth [2][47]. The performance of this ground-based telescope in providing warning for (smaller) Earth-impacting NEOs has been estimated previously in the work by [2], within the framework of activities of ESA's Planetary Defence Office. In this paper, the same software tool is used to determine the observation of the NEO population considered using the Flyeye telescope.

Table 4 presents the detection rates obtained by a VIS and TIR space-based survey at the SE sub−L_1 point, using NEO population #1 and a default albedo of 0.14, combined with the ground-based results using ESA's Flyeye telescope. First, it is important to highlight that, independent of the space-based telescope, the Flyeye telescope is able to detect up to 32% of Earth impactors, which is similar to the space-based results for the chosen SE orbit candidate at TIR

Table 4 Detection rates for different orbit locations and wavebands of the space-based telescope, using NEO population #1, combined with the ground-based results using ESA's Flyeye telescope.

Location	Band	p_v	Only space	+ Ground
SE sub$-L_1$	VIS	0.14	48.27%	63.36%
	TIR	0.14	39.09%	60.67%

wavelengths. However, when combining all observations from ground- and space-based surveys, the detection rates are doubled. This indicates that space-based surveys are necessary in order to achieve longer warning times and also to detect those that are missed by existing ground-based telescopes. As shown in Fig. 15, ground-based surveys are only able to observe objects with a minimum solar elongation of approximately 40°, while space-based telescopes can survey and detect objects much closer to the Sun.

Second, Table 4 also shows how the difference in results between the VIS and TIR wavebands at the SE sub$-L_1$ point decreases considerably when combined with the ground-based results, from 10% to 3%, respectively, which indicates that surveying at IR wavelengths better complements ground-based surveys. This can also be seen in Fig. 15; many observations obtained at larger solar elongations with the VIS space-based telescope, that cannot be reached when surveying at IR wavelengths, can also be obtained with ground-based surveys. In addition, the warning times obtained with the TIR space-based telescope are generally longer. As shown in Fig. 16, both space-based telescopes are able to detect the same number of Earth impactors with a warning time of at least one day and thus, the slight increase in the detection rates for the VIS case is only due to detecting NEOs with a warning time shorter than a day.

Therefore, it can be concluded that the best way to detect as many Earth impactors as soon as possible is combining a TIR space-based telescope at the SE sub$-L_1$ point with existing ground-based telescopes.

D. Estimation of the increase in Performance with Multiple Space-based Telescopes at the SE sub$-L_1$ point

As discussed in Sec. VI.B, many 'potential' detections have been discarded due to the fact that the space-based telescope can only point in one direction at any one time. Therefore, this section analyses the performance of a TIR space-based survey system at the SE sub$-L_1$ point consisting of one, two and three space-based telescopes. Despite the fact that the VIS space-based telescope has been discarded due to shorter warning times obtained with respect to the TIR option, the results for a VIS space-based survey system at the SE sub$-L_1$ point consisting of one, two and three space-based telescopes have also been included, in order to further justify the choice of waveband.

Table 5 presents the detection rates of up to three space-based telescopes in both wavebands, using NEO population #1 and a default albedo of 0.14. The combined results with the ground-based ones using ESA's Flyeye telescope are also presented. First, it is important to highlight how the increase in performance with the number of space-based telescopes is significantly different for each waveband; by using three telescopes, the VIS results improve from ~48%

Table 5 Detection rates for different wavebands and number of space-based telescopes, using NEO population #1, combined with the ground-based results using ESA's Flyeye telescope.

Location	Band	p_v	Only space-based telescopes			+ Ground		
			One	Two	Three	One	Two	Three
SE sub$-L_1$	VIS	0.14	48.27%	73.36%	84.58%	63.36%	81.44%	90.17%
	TIR	0.14	39.09%	52.26%	56.02%	60.67%	71.44%	74.46%

up to almost 85%, while the TIR results only go from ~39% to approximately 56%. Therefore, although the detection rates of only one space-based telescope are fairly similar, three VIS space-based telescopes are able to detect up to 30% more Earth impactors than three TIR space-based telescopes. Moreover, when combined with ground-based surveys, this survey system is able to detect up to 90% of all NEOs. On the other hand, when combined with ground-based results, the difference between VIS and TIR surveys reduces, as three VIS space-based telescopes are now able to detect up to 15% more (instead of 30%) of Earth impactors than three TIR space-based telescopes. This again implies that surveying at IR wavelengths better complements ground-based surveys, as also observed in Sec. VI.C. In addition, for both wavebands, the major improvement comes from adding a second space-based telescope, as the results improve by 18% and 11% at VIS and TIR wavelengths, respectively, with respect to one space-based telescope. When adding a third one, this improvement is reduced by more than a half, as the results now improve only by 9% and 3% at VIS and TIR wavelengths, respectively, with respect to two space-based telescopes. Therefore, if only two space-based telescopes and ground-based surveys are considered, the difference between the VIS and TIR results is only 10%.

Figure 18 then shows the fraction of impactors observed as a function of the warning time, for the two wavebands and different number of telescopes considered, together with the ground-based results. As discussed previously, there is not a significant difference in results between two and three space-based telescopes. Using only two space-based telescopes, and combining the observations with the existing ground-based surveys, shows nearly the same performance as launching three telescopes (without use of ground telescopes). Furthermore, note that only one ground-based telescope (in the northern hemisphere) has been considered in the simulations; it is to be expected that many of both missed and observed impactors by the space-based surveys, especially at VIS wavelengths and large solar elongations, would be obtained by another ground-based survey, most likely in the southern hemisphere.

Since the first main goal of the space-based survey system is to provide warning for imminent impactors, the key factor to be considered are the warning times, and the TIR waveband thus still remains the better option over the VIS waveband. Moreover, surveying at TIR facilitates the discovery of those NEOs coming from the day-side that are missed by existing ground-based surveys. Regarding the number of space-based telescopes, it is highly questionable whether the additional cost of a third telescope is worth the 3% increase in observed NEOs, especially since those extra observations have a very short warning time. Therefore, it is concluded that the best NEO survey system consists of

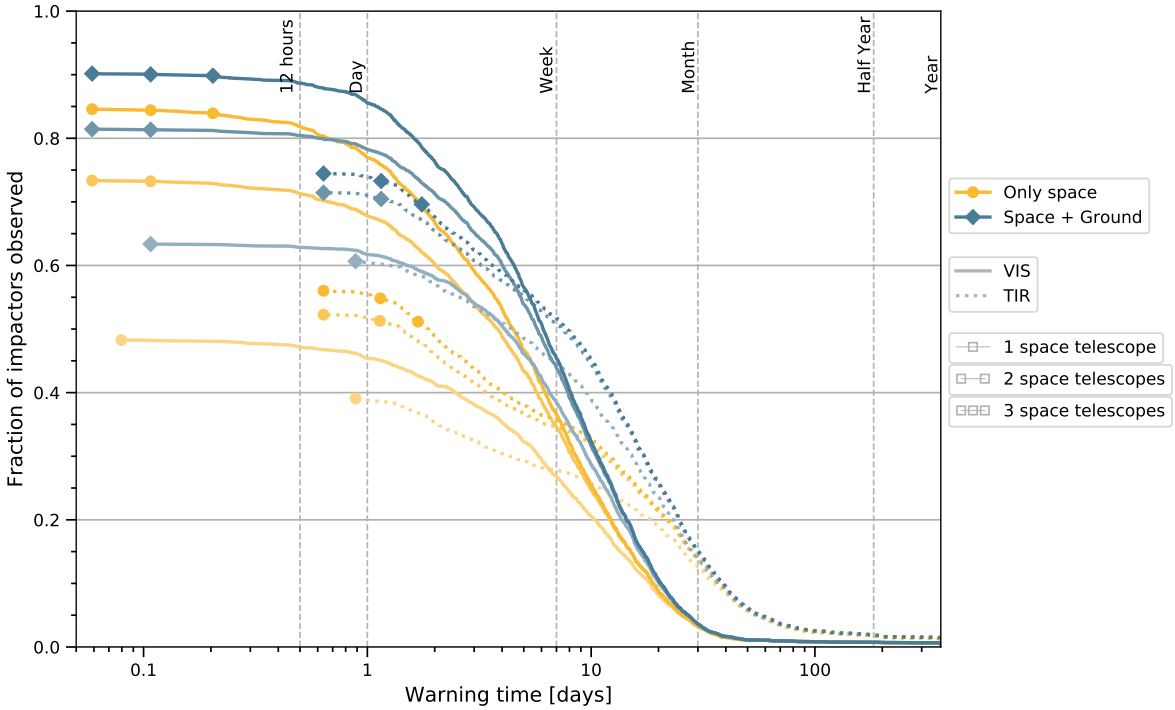

Fig. 18 The fraction of impactors observed at a given time before impact, for different wavebands and number of space-based telescopes at the Sun-Earth sub$-L_1$ point, using NEO population #1. The ground-based results using ESA's Flyeye telescope are also presented individually and combined with the space-based survey results.

one or two TIR space-based telescopes at the SE sub$-L_1$ point, combined with ground-based surveys.

VII. Transfer Trajectory Design

Now that the operational orbit of the space-based telescope is selected, the aim is to find a time-optimal, solar-sail propelled transfer trajectory from Earth's vicinity to the solar-sail halo orbit around the SE sub$-L_1$ point. To this aim, the transfer model is first described in Sec. VII.A. Then, the optimisation problem to be solved in the CR3BP is presented in Sec. VII.B. Once an optimal solution is found, an innovative multiple shooting differential corrector to find feasible transfer trajectories in the ER3BP is explained in Sec. VII.C. Finally, the resulting transfer trajectory in the ER3BP is presented in Sec. VII.D.

A. Transfer Model

This section describes the transfer problem to be solved, within the dynamical framework of the CR3BP, and presents the proposed approach for finding a time-optimal solution.

1. Launch from Earth

In this paper, a ride-shared launch on ESA's Euclid mission is assumed, which is expected to be launched in 2020 and injected into a large-amplitude ($\sim 10^6$ km) halo orbit around the SE L_2 point[***], as shown in Fig. 19 A very detailed design of the launch scenario and window can be found in [48]. However, since it is not possible to find any concrete reference values and for the purpose of performing a preliminary mission analysis of a space-based telescope to detect Earth-impacting NEOs, only the size of Euclid's orbit is adopted in this paper, independently of launch date and any other constraints. To this aim, a family of halo orbits around the L_2 point in the Sun-Earth CR3BP is generated, following the approach in [27]. Then, a continuation in both y- and z-amplitudes is conducted to obtain LPOs with in-plane amplitudes of $\sim 8 \cdot 10^6$ km (see Fig. 20).

2. Transfer phases

The solar-sail spacecraft is assumed to travel together with Euclid for some time, t_{euclid}, before deploying the solar sail and diverting away from Euclid's trajectory, towards the SE sub$-L_1$ region. The transfer trajectory can thus be divided into two phases: an un-propelled shared-transfer phase, and a solar-sail propelled phase.

The first transfer phase is modelled as an asymptotic trajectory on the stable manifold associated to the Euclid's halo orbit around the SE L_2 point that comes close to Earth. To find the stable invariant manifold associated to the orbit in Fig. 20, the method defined in [49] is used. The resulting stable manifold is shown in Fig. 20. The selected transfer trajectory along the manifold is also highlighted in red, which approaches Earth at a distance similar to geostationary (GEO) altitude.

The motion of the solar-sail spacecraft during the second phase of the transfer is simply described by the equations of motion given in Eq. (1), *i.e.*, in the solar-sail CR3BP. The initial and final state vectors of this phase must coincide

***Euclid - Mission Operations. URL `https://sci.esa.int/web/euclid/-/46661-mission-operations` (Access date 2019-11-13)

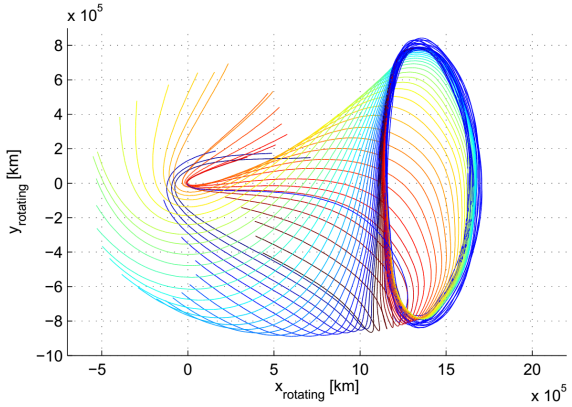

Fig. 19 Stable manifold of Euclid's operational orbit and transfer trajectory. Source: [48].

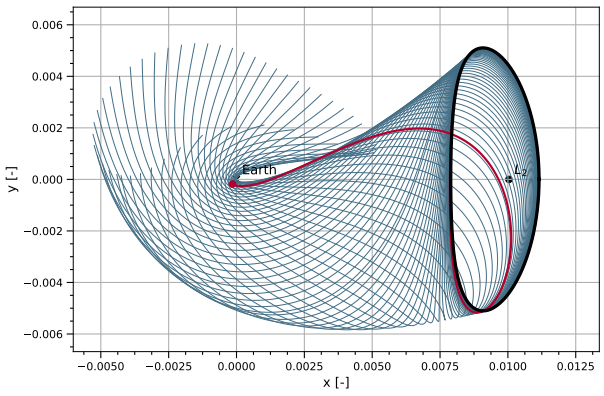

Fig. 20 Stable manifold associated to a halo orbit around the L_2 in the Sun-Earth CR3BP, similar to Euclid's operational orbit, and transfer trajectory.

with state vectors pertaining to the selected stable manifold trajectory and the targeted halo orbit around the SE sub$-L_1$ point, respectively. A schematic of this transfer model is shown in Fig. 21.

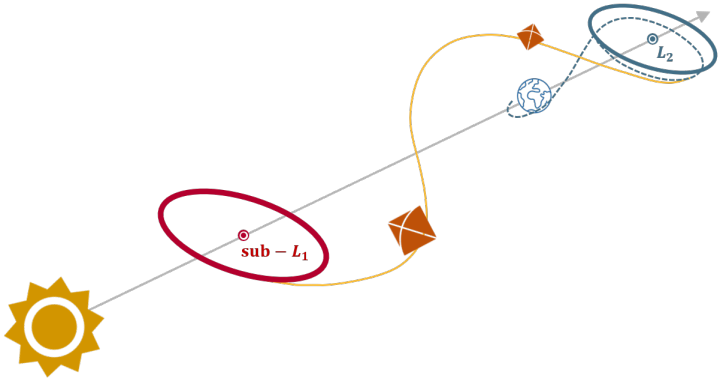

Fig. 21 Schematic of the transfer model (not to scale). The dashed blue line indicates the un-propelled shared-transfer phase from Earth's vicinity towards the SE L_2 region, together with ESA's Euclid spacecraft. The solid yellow line represents the solar-sail propelled phase from deployment until injection into the halo orbit around the SE sub$-L_1$ point (in red).

3. Trajectory design process

This section presents a novel approach to finding a time-optimal, solar-sail propelled transfer trajectory that satisfies the problem defined in Sec. VII.A.2. This approach is a slight modification to similar methods in literature, which has been proven successful in finding locally time-optimal trajectories in the solar-sail CR3BP (see Reference [50]), and is adapted here to meet the (slightly) constrained initial and end conditions of the transfer. The approach consists of three steps: in the first step, a genetic algorithm is used to find near-feasible transfer trajectories based on a few design variables and the search for a heteroclinic connection between the LPOs at the SE L_1 and L_2 points. These near-feasible transfer trajectories are then used as a first guess for a multiple shooting differential correction algorithm to find feasible transfer trajectories for a fixed time-of-flight (TOF). In the third and last step, a continuation scheme in eccentricity is applied in order to find a transfer trajectory in the ER3BP that targets the designed orbit in Sec. III.

B. Optimisation Problem

This section defines the optimisation problem to be solved in the first step of the design process, and the chosen optimisation method to handle it. The resulting near-feasible transfer trajectories are presented and discussed at the end of the section.

1. Problem Statement

The first step of the transfer trajectory design process aims at finding a heteroclinic connection between the halo orbit around the SE L_2 in Fig. 20 and the halo orbit around the SE sub$-L_1$ in Fig. 4 in the CR3BP. This transfer

trajectory can be divided into two segments:

1) An initial segment propagated forwards in time from the launch conditions defined in Sec. VII.A.1, *i.e.*, from the moment the sail deploys and the solar-sail spacecraft diverts away from Euclid's trajectory.
2) A final segment propagated backwards in time from the insertion into the solar-sail halo orbit around the SE sub$-L_1$ point.

The aim is then to find a trajectory that links these two segments together. Note that the solar-sail can adopt a different, but constant, sail attitude along each of the two segments. Therefore, the problem is parametrised by the following set of decision variables:

$$\mathbf{y} = \begin{bmatrix} t_{\text{euclid}} & \alpha_{s,0} & \delta_{s,0} & \alpha_{s,f} & \delta_{s,f} & \tau_f \end{bmatrix} \tag{22}$$

where the subscripts '0' and 'f' indicate the initial and final segments defined above. Therefore, the variables $\alpha_{s,0} \in \left[0, \frac{\pi}{2}\right]$ and $\delta_{s,0} \in [-\pi, \pi]$ represent the sail attitude in the initial segment, and $\alpha_{s,f} \in \left[0, \frac{\pi}{2}\right]$ and $\delta_{s,f} \in [-\pi, \pi]$ represent the sail attitude in the final segment. The parameter $\tau_f \in [0, 1]$ determines the insertion point along the targeted halo orbit, which is obtained by propagating the initial conditions of the orbit, $\mathbf{x}_{\text{SE-CR3BP},0}$, from t_0 to $\tau_f P_{\text{p.o}}$, where $P_{\text{p.o}}$ indicates the period of that orbit. Lastly, as mentioned in Sec. VII.A.2, the parameter $t_{\text{euclid}} \in [0, 300\,\text{days}]$ indicates the time that the solar-sail spacecraft travels together with ESA's Euclid spacecraft along Euclid's transfer trajectory (see Fig. 20).

In order to find the optimum values of the decision variables, a multi-objective optimisation method is applied, based on the non-dominated sorting genetic algorithm II (NSGA-II), which is imported from the Python library 'Platypus'[†††]. The two objective functions of this optimisation problem are as follows: the TOF, from GEO altitude until injection into orbit, and the so-called infeasibility, ϵ_I, which is computed as the minimum Euclidean norm in dimensionless phase space between any two points of the two segments propagated in time for two years, *i.e.*:

$$\epsilon_I = \sqrt{\epsilon_R^2 + \epsilon_V^2} \tag{23}$$

where ϵ_R and ϵ_V are the errors in dimensionless position and velocity, respectively.

The output of this algorithm is given in the form of a Pareto front, which contains a set of optimal individuals that vary in TOF and infeasibility. Although all these individuals are potential solutions, the one with minimum ϵ_I will be selected in order to facilitate the search for feasible transfer trajectories later in Sec. VII.C. Several Pareto fronts are obtained as the algorithm is run for different values of random seeds in order to decrease the uncertainty concerning the chosen optimum. Each run uses a population of 20 $\times$ the number of decision variables, and a total of 10 000 function evaluations.

[†††] Platypus – Multiobjective Optimization in Python. URL `https://platypus.readthedocs.io/en/latest/` (Access date 2019-11-26)

2. Results – Near-feasible transfer trajectories

Table 6 presents the results of the optimisation algorithm for different random seeds. Although there is a wide range in the solutions, the general trend is focused on near-feasible transfer trajectories with a TOF around 430 days and a discontinuity in phase space in the order of $\sim 10^{-4}$. Based on these results, the 'best' optimum is found for a seed equal to 3 that yields a TOF of almost 438 days and a discontinuity of $7{\cdot}10^{-4}$, which corresponds to an error in position and velocity of 89 629 km and 10.80 m/s, respectively. The full Pareto front for a seed value of 3 is shown with blue circle-shaped markers in Fig. 22.

Table 6 Results of the multi-objective optimisation algorithm for different random seeds.

Seed	Infeasibility			TOF [days]
	ϵ_I	ϵ_R	ϵ_V	
3	$7.00{\cdot}10^{-4}$	$5.99{\cdot}10^{-4}$	$3.63{\cdot}10^{-4}$	437.54
7	$1.19{\cdot}10^{-3}$	$1.02{\cdot}10^{-3}$	$6.26{\cdot}10^{-4}$	424.55
127	$1.51{\cdot}10^{-3}$	$1.39{\cdot}10^{-3}$	$5.87{\cdot}10^{-4}$	263.31
1986	$1.09{\cdot}10^{-3}$	$7.78{\cdot}10^{-4}$	$7.29{\cdot}10^{-4}$	434.54
151086	$1.05{\cdot}10^{-3}$	$1.02{\cdot}10^{-3}$	$2.17{\cdot}10^{-4}$	453.93

A further local refinement around this found optimum is conducted with a two-step approach, where the optimum values of the decision variables are first varied within ±10%, and then, the newly found values are varied again within ±5%. Figure 22 shows the improvement made in the local refinement through the use of a cross- and diamond-shaped marker. In the first step of the refinement, there is a significant improvement in the feasibility and a slight decrease in

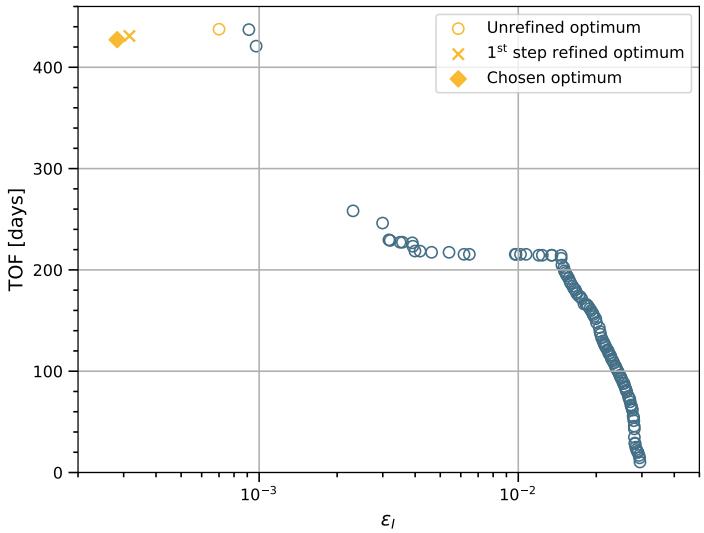

Fig. 22 Pareto front obtained in the multi-objective optimisation problem with a seed equal to 3, and the subsequent refinement around the found optimum.

the TOF. The second and last step of the refinement does not significantly vary this optimal individual, which ensures a sufficient convergence of the method. Therefore, the chosen optimum yields a TOF of 427.25 days and an infeasibility of $2.83{\cdot}10^{-4}$, which corresponds to an error in position and velocity of 35 527 km and 4.6 m/s, respectively. The resulting near-feasible trajectory is shown in Fig. 23, which clearly shows the position error at the connection between the two segments. The optimal values of the decision variables for this solution are:

$$\begin{aligned}\mathbf{y}_{\text{opt}} &= \left[t_{\text{euclid}} \quad \alpha_{s,0} \quad \delta_{s,0} \quad \alpha_{s,f} \quad \delta_{s,f} \quad \tau_f\right] \\ &= [156.15\,\text{days} \quad 76.53^\circ \quad 50.83^\circ \quad 18.68^\circ \quad 83.47^\circ \quad 0.995]\end{aligned} \tag{24}$$

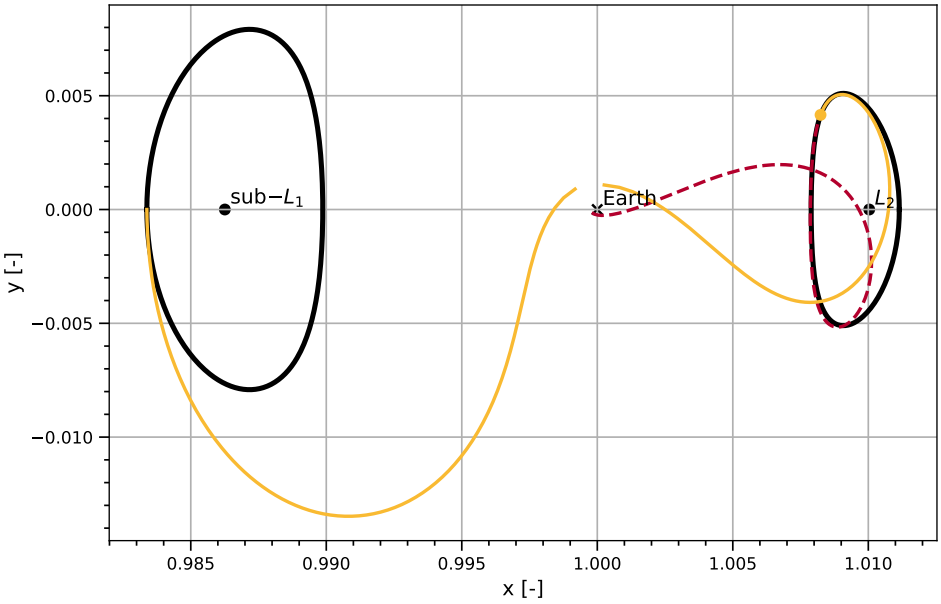

Fig. 23 Near-feasible transfer trajectory in the SE CR3BP. The dashed red line indicates the un-propelled shared-transfer phase and the solid yellow line indicates the solar-sail propelled phase.

C. Feasible Transfer Trajectories

Since none of the potential solutions obtained by the optimisation algorithm results in a feasible transfer trajectory ($\epsilon_I = 0$), a multiple shooting differential correction algorithm is applied to find a feasible transfer trajectory, using as a first guess the chosen optimal solution of Sec. VII.B.2.

1. Two–step multiple shooting differential corrector with solar sail

The multiple shooting differential corrector implemented in this section is a modification of the one used previously in Sec. III and Sec. IV, such that the sail attitude is also included in the decision vector at each node. Therefore, for a reference trajectory discretised in $n-1$ segments that are connected through n nodes, the decision vector $\mathbf{p}_i$ at each

node i contains a point in phase space of the CR3BP, $\mathbf{x}_i$, a cone angle, $\alpha_{s,i}$, a clock angle, $\delta_{s,i}$, and the time at the node, t_i, *i.e.*:

$$\mathbf{p}_i = \begin{bmatrix} \mathbf{x}_i & \alpha_{s,i} & \delta_{s,i} & t_i \end{bmatrix}^T \quad \text{for } i \in \{1, 2, \cdots, n-1\} \tag{25}$$

At the last node, the cone and clock angles do not need to be defined as they are prescribed by the sail attitude required to maintain the solar-sail halo orbit, and thus, those decision vectors only contain $\mathbf{x}_n$ and t_n.

The aim of the multiple shooting differential corrector is to find a feasible transfer trajectory for a given TOF, T_f, with constraints g_0 and g_f on the state vectors at the initial and last nodes. The resulting trajectory must satisfy the dynamics of Eq. (7) along each segment and is obtained as the solution to the following problem:

$$g_0\left(\mathbf{p}_1\right) = 0 \tag{26}$$

$$\phi_{t_{i+1}}\left(\mathbf{x}_i, \alpha_{s,i}, \delta_{s,i}, t_i\right) - \mathbf{x}_{i+1} = 0 \quad \text{for } i \in \{1, 2, \cdots, n-1\} \tag{27}$$

$$g_f\left(\mathbf{p}_n\right) = 0 \tag{28}$$

$$t_n - T_\mathrm{f} = 0 \tag{29}$$

where $\phi_{t_{i+1}}\left(\mathbf{x}_i, \alpha_{s,i}, \delta_{s,i}, t_i\right)$ is the propagated state vector from $\mathbf{p}_i$ to the next epoch t_{i+1}. The constraints imposed on the initial and final nodes in Eqs. (26) and (28) are defined as follows:

$$g_0\left(\mathbf{p}_1\right) = \mathbf{x}_\mathrm{GEO} - \mathbf{x}_1 \tag{30}$$

$$g_f\left(\mathbf{p}_n\right) = \mathbf{x}_{\mathrm{SE-CR3BP},\tau_\mathrm{f}\mathrm{P}_\mathrm{p.o}} - \mathbf{x}_n \tag{31}$$

where $\mathbf{x}_\mathrm{GEO}$ is the initial state vector of the un-propelled shared-transfer phase and $\mathbf{x}_{\mathrm{SE-CR3BP},\tau_\mathrm{f}\mathrm{P}_\mathrm{p.o}}$ is a state vector pertaining to the targeted halo orbit at the insertion point.

In order to solve the problem in Eqs. (26)-(29), the same two-step approach as the traditional multiple shooting differential corrector [24] is applied, where, in the first step, the continuity constraints (Eq. (27)) are satisfied by performing a ΔV at each node, and the second step then adjusts the positions and the epochs at each node along the trajectory in order to minimise the total ΔV. However, in the multiple shooter implemented in this section, the first step is slightly modified such that not only the velocity but also the sail attitude is adjusted at each node. Therefore, it results in a solar-sail trajectory with a different, but constant, sail attitude along each of the $n-1$ segments of the discretised trajectory.

2. Sail attitude control and weights optimisation

In the first level of the multiple shooter, the required change in velocity and sail attitude at each node is computed by means of the extended state transition matrix, $\Phi(t_f, t_0)$, which provides the linearised correction in the final state, denoted $\Delta\mathbf{x}_f = \begin{bmatrix}\mathbf{r}_f & \mathbf{v}_f\end{bmatrix}^T$, due to a change in the initial state vector $\Delta\mathbf{x}_0 = [\mathbf{r}_0 \quad \mathbf{v}_0]^T$ and a change in the parameters $\Delta\alpha_{s,0}$ and $\Delta\delta_{s,0}$. Mathematically, it is described as follows:

$$\Delta\mathbf{x}_f = \Phi(t_f, t_0)\begin{bmatrix}\Delta\mathbf{x}_0 & \Delta\alpha_{s,0} & \Delta\delta_{s,0}\end{bmatrix}^T \tag{32}$$

where $\Phi(t_f, t_0) = \begin{bmatrix}\frac{\partial\mathbf{x}}{\partial\mathbf{x}_0} & \frac{\partial\mathbf{x}}{\partial\alpha_{s,0}} & \frac{\partial\mathbf{x}}{\partial\delta_{s,0}}\end{bmatrix}$ is a 6×8 matrix that is obtained by numerically integrating the differential equations of the extended state transition matrix, according to [51].

Although the under-determined linear system in Eq. (32) can be easily solved by finding a least-squares solution, similar to what is done in the second step of the multiple shooter, in this paper, a matrix W that assigns different weights to $\Delta\mathbf{v}_0$, $\Delta\alpha_{s,0}$ and $\Delta\delta_{s,0}$ is introduced, such that the sail attitude angles are varied more intensively than the velocity, which ultimately yields smaller velocity discontinuities at the nodes. Therefore, considering that $\Delta\mathbf{r}_0 = 0$ and $\Delta\mathbf{v}_f$ is unconstrained, the solution of Eq. (32) is given by:

$$\begin{bmatrix}\Delta\mathbf{v}_0 \\ \Delta\alpha_{s,0} \\ \Delta\delta_{s,0}\end{bmatrix} = W\Phi_{R:}^T\left(\Phi_{R:}W\Phi_{R:}^T\right)^{-1}\left(-\Delta\mathbf{r}_f^T\right) \tag{33}$$

where $\Phi_{R:} = \begin{bmatrix}\frac{\partial\mathbf{r}}{\partial\mathbf{v}_0} & \frac{\partial\mathbf{r}}{\partial\alpha_{s,0}} & \frac{\partial\mathbf{r}}{\partial\delta_{s,0}}\end{bmatrix}$ and the weight matrix W is a diagonal matrix, with the velocity terms equal to one and the sail terms equal to W_α and W_δ. Note that, since the state transition matrix is propagated with linearised equations, the algorithm must be iterated until convergence, *i.e.*, until the deviation in position is within a specified tolerance $\Delta\mathbf{r}_f \leq \varepsilon_R$.

For each node and iteration, the best values for the weights W_α and W_δ are determined using the differential evolution optimisation algorithm that is implemented in the Python library 'SciPy'[‡‡‡], with the required change in velocity at the initial node of the segment $\Delta\mathbf{v}_0$ as the objective function to be minimised. The maximum upper bound of the search space for W_α and W_δ has been set to $5{\cdot}10^6$. The algorithm ensures that the rate of deflection of the sail angles does not surpass a sail maximum deflection of 24° per day [18] by limiting $\Delta\alpha_{s,0}$ and $\Delta\delta_{s,0}$ and decreasing the upper bound of the search space accordingly.

[‡‡‡]SciPy.org – Optimization. URL `https://docs.scipy.org/doc/scipy/reference/tutorial/optimize.html` (Access date 2019-12-07)

3. Feasible transfer trajectory in the CR3BP

Since the initial guess provided by the approach in Sec. VII.B presents a rather large discontinuity to correct, the reference trajectory is extended with a short trajectory arc along the sub$-L_1$ halo orbit (of length $\sim \frac{\pi}{13}$) in order to facilitate convergence of the multiple shooter. Furthermore, through trial and error, 145 nodes were selected, which are not equally distributed in time, but are focused around areas of faster dynamics and the linkage of the two segments.

Figure 24 shows the resulting transfer trajectory in the SE CR3BP, together with the initial guess used for the multiple shooter (red-dashed line). It is possible to see how the solar-sail spacecraft still travels together with Euclid for $\sim t_{\text{euclid}} = 155.9$ days, along the reference trajectory, but then quickly diverts away from both Euclid's trajectory and the initial guess. The converged trajectory flies ahead of Earth at a much further distance and intersects with the targeted halo orbit at a slightly later point. The discontinuities across the nodes are limited to 10^{-12} in position and $5 \cdot 10^{-5}$ in velocity, which correspond to a deviation of ~ 0.15 m ~ 1.5 m/s. At the initial and final nodes, the tolerances are slightly larger due to the boundary constraints: 10^{-4} in position (~15 000 km) and $6.5 \cdot 10^{-5}$ in velocity (~ 2 m/s). However, a second continuation scheme will be applied to the resulting trajectory in the ER3BP in order to reduce these discontinuities. As a last remark, the TOF of the resulting trajectory is within an error of ~ 8 min with respect to the optimal TOF found in Sec. VII.B.2.

Figure 25 provides the profile of the solar-sail attitude along the transfer trajectory, in terms of the cone angle α_s and the clock angle δ_s. Note that, during the first phase of the transfer, the solar sail is yet to be deployed, hence $\alpha_s = \frac{\pi}{2}$. There is an additional phase of the transfer, approximately from the 230th day until the 280th, when there is again

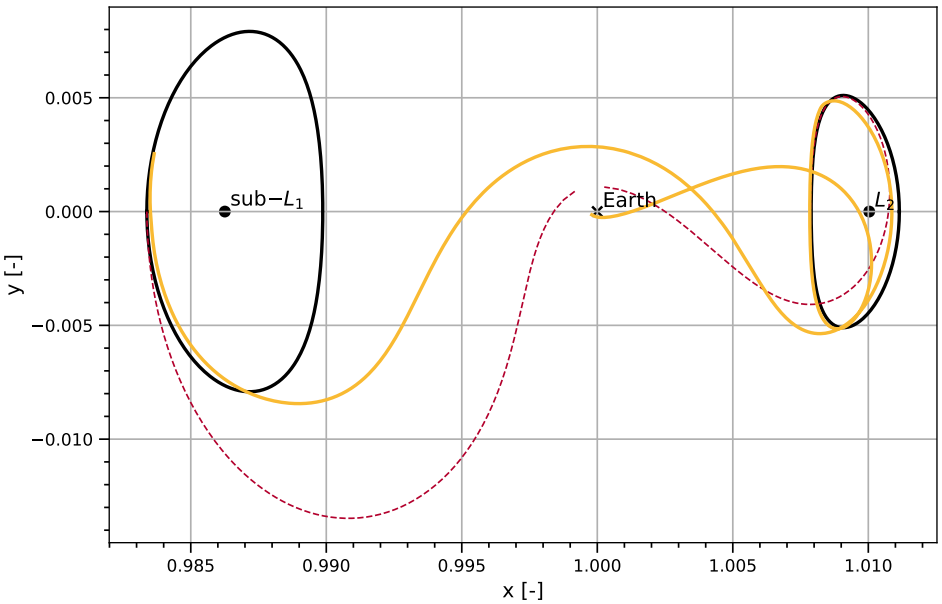

Fig. 24 Feasible transfer trajectory in the SE CR3BP. The dashed red line indicates the near-feasible transfer trajectory that has been used as initial guess in the multiple shooting differential corrector.

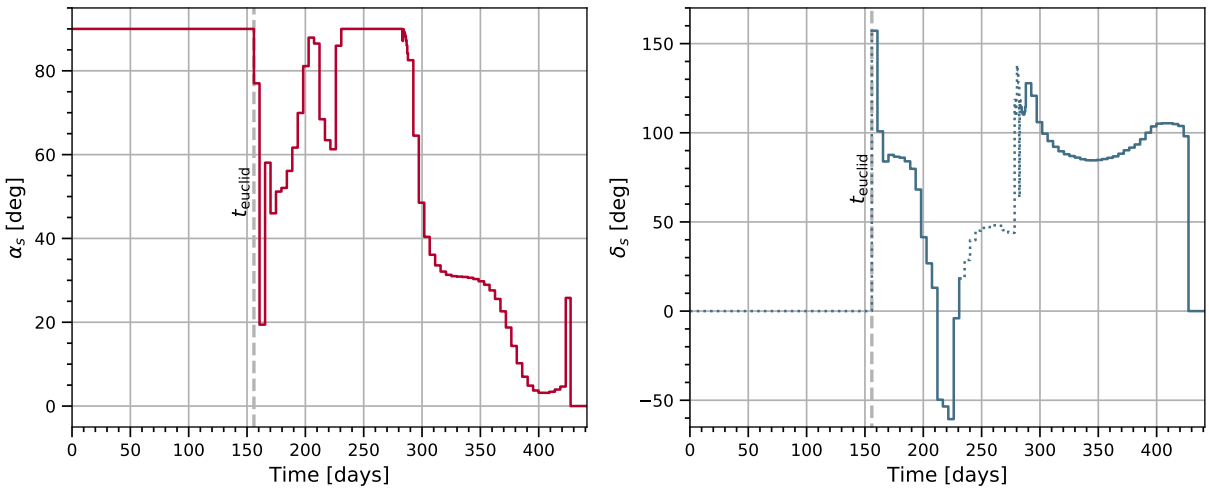

Fig. 25 Attitude of the solar sail, in terms of cone angle α_s and clock angle δ_s, along the transfer trajectory in the SE CR3BP.

no solar-sail acceleration $\left(\alpha_s = \frac{\pi}{2}\right)$ and thus the value of the clock angle δ_s is arbitrary. Although the attitude profile obtained is not perfectly smooth, all the required attitude changes throughout the flight satisfy the imposed maximum rate of change of 24° per day. Future work may consider implementing a non-constant continuous control law.

D. Transfer Trajectory to the Solar-Sail Halo Orbit around the Sun-Earth sub$-L_1$ point

With a feasible trajectory with a given TOF found in Sec. VII.C, a continuation scheme in eccentricity e is applied to obtain the transfer trajectory in the ER3BP.

1. Feasible transfer trajectory in the ER3BP

Because the equations of motion in the ER3BP are non-autonomous, it is essential to properly define the epoch at each of the nodes in the reference trajectory. To this aim, the reference epoch is set equal to the initial epoch of the targeted halo orbit. This orbit has a period equal to 4π, such that the true anomaly at the last and initial nodes of the transfer trajectory for $e = 0$ are defined as $f_n = 4\pi k + t_{\text{insertion}}$ and $f_1 = 4\pi k + t_{\text{insertion}} - T_{\text{f}}$, respectively, where $t_{\text{insertion}}$ indicates the propagation time from the initial conditions of the orbit, $\mathbf{X}_{\text{SE-ER3BP},0}$, until the insertion point of the solar-sail spacecraft. Note that $t_{\text{insertion}}$ is not equal to $\tau_f P_{\text{p.o}}$ since the end conditions of the transfer have been taken slightly later from the 'optimal' insertion point during the generation of a feasible trajectory with the multiple shooter.

Starting with the transfer trajectory in the CR3BP, and increasing e by a suitably small value ($\sim 10^{-4}$), a new transfer trajectory in the ER3BP is found by consecutively updating the decision vector $\mathbf{P}_i = \begin{bmatrix}\mathbf{X}_i & \alpha_{s,i} & \delta_{s,i} & f_i\end{bmatrix}^T$ with the multiple shooting differential corrector of Sec. VII.C until reaching Earth's eccentricity, *i.e.*, $e = 0.0167$. Note that, in this section, the constraint on the fixed TOF is discarded (Eq. (29)), and the constraints imposed on the initial

and final nodes in Eqs. (26) and (28) are re-defined as follows:

$$g_0\left(\mathbf{P}_1\right) = \mathbf{x}_1 - \mathbf{X}_1 \tag{34}$$

$$g_f\left(\mathbf{P}_n\right) = \mathbf{X}_{\mathrm{SE-ER3BP,f_n,e}} - \mathbf{X}_n \tag{35}$$

where $\mathbf{x}_1$ indicates the initial state vector of the transfer trajectory in the CR3BP and $\mathbf{X}_{\mathrm{SE-ER3BP,f_n,e}}$ is a state vector pertaining to the targeted halo orbit at true anomaly f_n and eccentricity e. Equation (34) states that the initial state vector of the transfer trajectory in the ER3BP, $\mathbf{X}_1$, is set equal to the initial state vector of the transfer trajectory in the CR3BP, obtained in Sec. VII.B. Eq. 35 then states that the final state vector of the transfer trajectory in the ER3BP, $\mathbf{X}_n$, is set equal to the state vector of the sub$-L_1$ halo orbit at true anomaly f_n, which is obtained by propagating the initial conditions of the orbit, $\mathbf{X}_{\mathrm{SE-ER3BP},0}$, from $f_0 = 4\pi k$ to f_n. In addition, the weights of the sail terms, W_α and W_δ, are set equal to one because the reference trajectory is already very close to the final solution in the ER3BP. Therefore, the sail attitude profile during the transfer trajectory in the ER3BP is similar to the one shown in Fig. 25.

Figure 26 shows the resulting transfer trajectory and halo orbit in the SE ER3BP. The discontinuities across the nodes along the trajectory are limited to 10^{-12} in position and $5 \cdot 10^{-5}$ in velocity, which correspond to a deviation of $\sim$ 0.15 m and $\sim$ 1.5 m/s. At the initial and final nodes, a second continuation scheme has been applied to reduce the discontinuities in position and velocity down to 10^{-5} ($\sim$1 500 km) and $5.0 \cdot 10^{-5}$ ($\sim$ 1.5 m/s), respectively, which are assumed acceptable for the scale of the transfer designed.

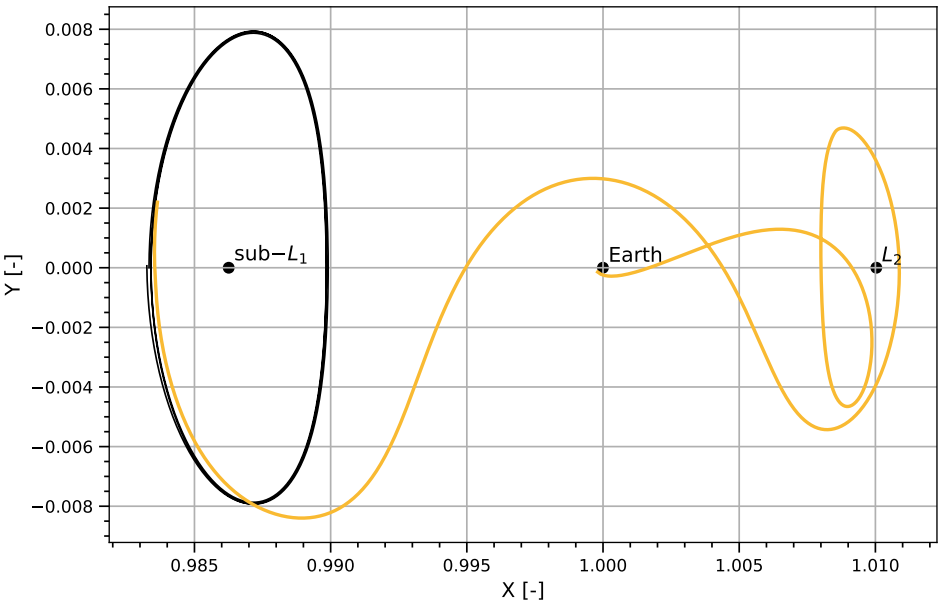

Fig. 26 Feasible transfer trajectory in the SE ER3BP. Note that the indicated locations of the sub$-L_1$ and L_2 points are instantaneous and only hold valid when the distance between Sun and the Earth is 1 au.

VIII. Conclusions

The aim of this paper was to design a space mission that places a telescope in-orbit in order to detect and provide warning for near-Earth objects (NEOs) on a collision course with Earth. Two mission candidates were envisioned for this purpose: the first mission candidate consists of a solar-sail halo orbit about the artificial equilibrium point sub-L_1 of the Sun-Earth (SE) system, and the second one consists of three vertical Lyapunov orbits about the libration points L_3, L_4 and L_5 of the Sun-Venus (SV) system. The performance of a space-based telescope used in each of these mission candidates was determined by means of a space-based survey simulation tool, that determines whether the object is observable by the visible (VIS) and/or thermal infrared (TIR) space-based telescope before impact, for four different synthetic populations of impactors in the range ∼22–140 m in diameter.

For surveying NEOs down to 20 m in diameter, the simulations of space-based surveys clearly show that the SE mission candidate performs better than the SV one in terms of detection rates, for both wavebands considered. The results indicate that the space-based telescope at the SE sub$-L_1$ point is able to observe between ∼40% and ∼50% of the impactors, depending on the waveband, while the space-based telescopes at the SV L_3, L_4 and L_5 points are only observing ∼3–17% of the NEOs during the one year of observation before impact. Regarding the waveband for the space-based telescope, although the results differ between the two mission candidates, it is concluded that surveying at IR wavelengths is more effective due to the longer warning times obtained, which is key for providing warning for impacting NEOs. The results indicate that the TIR space-based telescope at the SE sub$-L_1$ point is able to detect ∼40% of all NEOs with a warning time of at least one day, which is significantly higher than other estimates found in literature. When surveying at VIS wavelengths from this location, although the detection rate is approximately ∼10% larger than the TIR case, the obtained warning times are generally shorter.

When combined with ground observations by ESA's Flyeye telescope, the survey system is estimated to detect approximately ∼61% and ∼63% of all impacting NEOs by means of the TIR and VIS space-based telescopes, respectively. Although the VIS space-based telescope still provides slightly larger detection rates, the difference between the VIS and TIR space-based survey results has been reduced from 10% to only 2%, which implies that surveying at IR wavelengths from the SE sub$-L_1$ point better complements existing ground-based surveys. When considering multiple space-based telescopes instead of only one, it is concluded that the best NEO survey system consists of two TIR space-based telescopes at the SE sub$-L_1$ point, combined with ground-based surveys, which is able to efficiently detect and provide warning for almost ∼72% of all NEOs at least one day before impact. Lastly, a feasible transfer trajectory from Earth's vicinity to the operational orbit of the space-based telescope was designed in the elliptic restricted three-body problem (ER3BP), which assumes a ride-share launch with ESA's Euclid spacecraft and takes 427.25 days.

Appendix

A. Software Tuning

1. Selection of tuning parameters

The space-based survey model contains many parameters that are typically unknown, and thus they need to be assumed. As a result of these assumptions, large uncertainties are introduced, which may affect the obtained results. Another source of uncertainty is derived from the models used to develop the software, *e.g.*, the zodiacal model for the background noise, due to the many assumptions and considerations during the implementation of the model. For these reasons, some parameters of the space-based survey model need to be tuned in order to ensure that the obtained results are robust.

The first parameter to analyse is the visual albedo of the NEO p_v, which is often unknown, and thus needs to be assumed, resulting in very large uncertainties in the estimation of the size of a NEO (see Eq. (15)). For the following test simulations, the albedo of the NEO will be tuned using three different values: 0.05, 0.14 and 0.25. The second parameter to analyse is the thermal model used to compute the infrared brightness of the NEO. As previously mentioned in Sec. V.D.2, two different thermal models are considered and tested in the following simulations: the STM and the NEATM. The third and last parameter to analyse is the model implementations of the background's noise in both VIS and TIR wavebands, which have a direct impact on the computed SNR.

In order to determine which tuning parameters have a larger impact on the results of the space-based surveys, several test simulations have been performed. As the input NEO population, a sample population of 500 random impacting NEOs from population #1 (see Sec. V.C) has been chosen, and the observation window of the simulation is set to one year before impact.

2. Discussion of test simulation results

The first parameters to tune are the albedo of the NEO and the thermal model for the infrared brightness. Table 7 presents the obtained detection rates for each space-based survey system considered, using three different values of the albedo p_v: 0.05, 0.14 and 0.25 and the two thermal models considered for the infrared space-based telescope.

First, it is possible to observe that the visual albedo does not have a significant impact on the results of the VIS waveband, as similar detection rates are obtained at each of the two orbit locations considered. However, it does have a major impact on the TIR results, as a smaller p_v corresponds to a larger diameter and surface temperature of the object, and it thus emits more thermal radiation. The reason why the visual albedo does not have a significant impact on the VIS results is because, for a given H, the visual albedo does not significantly influence the optical brightness of the object as it mainly depends on H (see Eq. (19)) and only has a minimum dependence on p_v through the opposition effect. Moreover, while a smaller p_v derives a larger size, thus increasing the reflective surface of the object, it also

Table 7 Detection rates for different orbit locations, wavebands of the space-based telescope and visual albedos of the objects, using a sample population of 500 impacting NEOs and one year of observation window before impact.

Band	Location	$p_v = 0.05$	$p_v = 0.14$	$p_v = 0.25$
VIS	SE sub$-L_1$	90.0%	90.4%	90.4%
	SV $L_{3,4,5}$	2.0%	2.8%	3.0%
TIR/STM	SE sub$-L_1$	64.2%	58.2%	56.2%
	SV $L_{3,4,5}$	60.4%	26.6%	10.8%
TIR/NEATM	SE sub$-L_1$	63.2%	57.2%	55.0%
	SV $L_{3,4,5}$	56.6%	24.2%	9.4%

means a smaller reflectivity of the object, and so the amount of reflected sunlight remains independent of p_v. For these reasons, the VIS space-based surveys in this paper only consider a default albedo of 0.14.

Regarding the thermal model for the infrared brightness, it is possible to observe that similar results are obtained using the two models, which is to be expected as the waveband of the TIR space-based telescope lies within the longer-wavelength part of the IR spectrum, where the simpler STM is reliable and closer to the more accurate NEATM. Nonetheless, slight worse results are obtained using the NEATM. Furthermore, the warning times obtained using the 'worst-case' NEATM are considerably shorter than when using the STM. Therefore, the NEATM is chosen in the TIR space-based surveys in this paper in order to consider the worst-case scenario.

The last parameter to analyse is the uncertainty in the total background noise due to the inherent assumptions in the models and the neglected light contributions, which impacts the computed SNR of the object. To this aim, the uncertainty in the SNR has been estimated by quantifying the relative contribution of each of the light sources to the total noise, using the more accurate background noise model developed by IPAC at Caltech[§§§]. This on-line tool provides optical-to-infrared estimates of the (median) zodiacal, interstellar, stellar and cosmic background noise for observations from the SE L_2 region. As these estimates for the night brightness depend on the date, wavelength and pointing direction, several different scenarios have been computed. At VIS wavelengths, the uncertainty has been estimated to be in the range of 10–80%, which is to be expected due to the neglected starlight. At IR wavelengths, the uncertainty is in the smaller range of 1–20%, mainly due to the neglected Earth-trailing blob in the zodiacal dust model.

Table 8 presents the obtained detection rates for each space-based survey system considered, using a default albedo of $p_v = 0.14$ and the NEATM for the IR space-based telescope. The uncertainty is considered by applying a multiplying factor to the computed background irradiance, B_e. It is possible to see that the detection rates do not change significantly with the increased background noise, especially for the SE case, for which the impactors get close

[§§§]Background Model. URL `https://irsa.ipac.caltech.edu/applications/BackgroundModel/` (Access date 2019-08-14)

Table 8 Detection rates for different orbit locations, wavebands of the space-based telescope and uncertainty multiplying factors on the background's irradiance, using a sample population of 500 impacting NEOs and one year of observation window before impact.

Band	Location	p_v	Factor × B_e					
			1.0	1.5	2.0	2.5	3.0	5.0
VIS	SE sub$-L_1$	0.14	90.4%	88.6%	88.6%	88.6%	88.6%	88.6%
	SV $L_{3,4,5}$	0.14	2.8%	2.6%	2.4%	2.2%	2.0%	1.4%
TIR/NEATM	SE sub$-L_1$	0.14	57.2%	–	55.0%	54.8%	54.6%	–
	SV $L_{3,4,5}$	0.14	24.2%	–	14.4%	12.0%	7.6%	–

enough to the observer that they are much brighter than the stellar background. For the SV case, the detection rates do vary slightly more because the time intervals when the objects are close and bright enough are shorter, and thus the SNR condition is more limiting. Regardless of the uncertainty in the SNR, the obtained detection rates can be assumed to be accurate enough due to the (slight) constraining detection threshold that is implemented in the space-based survey model, previous to the computation of the SNR, in order to take into account the neglected light sources.

References

[1] Stokes, G. H., Barbee, B. W., Bottke, W. F., Buie, M. W., Chesley, S. R., Chodas, P. W., Evans, J. B., Gold, R. E., Grav, T., Harris, A. W., Jedicke, R., Mainzer, A. K., Mathias, D. L., Spahr, T. B., and Yeomans, D. K., "Update to Determine the Feasibility of Enhancing the Search and Characterization of NEOs," Report of the near-earth object science definition team (2017), National Aeronautics and Space Administration, 2017. URL `https://cneos.jpl.nasa.gov/doc/SDT_report_2017.html`, access date 2019-03-14.

[2] Ramirez Torralba, O., Jehn, R., Koschny, D., Frühauf, M., Jehn, L., and Praus, A., "Simulation of Sky Surveys with the Flyeye telescope," *Proc. 1st NEO and Debris Detection Conference (Darmstadt, Germany, 22-24 January 2019)*, ESA Space Safety Programme Office, 2019. URL `https://conference.sdo.esoc.esa.int/proceedings/neosst1/paper/2/NEOSST1-paper2.pdf`.

[3] Farnocchia, D., Bernardi, F., and Valsecchi, G. B., "Efficiency of a wide-area survey in achieving short-and long-term warning for small impactors," *Icarus*, Vol. 219, No. 1, 2012, pp. 41–47.

[4] Mainzer, A., Bauer, J., Grav, T., Masiero, J., Cutri, R., Dailey, J., Eisenhardt, P., McMillan, R., Wright, E., Walker, R., et al., "Preliminary results from NEOWISE: an enhancement to the wide-field infrared survey explorer for solar system science," *The Astrophysical Journal*, Vol. 731, No. 1, 2011, p. 53.

[5] Mainzer, A., Grav, T., Bauer, J., Conrow, T., Cutri, R., Dailey, J., Fowler, J., Giorgini, J., Jarrett, T., Masiero, J., et al., "Survey simulations of a new near-Earth asteroid detection system," *The Astronomical Journal*, Vol. 149, No. 5, 2015, p. 172.

[6] Milam, S., Hammel, H., Bauer, J. M., Brozovic, M., Grav, T., Holler, B. J., Mainzer, A. K., Reddy, V., Schwamb, M. E., Spahr, T. B., et al., "Emerging Capabilities for Detection and Characterization of Near-Earth Objects (NEOs)," *Bulletin of the American Astronomical Society*, 2019. Vol.51, No.3.

[7] Shustov, B., Shugarov, A., Naroenkov, S., and Kovalenko, I., "System of observation of day-time asteroids (SODA)," *Proc. 1st NEO and Debris Detection Conference (Darmstadt, Germany, 22-24 January 2019)*, ESA Space Safety Programme Office, 2019. URL `https://conference.sdo.esoc.esa.int/proceedings/neosst1/paper/439/NEOSST1-paper439.pdf`.

[8] Tsuda, Y., Mori, O., Funase, R., Sawada, H., Yamamoto, T., Saiki, T., Endo, T., Yonekura, K., Hoshino, H., and Kawaguchi, J., "Achievement of IKAROSJapanese deep space solar sail demonstration mission," *Acta Astronautica*, Vol. 82, No. 2, 2013, pp. 183–188.

[9] Johnson, L., Whorton, M., Heaton, A., Pinson, R., Laue, G., and Adams, C., "NanoSail-D: A solar sail demonstration mission," *Acta Astronautica*, Vol. 68, No. 5-6, 2011, pp. 571–575.

[10] Müller, M., "Surface properties of asteroids from mid-infrared observations and thermophysical modeling," *arXiv preprint arXiv:1208.3993*, 2012.

[11] Mainzer, A., Grav, T., Masiero, J., Bauer, J., Wright, E., Cutri, R., McMillan, R., Cohen, M., Ressler, M., and Eisenhardt, P., "Thermal model calibration for minor planets observed with wide-field infrared survey explorer/NEOWISE," *The Astrophysical Journal*, Vol. 736, No. 2, 2011, p. 100.

[12] Szebehely, V., "Theory of Orbits, the Restricted Problem of Three Bodies," , 1967.

[13] McInnes, C. R., *Solar sailing: technology, dynamics and mission applications*, Springer Science & Business Media, 2013.

[14] Macdonald, M., and McInnes, C., "Solar sail science mission applications and advancement," *Advances in Space Research*, Vol. 48, No. 11, 2011, pp. 1702–1716.

[15] Heiligers, J., Diedrich, B., Derbes, W., and McInnes, C. R., "Sunjammer: preliminary end-to-end mission design," *AIAA/AAS Astrodynamics Specialist Conference*, 2014, p. 4127.

[16] McInnes, C. R., *Solar sailing: Technology, Dynamics and Mission Applications (Springer-Praxis Books)*, Springer-Verlag, Berlin, 2004.

[17] Dachwald, B., Mengali, G., Quarta, A. A., and Macdonald, M., "Parametric model and optimal control of solar sails with optical degradation," *Journal of Guidance, Control, and Dynamics*, Vol. 29, No. 5, 2006, pp. 1170–1178.

[18] Biggs, J. D., McInnes, C. R., and Waters, T., "Control of solar sail periodic orbits in the elliptic three-body problem," *Journal of Guidance, Control, and Dynamics*, Vol. 32, No. 1, 2009, pp. 318–320.

[19] Howell, K., and Pernicka, H., "Sun-Earth libration point trajectories that avoid the solar exclusion zone," *Journal of the Astronautical Sciences*, Vol. 38, 1990, pp. 269–288.

[20] Baoyin, H., and McInnes, C. R., "Solar sail halo orbits at the Sun–Earth artificial L1 point," *Celestial Mechanics and Dynamical Astronomy*, Vol. 94, No. 2, 2006, pp. 155–171.

[21] Waters, T. J., and McInnes, C. R., "Periodic orbits above the ecliptic in the solar-sail restricted three-body problem," *Journal of Guidance, Control, and Dynamics*, Vol. 30, No. 3, 2007, pp. 687–693.

[22] Howell, K. C., "Three-dimensional, periodic, 'halo' orbits," *Celestial mechanics*, Vol. 32, No. 1, 1984, pp. 53–71.

[23] Heiligers, J., Macdonald, M., and Parker, J. S., "Extension of Earth-Moon libration point orbits with solar sail propulsion," *Astrophysics and Space Science*, Vol. 361, No. 7, 2016, p. 241.

[24] Parker, J. S., and Anderson, R. L., *Low-energy lunar trajectory design*, Vol. 12, John Wiley & Sons, 2014.

[25] Gómez, G., and Mondelo, J. M., "The dynamics around the collinear equilibrium points of the RTBP," *Physica D: Nonlinear Phenomena*, Vol. 157, No. 4, 2001, pp. 283–321.

[26] Wakker, K., *Fundamentals of astrodynamics*, TU Delft Library, 2015.

[27] Richardson, D. L., "Analytic construction of periodic orbits about the collinear points," *Celestial mechanics*, Vol. 22, No. 3, 1980, pp. 241–253.

[28] Richardson, D. L., "Periodic and Quasi Periodic Halo Orbits in the Earth-Sun/Earth-Moon Systems," 2010.

[29] Belton, M. J., Belton, M. J., Morgan, T. H., Samarasinha, N. H., and Yeomans, D. K., *Mitigation of hazardous comets and asteroids*, Cambridge University Press, 2004.

[30] Granvik, M., Morbidelli, A., Jedicke, R., Bolin, B., Bottke, W. F., Beshore, E., Vokrouhlický, D., Nesvorný, D., and Michel, P., "Debiased orbit and absolute-magnitude distributions for near-Earth objects," *Icarus*, Vol. 312, 2018, pp. 181 – 207. https://doi.org/https://doi.org/10.1016/j.icarus.2018.04.018, URL http://www.sciencedirect.com/science/article/pii/S0019103517307017.

[31] Harris, A. W., "A thermal model for near-Earth asteroids," *Icarus*, Vol. 131, No. 2, 1998, pp. 291–301.

[32] Chesley, S. R., and Spahr, T. B., "Earth impactors: orbital characteristics and warning times," *Mitigation of Hazardous Comets and Asteroids*, Vol. 22, 2004.

[33] Koschny, D., and Igenbergs, E., "Near-Earth Objects for engineers and physicists. Lecture notes, TU Munich." , 2015. URL: http://neo.koschny.eu. Access date 2019-03-11.

[34] APL, "Analysis of Alternatives for Near-Earth Object Detection, Tracking and Characterization," Tech. rep., Johns Hopkins University Applied Physics Laboratory, March 2018. URL https://www.nasa.gov/sites/default/files/atoms/files/aoa_neo_report_031218_final.pdf, access date 2019-03-29.

[35] Gelhaus, J., Hahn, G., and Müller, S., "Final Report: Near Earth Object Population Observation Program," Tech. Rep. SGNEOP-FR, Technische Universität Braunschweig (TUBS), Institute of Aerospace Systems (ILR), Brauschweig, Germany, March

2015. URL http://neo.ssa.esa.int/c/document_library/get_file?uuid=aa4f5313-6a56-473a-adcd-6d5fd05d1daf&groupId=10157, Project title: Synthetic Generation of a NEO Population. Revision: 1.4.

[36] Belskaya, I., and Shevchenko, V., "Opposition effect of asteroids," *Icarus*, Vol. 147, No. 1, 2000, pp. 94–105.

[37] Shevchenko, V., "Analysis of the asteroid phase dependences of brightness," *Lunar and Planetary Science Conference*, Vol. 27, 1996.

[38] Johnson, H., and Morgan, W., "Fundamental stellar photometry for standards of spectral type on the revised system of the Yerkes spectral atlas," *The Astrophysical Journal*, Vol. 117, 1953, p. 313.

[39] Cousins, A., "VRI standards in the E regions," *Memoirs of the Royal Astronomical Society*, Vol. 81, 1976, p. 25.

[40] Lebofsky, L. A., Sykes, M. V., Tedesco, E. F., Veeder, G. J., Matson, D. L., Brown, R. H., Gradie, J. C., Feierberg, M. A., and Rudy, R. J., "A refined 'standard' thermal model for asteroids based on observations of 1 Ceres and 2 Pallas," *Icarus*, Vol. 68, No. 2, 1986, pp. 239–251.

[41] Wolters, S. D., Green, S. F., McBride, N., and Davies, J. K., "Thermal infrared and optical observations of four near-Earth asteroids," *Icarus*, Vol. 193, No. 2, 2008, pp. 535–552.

[42] Leinert, C., Bowyer, S., Haikala, L., Hanner, M., Hauser, M., Levasseur-Regourd, A.-C., Mann, I., Mattila, K., Reach, W., Schlosser, W., et al., "The 1997 reference of diffuse night sky brightness," *Astronomy and Astrophysics Supplement Series*, Vol. 127, No. 1, 1998, pp. 1–99.

[43] Daniels, G. M., "A night sky model for satellite search systems," *Optical Engineering*, Vol. 16, No. 1, 1977, p. 160166.

[44] Kelsall, T., Weiland, J., Franz, B., Reach, W., Arendt, R., Dwek, E., Freudenreich, H., Hauser, M., Moseley, S., Odegard, N., et al., "The COBE diffuse infrared background experiment search for the cosmic infrared background. II. Model of the interplanetary dust cloud," *The Astrophysical Journal*, Vol. 508, No. 1, 1998, p. 44.

[45] Milani, A., Gronchi, G. F., Knežević, Z., Sansaturio, M., Arratia, O., Denneau, L., Grav, T., Heasley, J., Jedicke, R., and Kubica, J., "Unbiased orbit determination for the next generation asteroid/comet surveys," *Proceedings of the International Astronomical Union*, Vol. 1, No. S229, 2005, pp. 367–380.

[46] Farnocchia, D., Chesley, S., and Micheli, M., "Systematic ranging and late warning asteroid impacts," *Icarus*, Vol. 258, 2015, pp. 18–27.

[47] Cibin, L., Chiarini, M., Gregori, P., Bernardi, F., Ragazzoni, R., Sessler, G., and Kugel, U., "The Fly-Eye Telescope, Development and First Factory Tests Results." *Proc. 1st NEO and Debris Detection Conference (Darmstadt, Germany, 22-24 January 2019)*, ESA Space Safety Programme Office, 2019. URL https://conference.sdo.esoc.esa.int/proceedings/neosst1/paper/481/NEOSST1-paper481.pdf.

[48] Renk, F., and Landgraf, M., "Euclid: ESA's dark energy 3-axis stabilized survey mission at the night-side Sun-Earth libration point," 2014.

[49] Topputo, F., Vasile, M., and Ercoli, A., "An approach to the design of low energy interplanetary transfers exploiting invariant manifolds of the restricted three-body problem," *14th AAS/AIAA Space Flight Mechanics Meeting*, Univelt, 2004, pp. 2229–2248.

[50] Fernández Mora, A., "Solar-sail invariant objects in the Sun-Earth system and transfers to the L5 region," Master's thesis, Delft University of Technology, Delft, The Netherlands, February 2019.

[51] McInnes, A. I. S., "Strategies for solar sail mission design in the circular restricted three-body problem," Master's thesis, School of Aeronautics and Astronautics, Purdue University, 2000.

3

Conclusions and Recommendations

3.1. Conclusions

The aim of this research was to design a space mission that places a telescope in-orbit in order to detect and provide warning for near-Earth objects (NEOs) on a collision course with Earth by determining the performance of both a visible (VIS) and thermal infrared (TIR) space-based telescope used in two different mission candidates, and performing a mission analysis in order to determine a feasible transfer trajectory to the most optimal operational orbit. A main research question and a set of research sub-questions were formulated in Section 1.4 in order to fulfil this research aim. Based on the results and work presented throughout the draft journal article in Chapter 2, this section starts by answering all the sub-questions, which leads to a final conclusion that answers the main research question.

1. *How do the two orbit locations perform and compare in terms of NEO detection rate and warning time?*
   Based on a NEO population that is distributed in size in the range of 20–140 m, the results of the sky surveys clearly show that the Sun-Earth (SE) mission candidate outperforms the Sun-Venus (SV) mission candidate for both wavebands considered. Since the NEO population consists of Earth impactors, the space-based telescope at the SE sub$-L_1$ point acts as a 24/7 security camera, that is able to capture up to ~ 50% of all NEOs before impact. Instead, the space-based telescope at the SV L_3, L_4 and L_5 points is able to capture only up to ~17% in the best-case scenario. The performance of this orbit candidate highly depends on the likelihood of the NEO passing through the field of regard (FOR) on its collision course with Earth. Consequently, the detection rates are much smaller for the SV case than for the SE case but may improve if the observation window is longer. In terms of warning time, it is difficult to draw a solid conclusion since the obtained detection rates between the two mission candidates are so different.

Nonetheless, when considering larger and brighter objects than $H = 22$ (which corresponds to ~140 m), similar detection rates are obtained for both orbit locations, with values up to ~50% and ~55% of observed NEOs for the SV and the SE mission candidates, respectively. In this case, both orbit locations seem to perform similarly in terms of warning time.

2. *Which wavelength band provides the longest warning time for impacting NEOs and/or largest detection rates?*

   For observing Earth impacting NEOs in the size range of 20–140 m, although the VIS and TIR results differ quite significantly between the two mission candidates, it is concluded that surveying at IR wavelengths is more effective in terms of both detection rate and warning time, for the following reasons. First, a considerable improvement of the SV results has been observed between the VIS and the TIR cases; while the VIS space-based telescope is only able to detect ~3% of the NEOs, the TIR space-based telescope can observe up to ~17%, improving thus the detection rate of this mission candidate by 14%. Second, for the SE orbit candidate, it is concluded that many observations by the VIS space-based telescope are obtained at large solar elongations, where the TIR survey cannot reach, due to a FOR that is closer to Earth. Therefore, although the largest detection rate is obtained by a VIS space-based telescope at the SE orbit candidate, with a value of ~50% of observed NEOs, many of these extra detections are obtained with very short warning times. Instead, the TIR space-based telescope at this same location observes up to ~40% of all NEOs with warning times of at least one day. Last but not least, surveying at IR wavelengths at both orbit locations generally provides longer warning times. For instance, a TIR space-based telescope at the SE orbit location detects almost 15% of the objects with a warning time of at least one month before impact, while the VIS space-based telescope can only detect less than 5%.

   However, when considering larger and brighter objects than $H = 22$ (≥140 m), the SV mission candidate obtains slightly larger detection rates at VIS wavelengths than at TIR wavelengths and similar warning times.

3. *How does the combination of space- and ground-based survey systems perform in terms of NEO detection rate and warning time?*

   When combining all observations from ground- and space-based surveys, the obtained detection rates are doubled. For the chosen SE orbit candidate, the detection rate improves from ~50% and ~40% at VIS and TIR wavelengths, respectively, to ~63% and ~61%. Note that, when using only a space-based telescope or combining it with the ground-based results, the difference in results between the two wavebands decreases from 10% to 2%, respectively. This indicates that surveying at IR wavelengths better complements ground-based surveys, even though the VIS space-based telescope obtains a slightly larger detection rate. The reason is that many of the extra detections by the VIS space-based telescope, that result in the additional +2% in the detection rate, are obtained at larger solar elongations, that cannot be reached with TIR surveys but can instead be obtained with ground-based surveys. In terms of warning time, the TIR space-based telescope still remains the better option.

   Therefore, it is possible to conclude that space-based surveys are necessary in order to not only de-

tect those impacting NEOs with a longer warning time before impact, but also to detect those that are missed by existing ground-based telescopes. Furthermore, it is concluded that the best way to detect as many Earth impactors as soon as possible is by combining a TIR space-based telescope at the SE sub$-L_1$ point with existing ground-based telescopes.

4. *How does the performance of the NEO survey system improve with multiple space-based telescopes?*
When considering two space-based telescopes at the SE sub$-L_1$ point instead of one, a major improvement in the detection rates is observed, as the results improve by 18% and 11% at VIS and TIR wavelengths, respectively. However, the addition of a third telescope does not bring the same improvement, as the results now improve only by 9% and 3% at VIS and TIR wavelengths, respectively, with respect to two space-based telescopes. Therefore, it is decided that the additional cost of a third telescope is not worth this slight increase in observed NEOs, especially since these extra detected NEOs have a very short warning time.

   The obtained results also show how the increase in performance with two space-based telescopes is significantly different for each waveband; although the detection rates of only one space-based telescope are fairly similar, two VIS space-based telescopes are able to detect up to 20% more of the Earth impactors than two TIR space-based telescopes. However, when combined with ground-based surveys, the difference between the VIS and TIR results is only 10%, which further strengthens the previous statement that TIR space-based surveys combine best with existing ground-based telescopes.

5. *What transfer scheme from Earth results in a feasible trajectory to the chosen operational orbit?*
In this research work, a ride-shared launch on ESA's Euclid mission to the SE L_2 point is assumed. Therefore, the transfer scheme from Earth's vicinity to the operational orbit of the space-based telescope is divided into two segments. First, an un-propelled shared-transfer phase, where the solar-sail spacecraft travels together with Euclid for some time, and a solar-sail propelled phase, where the solar-sail spacecraft finally deploys the solar sail and starts diverting away from Euclid's trajectory, towards the SE sub$-L_1$ region.

   Through the use of solar-sail propulsion, this transfer trajectory was optimised in terms of the time of flight (TOF) and infeasibility by means of a multi-objective optimisation algorithm. After several runs with different random seeds and a local refinement around the found optimum, the optimal near-feasible transfer trajectory with the smallest infeasibility was chosen, which yielded a suboptimal TOF of 427.25 days. Then, in order to find a feasible transfer trajectory, an innovative two-step multiple shooting differential corrector was implemented such that the sail attitude was varied more intensively, ultimately leading to smaller velocity discontinuities in the trajectory, while still ensuring the fly-ability of the solar sail. Using this multiple shooter algorithm, a feasible transfer trajectory in the SE CR3BP was successfully determined, which was then obtained in the SE ER3BP by applying a continuation scheme in eccentricity. The resulting transfer trajectory in the SE ER3BP also presents a suboptimal TOF of 427.25 days.

To summarise, the answer to the main research question,

What is the best location and what are the best characteristics for a space-based telescope with the aim of efficiently detecting and providing warning for NEOs that are going to impact Earth?

is as follows.

- For surveying Earth impacting NEOs down to 20 m in diameter, a TIR space-based telescope placed at the Sun-Earth solar-sail displaced L_1 point is concluded to be the best option, mainly due to the long warning times obtained. Moreover, a space-based telescope surveying at IR wavelengths is able to contribute more to existing ground-based NEO surveys, as it is able to detect those NEOs at small solar elongations, that are missed by ground telescopes, with enough warning time before impact. It is also concluded that the best NEO survey system consists of one or two TIR space-based telescopes at the SE sub$-L_1$ point, combined with ground-based surveys, which is able to efficiently detect and provide warning for almost ~72% of all NEOs.

3.2. RECOMMENDATIONS

During the development of the main research content, there were many tasks and/or new interesting ideas outside the scope of the thesis that were left unexplored, unfortunately, mainly due to time constraints. This section briefly describes each of these recommendations for future work, which are expected to improve and cover the weak points of this thesis, as well as provide new topic ideas for further research.

- *Implementation of a survey cadence*

  Two main assumptions have been introduced in the simulations of sky surveys due to the absence of a survey cadence: a NEO is assumed to be observed when it satisfies the detection conditions for which a tracklet can be built, and when the pointing direction of the space-based telescope is uniquely defined during the time interval of observation. However, in reality, any space-based astronomical observation follows a survey cadence that defines the sequence of observation times and scanning directions, the revisit times between images and so on, in order to ensure detection, follow-up and accurate orbit determination of the detected celestial objects. The implementation of a survey cadence is not trivial and requires a detailed analysis to optimise the number of observations. There are many ongoing projects around the NEOCam project to determine the optimum survey cadence for potentially hazardous asteroids (PHAs), such as (Grav et al., 2019). Ultimately, this task was considered to be outside the scope of the thesis, but could be an interesting idea for future work.

- *Addition of the starlight contribution to the total background noise*

  At VIS wavelengths, the two main contributions to the total background noise are the light sources due to zodiacal light and starlight. Due to the neglected starlight contribution in this work, the uncertainty in the computed background irradiance has been estimated to be in the range of 10–80% at VIS wavelengths. In order to take into account this neglected light source, a (slight) constraining detection

threshold has been implemented in the space-based survey model, previous to the computation of the Signal-to-Noise Ratio (SNR), that defines whether the NEO is detected or not. Although the test simulations show that the results are robust, as the detection rates do not change significantly when the background noise is increased due to the uncertainty in the sources, the results would certainly be more accurate and reliable if the starlight contribution were implemented at VIS wavelengths. Moreover, this would also help in the selection of the waveband of the space-based telescope, since the obtained detection rates by the VIS and TIR space-based telescopes were fairly similar.

- *Estimation of the improved performance for providing warning of impacting NEOs of solar-sail displaced libration point orbits (LPOs) over classical LPOs around the L_1 point*

  All proposed space-based surveys of NEOs found in literature conclude that the SE L_1 point is the best location for placing the space-based telescope. However, the use of solar sails in the Sun-Earth L_1 region in order to displace the AEP towards the Sun is expected to increase the warning time. Therefore, it would be interesting to run the simulations of sky surveys for a halo orbit around the classical L_1 point in order to estimate and quantify this improvement in the performance. Proposals like the SODA project, which aims at finding potential impactors, might consider the use of solar sails, obtaining thus longer warning times than the four hours estimated (Shustov et al., 2019).

- *Use of a different population of Earth impactors*

  This research work has used the population of synthetic Earth impactors derived by Ramirez Torralba et al. (2019), which was based on the most-recent NEO population model developed by Granvik et al. (2018). However, there is a second population of Earth impactors found in literature, the one derived by Chesley and Spahr (2004), which was based on the (old) NEO population model developed by Bottke et al. (2002). The main difference between the two populations of Earth impactors is that the one derived by Ramirez Torralba et al. (2019) is distributed in a range of absolute magnitude, and thus each orbit is associated to each NEO with a given size and reflectivity. However, since in this work it has been assumed that there was no correlation between the physical size and the orbital characteristics of the NEO population, the second population by Chesley and Spahr (2004) could also have been used. It would be interesting to see how the results change (or not) when using a different population.

- *Extension of the observation window for the simulations of sky surveys*

  The observation window for the simulations of sky surveys presented in this work was fixed to one (sidereal) year before impact. The reason why is that the orbits of the NEOs in the Earth impactor population were slightly modified, such that they would be impacting Earth within one year (Ramirez Torralba et al., 2019). Therefore, for statistically purposes, the observation window was also one year. However, the lifetime of a space-based survey mission like this is typically four to five years (*e.g.*, NEOCam (Milam et al., 2019b)). As discussed in Chapter 2, the results at the discarded mission candidate, placed at the SV L_3, L_4 and L_5 points, might improve if the observation window is longer, thus increasing the likelihood of the NEO passing through the FOR on its collision course with Earth.

- *Addition of a second ground-based telescope in the southern hemisphere*

  As discussed in the draft journal article, the results of the space-based telescopes were combined with only one ground-based telescope, which was located in the northern hemisphere. Since it was observed that many of the VIS observations at large solar elongations were also obtained by ground-based surveys, it is to be expected that the VIS results change accordingly if a second ground telescope is added, most likely in the southern hemisphere. This would strengthen the selection of the TIR waveband, which still contributes to the total number of observations, regardless of the number of ground telescopes, as most of the TIR observations are obtained at small solar elongations, where ground-based surveys cannot reach.

- *Implementation of a control law for the sail attitude along the transfer trajectory*

  For the design of the transfer trajectory, a different, but constant, sail attitude has been assumed along each of the segments of the discretised trajectory. As a result, the obtained attitude profile has the shape of a stair-step graph, and is thus not perfectly smooth. Although the fly-ability of the solar sail is ensured by limiting the rate of change of the sail angles, one could also implement a non-constant continuous control law in order to track the reference trajectory using variations in the sail attitude angles, similar to what has been done in the work by (Biggs et al., 2009).

- *Continuation on the fixed TOF of the transfer trajectory*

  Although the design of the transfer trajectory starts by obtaining an initial guess that results from a multi-objective optimisation in TOF and infeasibility, the resulting feasible transfer trajectory that is obtained in Chapter 2 by means of a multiple shooting differential corrector is actually sub-optimal in terms of TOF. Therefore, after finding a feasible trajectory in the CR3BP, a continuation on the fixed TOF could have been used in order to gradually reduce the flight time, such as in the work by Fernández Mora (2019). Unfortunately, due to time constraints, this continuation scheme was not applied.

- *Selection of the launch vehicle*

  The selected transfer scheme assumes a shared-launch scenario with ESA's Euclid mission, yet it has already been decided that Euclid will be carried into a direct transfer orbit by a Soyuz ST 2-1b launch vehicle departing from Europe's Spaceport in French Guiana. Therefore, it might not be possible that the one or two space-based telescopes are also launched by means of this launch vehicle. To this aim, an estimation of the required payload mass for our mission should be determined and checked whether the maximum payload mass of the Soyuz ST 2-1b launch vehicle is not exceeded.

A

VERIFICATION AND VALIDATION

This Appendix includes all the numerical and qualitative tests and comparisons that were conducted throughout the thesis in order to guarantee that the models and algorithms were implemented correctly, and thus ensure that the outcome and conclusions of this research work are reliable.

A.1. DYNAMICAL MODELS

The dynamical framework used throughout the paper consists of the following models:

- Circular restricted three-body problem (CR3BP).
- Ideal solar-sail model.
- Elliptic restricted three-body problem (ER3BP.)

These models are discussed as follows. First, the CR3BP is validated in Section A.1.1, followed by the ideal solar-sail model in Section A.1.2 and the solar-sail CR3BP in Section A.1.3. Finally, the ER3BP is verified and validated in Section A.1.4.

A.1.1. CIRCULAR, RESTRICTED, THREE-BODY PROBLEM

In the ballistic CR3BP, as discussed in Section II.A, there are five equilibrium points, or libration points, where gravitational and centrifugal forces balance each other. This means that if a spacecraft is placed at any of the libration points with zero velocity, it will not experience any acceleration with respect to the synodic reference frame. Table A.1 presents the location of the five libration points of the Sun-Earth (SE) and Sun-Venus (SV) three-body systems in the SE and SV synodic reference frames, respectively, which have been

compared with the reference values found in Wakker (2015) and computed with an on-line tool[1]. It is possible to see that the results coincide up to the 12^{th} decimal digit, which corresponds to a deviation in position of approximately 1 m. Then, Table A.2 presents the associated acceleration of a spacecraft with zero velocity placed at these locations with respect to the SE and SV synodic reference frames. The obtained results show that the spacecraft experiences a negligible acceleration at the libration points, which can be attributed to rounding errors, and it can thus be concluded that the dynamics of the CR3BP are correctly implemented.

Table A.1: Comparison of the reference and computed locations of the libration points of the SE and SV three-body systems.

Lagrange Point		Reference Position (non-dim) Wakker (2015)			Position (non-dim)		
		x	**y**	**z**	**x**	**y**	**z**
Sun-Earth	L_1	0.990026783028	0	0	0.990026783029	0	0
	L_2	1.010033925070	0	0	1.010033925070	0	0
	L_3	-1.000001251379	0	0	-1.000001251379	0	0
	L_4	0.499996996691	0.866025403784	0	0.499996996691	0.866025403784	0
	L_5	0.499996996691	-0.866025403784	0	0.499996996691	-0.866025403784	0
Sun-Venus	L_1	0.990682458814	0	0	0.990682458816	0	0
	L_2	1.009370855464	0	0	1.009370855464	0	0
	L_3	-1.000001019879	0	0	-1.000001019879	0	0
	L_4	0.499997552294	0.866025403784	0	0.499997552294	0.866025403784	0
	L_5	0.499997552294	-0.866025403784	0	0.499997552294	-0.866025403784	0

A.1.2. IDEAL SOLAR-SAIL MODEL

In order to verify the ideal solar-sail model, a polar plot of the acceleration components is created and compared to the one obtained by Vergaaij (2018). To this aim, the forces along and perpendicular to the Sun-sail line are computed for an ideal sail with lightness number equal to $\beta = 0.0363$ and a mass of 45 kg, as shown in Figure A.1. The polar plot is recreated by fixing the clock angle to $\delta_s = 0$ and varying the cone angle α_s from $-90°$ to $90°$. It can be seen that an exact match is obtained between the reference values from (Vergaaij, 2018) and the ones calculated in this work, thus verifying the implementation of the ideal sail model and the solar-sail acceleration.

A.1.3. SOLAR SAIL, CIRCULAR, RESTRICTED, THREE-BODY PROBLEM

Solar sailing adds another force, and thus another acceleration term, to the CR3BP model, as discussed in Section III. The modified equations of motion that result from the addition of the solar-sail acceleration to the CR3BP yield new equilibrium solutions in the form of surfaces of AEPs.

[1] Orbit Simulator. URL http://orbitsimulator.com/formulas/LagrangePointFinder.html (Access date 2019-05-24).

Table A.2: Acceleration with respect to the SE and SV synodic reference frames of a spacecraft placed at the libration points with zero velocity.

Lagrange Point		Acceleration (non-dim)		
		x	**y**	**z**
Sun-Earth	L_1	$3.916703766871 \cdot 10^{-12}$	0	0
	L_2	$5.343246678446 \cdot 10^{-12}$	0	0
	L_3	$-2.140841061716 \cdot 10^{-13}$	0	0
	L_4	$-1.349429364095 \cdot 10^{-16}$	$-3.150411992370 \cdot 10^{-16}$	0
	L_5	$-1.349429364095 \cdot 10^{-16}$	$3.150411992370 \cdot 10^{-16}$	0
Sun-Venus	L_1	$2.061026696532 \cdot 10^{-11}$	0	0
	L_2	$8.222589276130 \cdot 10^{-16}$	0	0
	L_3	$-1.738438280845 \cdot 10^{-13}$	0	0
	L_4	$-2.069229492342 \cdot 10^{-16}$	$-3.642398374289 \cdot 10^{-16}$	0
	L_5	$-2.069229492342 \cdot 10^{-16}$	$3.642398374289 \cdot 10^{-16}$	0

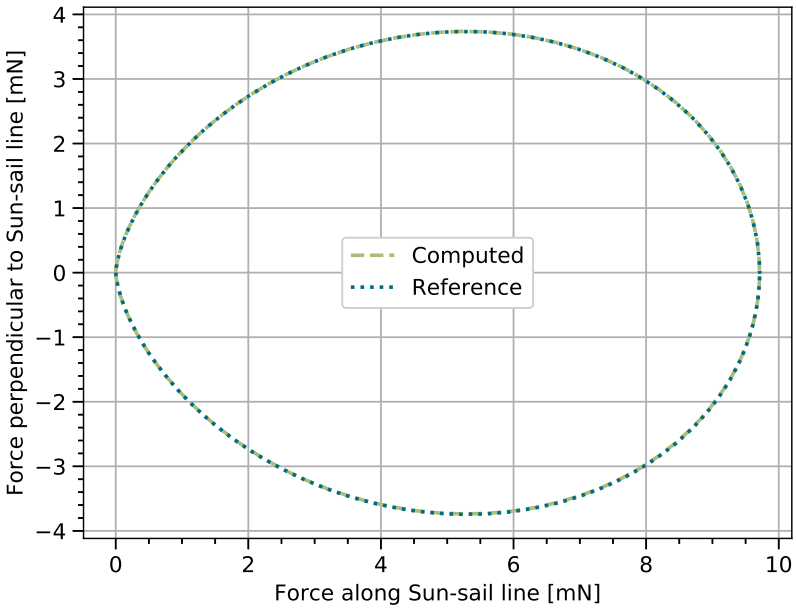

Figure A.1: Comparison of the reference (Vergaaij, 2018) and computed sail performance of a solar sail with lightness number $\beta = 0.0363$ and mass of 45 kg.

The correct determination of AEPs is verified and validated by comparing the contour plots of AEPs in the Sun-Earth three-body system, see Figure A.2. This figure shows the projections on to the (x, y)-plane and (x, z)-plane of the surfaces of AEPs, resulting in contours plots of constant lightness number, extracted from (Heiligers et al., 2014) (Fig. A.2a) and computed in this work (Fig. A.2b). In both these figures, the grey areas indicate those regions in which no AEPs exist, as they would require an acceleration with a component in the direction of the Sun, which the solar sail is unable to produce. The white solid line represents the

AEPs that would have been accessible by an ideal solar-sail performance of $\beta = 0.0363$. And lastly, the yellow cone indicates the solar exclusion zone, in which a satellite would suffer from solar radio interference during communications, and is thus advisable to avoid.

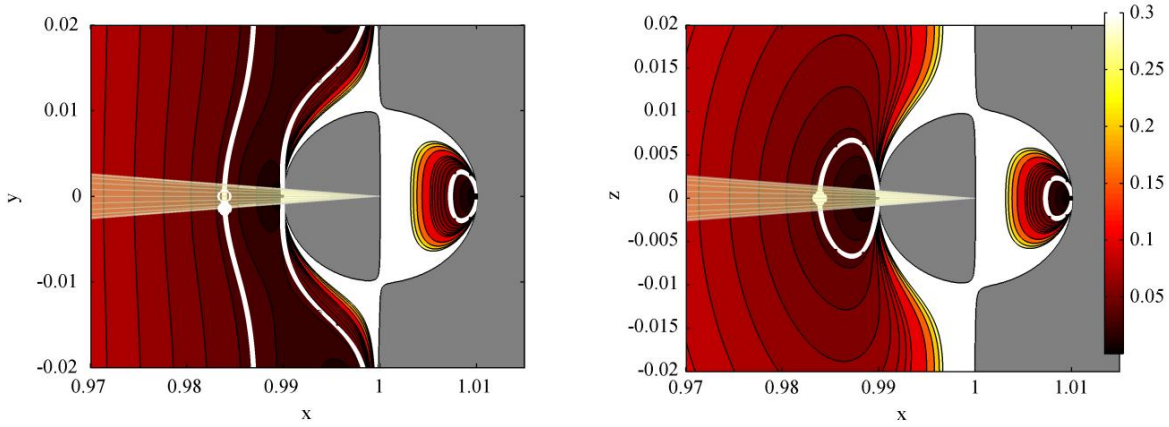

(a) Reference (Heiligers et al., 2014).

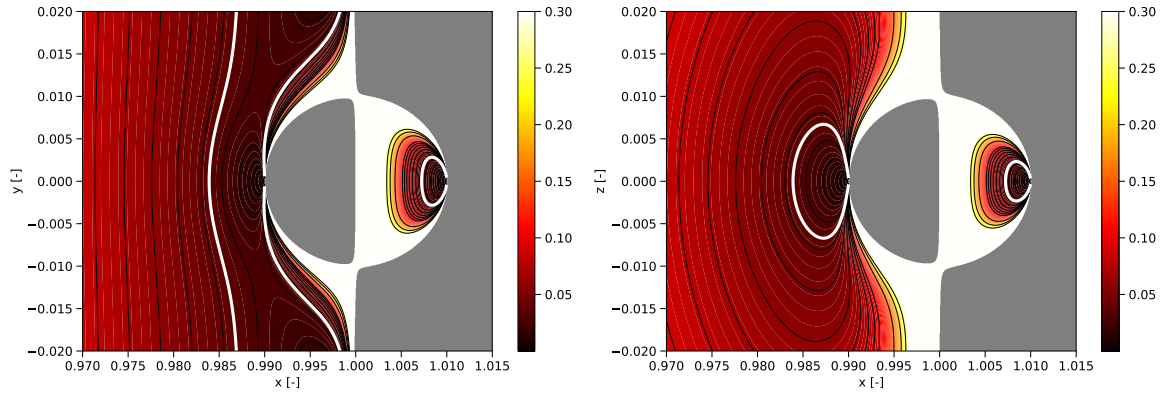

(b) Computed.

Figure A.2: Intersections with the (x, y)- and the (x, z)- planes of the surfaces of AEPs. The white sold line is the contour for an ideal solar-sail performance of $\beta = 0.0363$. The grey areas indicate regions in which no AEPs exist. The yellow cone indicates the solar exclusion zone.

While the traditional CR3BP has only five libration points, solar-sail CR3BP can generate an infinite number of AEPs inside certain allowed regions, as shown in Figure A.2. The classical Lagrange libration points exist when $\beta = 0$, for which the level surfaces collapse to the libration points. Then, as the sail lightness number increases from 0 to 1, the collinear libration points move closer to the Sun (hence, they are known as sub-Lagrange points). This effect can be observed in Figure A.3, where the evolution of the Sun-Earth collinear libration point locations with β is shown. Figure A.3a is obtained from (McInnes, 2000) and compared with the values calculated in this work in Fig. A.3b; it is possible to see that both plots follow the same trend, and it can thus be concluded that the determination of the collinear AEPs is correctly implemented.

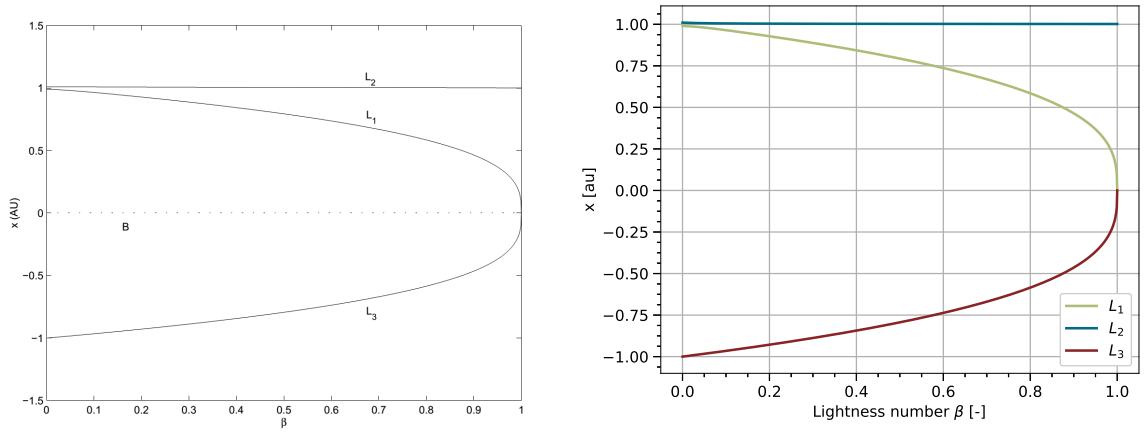

(a) Reference (McInnes, 2000).

(b) Computed.

Figure A.3: Evolution of the Sun-Earth collinear libration point locations with β.

A.1.4. ELLIPTICAL, RESTRICTED, THREE-BODY PROBLEM

Firstly, it is verified and validated that the ER3BP coincides with the circular case when the eccentricity is equal to zero, *i.e.*, $e = 0$. Secondly, as discussed in the work by Baoyin and McInnes (2006), equilibrium points can also be found in the ER3BP, such that $X'' = Y'' = Z'' = 0$ in Eq. (7). As discussed in (Baoyin and McInnes, 2006), the required sail lightness number and sail attitude, defined by $\hat{\mathbf{n}}$, to maintain an equilibrium point in the solar-sail ER3BP are:

$$\hat{\mathbf{n}} = -\frac{\Delta\Omega_E}{\|\Omega_E\|} \tag{A.1}$$

$$\beta = -\frac{1}{1-\mu}\frac{(\nabla\Omega_E \cdot \hat{\mathbf{n}})\, R_1^4}{(\mathbf{R}_1 \cdot \hat{\mathbf{n}})^2} \tag{A.2}$$

where Ω_E is the effective potential function in the ER3BP, given in Eq. (8).

Therefore, for an equilibrium point in the Sun-Earth ER3BP at $X = 0.99$, $Y = 0.01$, $Z = 0.0$, the required sail lightness number is equal to $\beta = 0.02867$. For this solar-sail lightness number, a solar-sail spacecraft placed at this location with zero velocity experiences the following acceleration, according to the equations of motion of the ER3BP implemented:

$$X'' = -5.9367 \cdot 10^{-11}, \quad Y'' = 1.0405 \cdot 10^{-12}, \quad Z'' = 0.0$$

which is negligible and can be attributed to rounding errors, thus verifying the correct implementation of the dynamics of the ER3BP.

A.2. NUMERICAL METHODS

In this research work, several high-order analytical approximations of the equations of motion have been used to generate initial guesses for periodic orbits about the equilibrium points. Since the resulting periodic orbits are only linear approximations to the solutions of the full non-linear system, a differential corrections scheme has been implemented and applied to correct these initial conditions. This section verifies the cor-

rect implementation of the differential corrections method and the determination of initial guesses for the generation of periodic orbits in Section A.2.1 and Section A.2.2, respectively.

A.2.1. DIFFERENTIAL CORRECTIONS METHOD

In order to verify the correct implementation of the differential corrections method, this technique is applied to correct the initial conditions given in Howell (1984) for a family of halo orbits about the L_1 point of a CR3BP with $\mu = 0.04$. Then, the corrected initial conditions are numerically integrated and the resulting orbits are plotted with respect to a synodic reference frame and compared to the solutions found in Howell (1984).

Table A.3 contains the initial conditions, $(x_0, z_0, \dot{y}_0)$, extracted from the reference Howell (1984), together with the half-period of the orbit, *i.e.*, the non-dimensional time at half the period for the given orbit. The calculated half-period of the orbit and the number of iterations until convergence when applying the differential corrections method are also presented in Table A.3. Firstly, it is possible to see that the obtained half-period of the orbits coincide with the reference values up to the 5^{th} decimal digit. Secondly, only one iteration is required to correct the given initial conditions, which implies that the method is working as expected. Thirdly, as shown in Figure A.4, the halo orbits that result from the numerical integration of the corrected initial conditions are exactly the same as the ones found in Howell (1984) (note that not all initial conditions are given in Howell (1984), and it is thus only possible to recreate some of the orbits). Therefore, the differential corrections method is verified and validated.

Table A.3: Initial conditions and half-periods for the L_1 halo-orbit family for $\mu = 0.04$, together with the number of iterations that is required to reach convergence in the differential corrections method. Source: Howell (1984)

x_0	0.723268	0.729988	0.753700	0.777413	0.801125	0.817724
z_0	0.040000	0.215589	0.267595	0.284268	0.299382	0.313788
$\dot{y}_0$	0.198019	0.397259	0.399909	0.361870	0.312474	0.271306
Reference Half-Period	1.300177	1.348532	1.211253	1.101099	1.017241	0.978635
Computed Half-Period	1.300177	1.348533	1.211252	1.101095	1.017240	0.978635
Number of iterations	1	1	1	1	1	1

A.2.2. INITIAL GUESS GENERATION

Two different methods for generating initial guesses for the generation of periodic orbits have been used and implemented in this work. In Section III.C, the approach in Baoyin and McInnes (2006) and Waters and McInnes (2007) is used to compute solar-sail halo orbits around AEPs in the SE CR3BP. Then, in Section VII.A.2, the approach in Richardson (1980) is used to generate a family of halo orbits around the L_2 point in the SE CR3BP. The verification of these two methods is quite straightforward; since the differential corrections method has been able to converge into periodic orbits for both cases, it can be assumed that the generation of initial guesses has been implemented correctly.

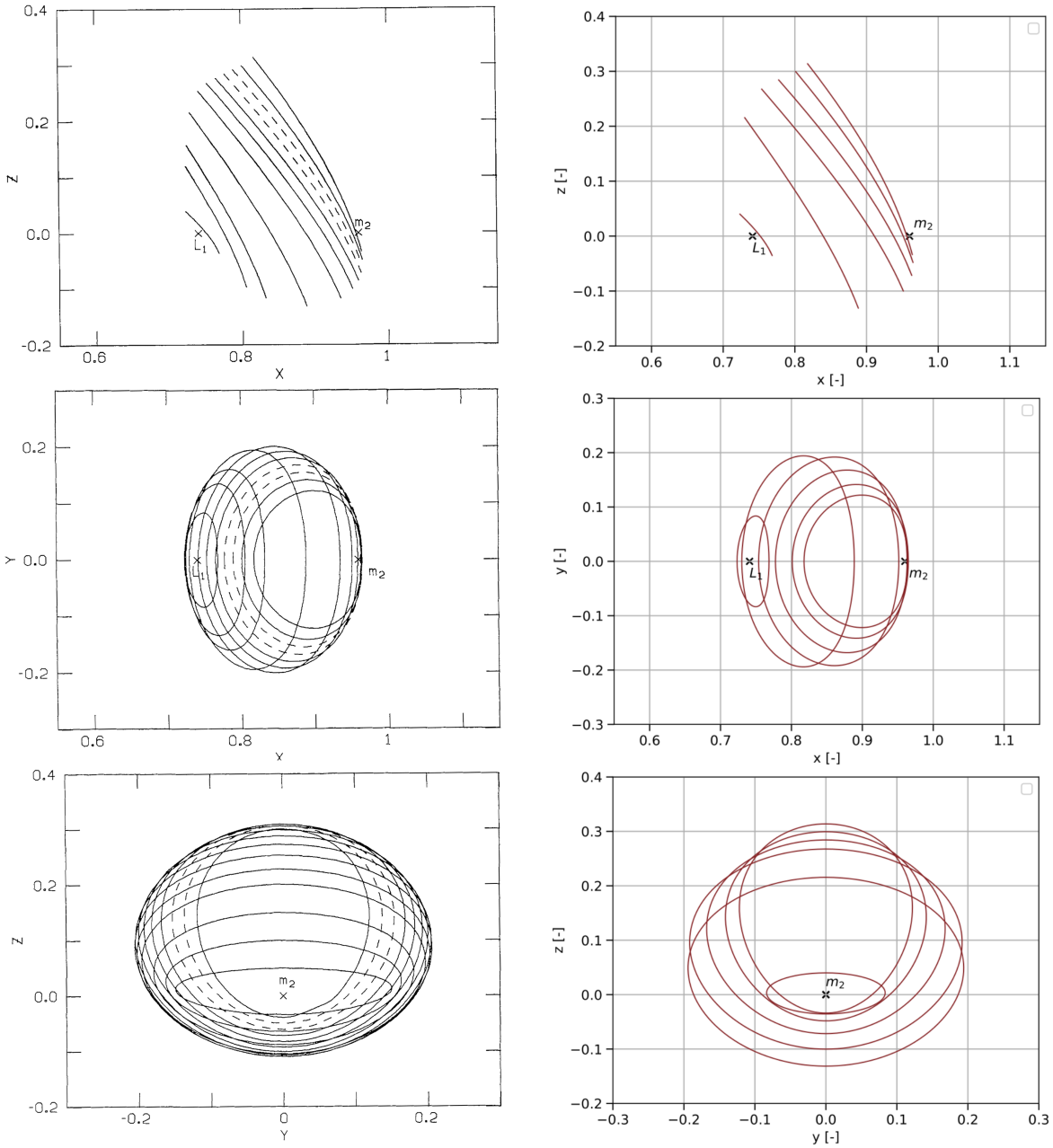

(a) Reference (Howell, 1984).

(b) Computed.

Figure A.4: L_1 halo-orbit family for $\mu = 0.04$.

A.3. DETECTABILITY OF NEOS

The detectability of NEOs is determined by the Signal-to-Noise Ratio (SNR) at the detector, which is simply the ratio of the object's signal and the noise at the detector. The object's signal depends on the wavelength of the detector: for a visible detector, the signal is given by the optical brightness or apparent magnitude of the object (Section A.3.1), and for an infrared detector, the signal is given by the thermal emission of the object (Section A.3.2). Then, regarding the noise at the detector, the major contribution is due to the brightness of the background. For space-based sensors, the main source of light to the background brightness is the

zodiacal light (Section A.3.3). This section discusses the verification and validation of all these elements that must be taken into account when computing the SNR at the detector, which have been defined and presented previously in Section V.D.

A.3.1. OPTICAL BRIGHTNESS

To verify the correct implementation of the optical brightness of NEOs, use is made of ESA's Near-Earth Object Population Observation Program (NEOPOP). NEOPOP is a software developed in 2015 within the framework of activities related to ESA's Space Situational Awareness (SSA) program, which can be downloaded for free through their website[2]. Among its many functionalities, this tool does a close approach analysis of any input population of NEOs and provides information regarding the objects at the time of closest approach. One of the outputs of such analysis is the apparent magnitude m of the object at the time of closest aproach. Although the method for computing m is not exactly the one implemented in this work (explained in Section A.3.1), the obtained values are a good reference to check whether the method is coherent.

Table A.4 then provides the necessary information to compute m for three different random asteroids: the physical properties of the object, *i.e.*, the absolute magnitude H and the visual albedo p_v, and the geometry at the time of closest approach, *i.e.*, the heliocentric distance r, the geocentric distance Δ and the phase angle α (the angle Sun-object-Earth). Then, Table A.5 presents both the reference apparent magnitude, computed using NEOPOP, and the obtained apparent magnitude, using the method implemented in this work. It is possible to see that there is a slight discrepancy in the results, of approximately 0.06–0.26 visual magnitudes. However, this deviation in absolute magnitude corresponds to a deviation in diameter of approximately 0.8–2.3 m (using Eq. (15)), which is very small. Therefore, it is assumed that the method for computing the optical brightness of NEOs is verified and validated.

Table A.4: Geometry at the time of closest approach for three different asteroids.

Asteroid	r [au]	Δ [au]	α [deg]	H	p_v
#1	3.1659	4.1129	5.13	19.95	0.2125
#2	1.2149	2.1281	14.64	19.87	0.4098
#3	0.9518	0.7572	69.21	25.31	0.1077

Table A.5: Comparison of the reference and computed apparent magnitude of three different asteroids.

Asteroid	Reference m	Computed m
#1	26.01	25.75
#2	22.46	22.23
#3	25.75	25.69

[2] ESA NEO Coordination Centre. URL http://neo.ssa.esa.int/neo-population (Access date 2019-02-15)

A.3.2. INFRARED BRIGHTNESS

Two different thermal models have been implemented in order to compute the infrared brightness of NEOs: the Standard Thermal Model (STM) and the Near-Earth Asteroid Thermal Model (NEATM). To verify the correct implementation of these two methods, use is made of Fig. A.5a, which has been extracted from (Harris and Lagerros, 2002). This plot shows both the STM and NEATM fits to TIR fluxes of the asteroid 1999 LD_{31} from observations with an IR space-based telescope: the solid line in Fig. A.5a represents the fit provided by the STM, with a beaming parameter $\eta = 0.756$, and the dotted line in Fig. A.5a represents the fit provided by the NEATM, with $\eta = 1.22$. The aim is to replicate this plot by computing the thermal flux with both thermal models using the best-fit parameters obtained in the fitting process, which are presented in Table A.6, and the information regarding the geometry at the time of observation Harris et al. (2001): $r = 2.696$ au, $\Delta = 1.873$ au and $\alpha = 14.3°$. The result is shown in Fig. A.5b; it is possible to observe that the obtained thermal fluxes coincide with the values from the reference plot, thus verifying the correct implementation of both thermal models.

Table A.6: Best-fit parameters values for the thermal models. Source: Harris et al. (2001)

Model	p_v	D [km]	η
STM	0.036	12.2	0.756
NEATM	0.020	16.3	1.22

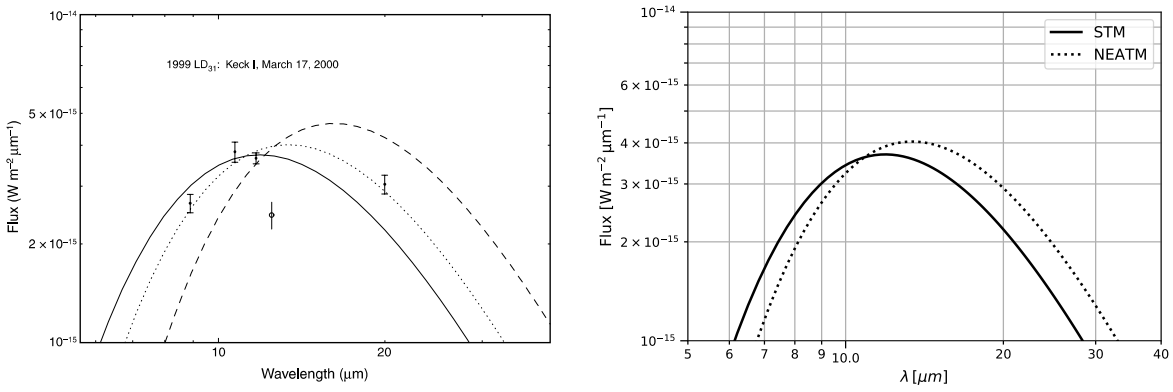

(a) Reference (Harris and Lagerros, 2002).

(b) Computed.

Figure A.5: Model fits to thermal-infrared fluxes of the asteroid 1999 LD_{31}. The solid line represents the fit provided by the STM, with $\eta = 0.756$, and the dotted line represents the fit provided by the NEATM, with $\eta = 1.22$.

A.3.3. SKY BRIGHTNESS

As discussed in Section V.D.3, in this paper, the background signal is computed assuming only the contribution of the zodiacal light. At visible wavelengths, the zodiacal light data has been taken from (Daniels, 1977) and (Leinert et al., 1998), which provide tabulated zodiacal fluxes as a function of ecliptic latitude and

longitude. At infrared wavelengths, however, the brightness of zodiacal light has been computed using the three-dimensional model of the interplanetary dust cloud by Kelsall et al. (1998), which is verified and validated next in Section A.3.3.

Since the zodiacal brightness is obtained for an observer at Earth, it has been assumed that the zodiacal light at both wavebands varies with heliocentric distance according to (Leinert et al., 1998), and a correction factor has thus been estimated in Section A.3.3.

INFRARED BRIGHTNESS OF THE ZODIACAL LIGHT

In the parametric model used to compute the infrared brightness of the zodiacal light, the three-dimensional dust density distribution is composed of multiple components – a smooth cloud, three dust bands, and a circumsolar dust ring just beyond 1 au. First, isodensity contours of each of the components of the model density are shown in Fig. A.6b, and compared to the ones extracted from the reference (Kelsall et al., 1998) in Fig. A.6a. Although the quality of the reference plots does not allow a very accurate comparison of the results, it is possible to see that the overall shape of the contour plots is extremely similar. The only noticeable difference is seen in the plot of the circumsolar ring, where the ring is slightly smaller around 1 au distance from the Sun. This discrepancy in the results is to be expected, as the zodiacal dust model implemented neglects the contribution due to the trailing blob in the circumsolar ring, which follows the Earth in its orbit.

Table A.7 then presents quantitative estimates of the contribution from each of the components of the zodiacal dust to the total background's irradiance, at different IR wavelengths λ, observation times and locations, for an observer at Earth. While the obtained estimates are generally in the same order of magnitude as the reference values, it is possible to see how the contribution due to the circumsolar ring is approximately half of the reference estimates, which can be attributed again to the neglected Earth-trailing blob. The rest of the results are fairly similar to the reference ones. The slight discrepancies that are observed can be due to: the Earth's position at the given observation time, which is not very precise, and the neglected colour correction that the model suggests using in order to compute the zodiacal brightness in a fashion consistent with the DIRBE data, from which the model parameters are obtained (Kelsall et al., 1998).

Nonetheless, it is important to remark that the irradiance estimates are given in units of MJy/sr, which correspond to 10^{-35} W/m^2/Hz/sr. Therefore, it can be assumed that the zodiacal dust model has been implemented correctly. In order to take into account the assumptions considered, a sensitivity analysis on the uncertainty in the background's irradiance has been performed in Appendix A of Section 2.

VARIATION WITH HELIOCENTRIC DISTANCE

The zodiacal background model implemented varies with the ecliptic latitude and longitude of the line-of-sight with respect to the Earth and the time of observation, *i.e.*, Earth's position during its orbit around the Sun. For those space-based surveys further from Earth, the model needs to be corrected in order to take into account the different heliocentric distance and height above the ecliptic of the observer.

Figures A.7 and A.8 show how the brightness of the zodiacal light for both VIS and TIR wavebands, respectively, changes with the heliocentric distance R_0 (measured in the ecliptic) for different heights Z_0 above

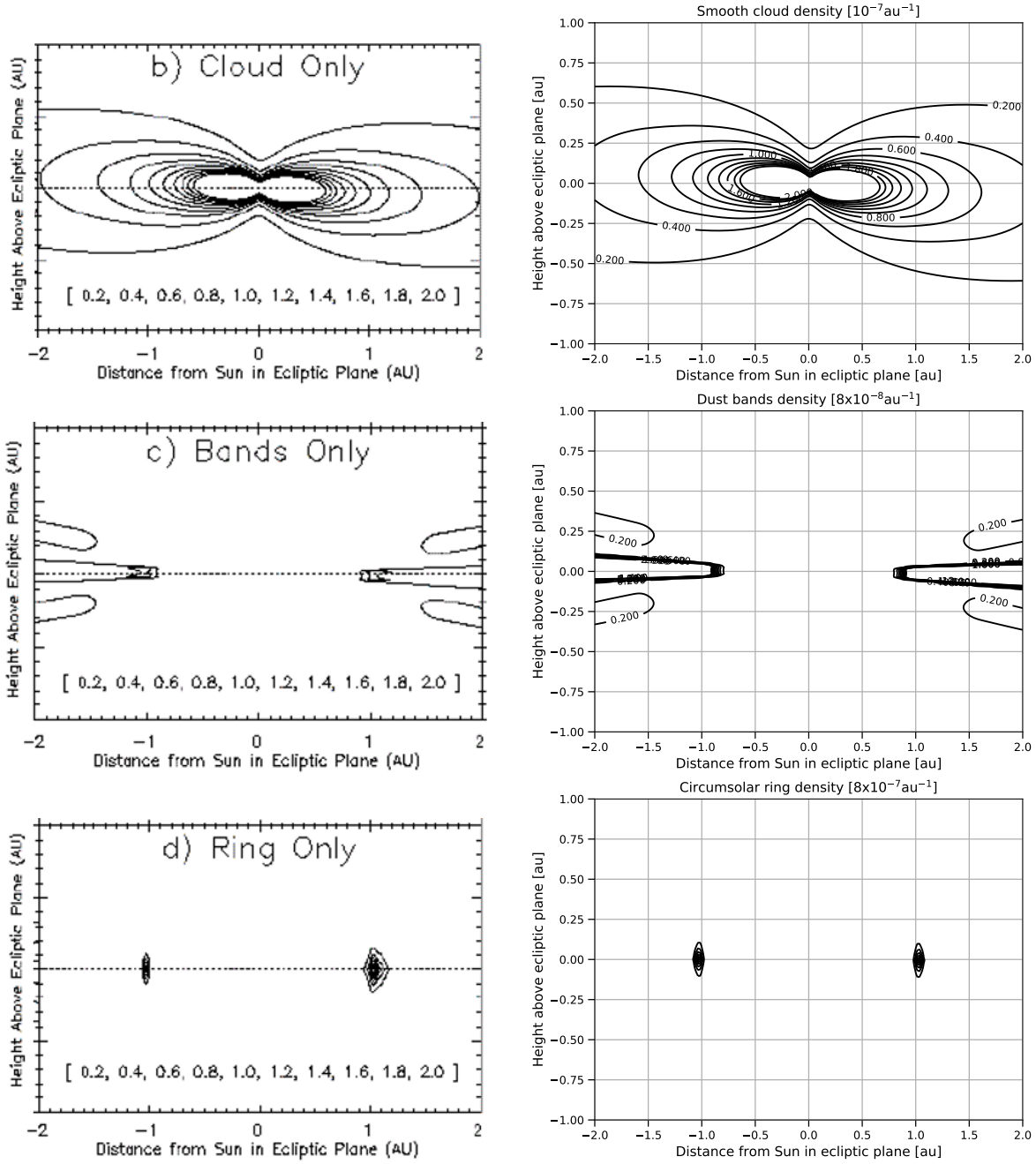

(a) Reference (Kelsall et al., 1998). (b) Computed.

Figure A.6: Isodensity contours of the zodiacal dust model components, shown for a cross-sectional slice perpendicular to the ecliptic plane: smooth cloud (top), dust bands (center) and circumsolar ring (bottom).

the ecliptic plane. Although the authors suggest that these curves cannot be very accurate, due to the uncertainties in the three-dimensional dust distribution (Leinert et al., 1998), this research work has assumed that the zodiacal background varies with R_0 according to Fig. A.7 and Fig. A.8. Since the out-of-plane amplitudes of the orbits of the space-based telescopes are extremely small with respect to the order of magnitude of the plots, *i.e.*, $\sim 500\,000$ km ≈ 0.003 au, the different height above the ecliptic of the observer is neglected.

A correction factor f_{zod} has then been computed in order to take into account the heliocentric distance

Table A.7: Comparison of the quantitative estimates of the contribution from each density component of the zodiacal dust model to the total background's irradiance. The location of the line-of-sight is given in geocentric ecliptic coordinates $(\lambda_\oplus, \beta_\oplus)$. The reference estimates are taken from (Kelsall et al., 1998).

Location $(\lambda_\oplus, \beta_\oplus)$	Observation date	λ [μm]	Smooth cloud [MJy/sr]		Dust bands [MJy/sr]		Ring + Blob [MJy/sr]	
			Reference	Computed	Reference	Computed	Reference	Computed
(137°, 47°)	1990-05-09	4.9	0.449	0.447	0.00114	0.001	0.0251	0.0114
(122°, 0°)	1990-04-19	12	28.476	29.33	1.938	1.66	3.324	1.59
(122°, 0°)	1990-04-19	4.9	0.679	0.643	0.0141	0.012	0.109	0.049

R_0 of the observer, which is multiplied with the zodiacal light estimate, yielding a more accurate value of the background's irradiance that varies with the location of the observer. Figure A.9 shows the estimated correction factors using the different data provided by Leinert et al. (1998). For an observer at Earth, the computed correction factors in all cases are equal to one, *i.e.*, the zodiacal light given by the model is correct. Then, as the observer goes closer to the Sun, the correction factors increases, which is to be expected since the zodiacal brightness decreases with heliocentric distance.

In this work, the correction factor has been assumed constant and equal to the one computed in the worst-case scenario. Therefore, since both orbit candidates are located at a distance closer to the Sun than the Earth, the VIS correction factor is computed using the data with a viewing-direction parallel to the ecliptic plane, and the TIR correction factor is computed using the data with a viewing-direction parallel to the ecliptic plane and a wavelength of 12 μm[3]. As a result, for the SV case located at a distance ~0.7233 au, the correction factors are $f_{\text{zod,VIS}} \approx 2.11$ and $f_{\text{zod,TIR}} \approx 2.10$.

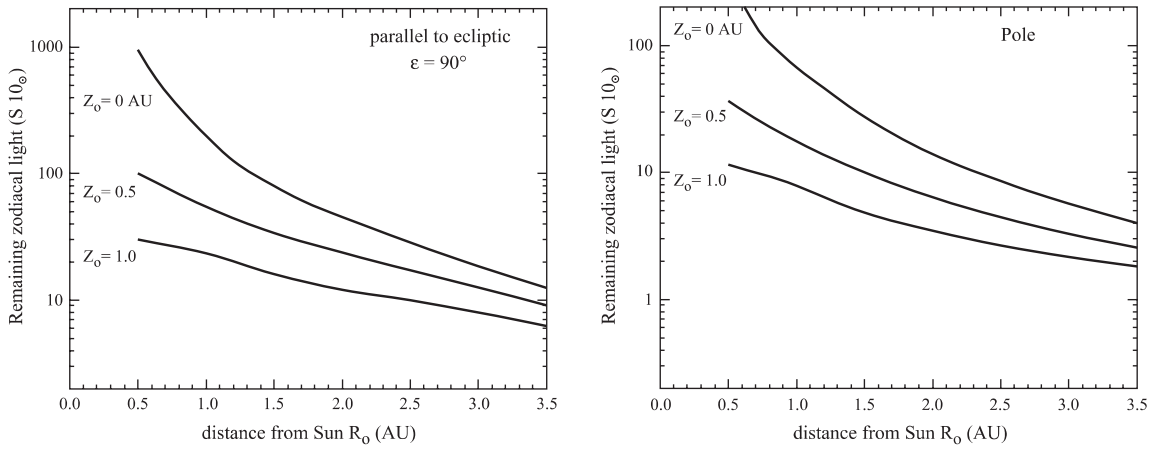

Figure A.7: Decrease of the visual brightness of the zodiacal light when the observer moves out of the ecliptic plane, for a viewing-direction parallel to the ecliptic plane (left) and for a viewing-direction towards the ecliptic pole (right). Source: (Leinert et al., 1998)

[3]Note that this wavelength is not inside the waveband of the TIR space-based telescope considered in this work, but no other data was found available.

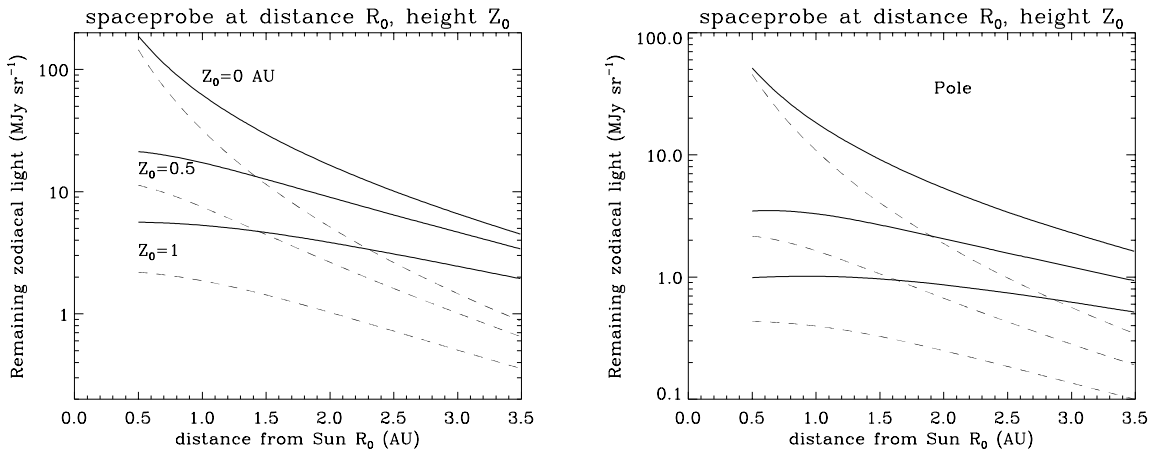

Figure A.8: Decrease of the infrared brightness of the zodiacal light when the observer moves out of the ecliptic plane, for a viewing-direction parallel to the ecliptic plane (left) and for a viewing-direction towards the ecliptic pole (right). The solid and dashed lines indicate the variation of brightness with heliocentric distance for a wavelength of 25 μm and 12 μm. Source: (Leinert et al., 1998)

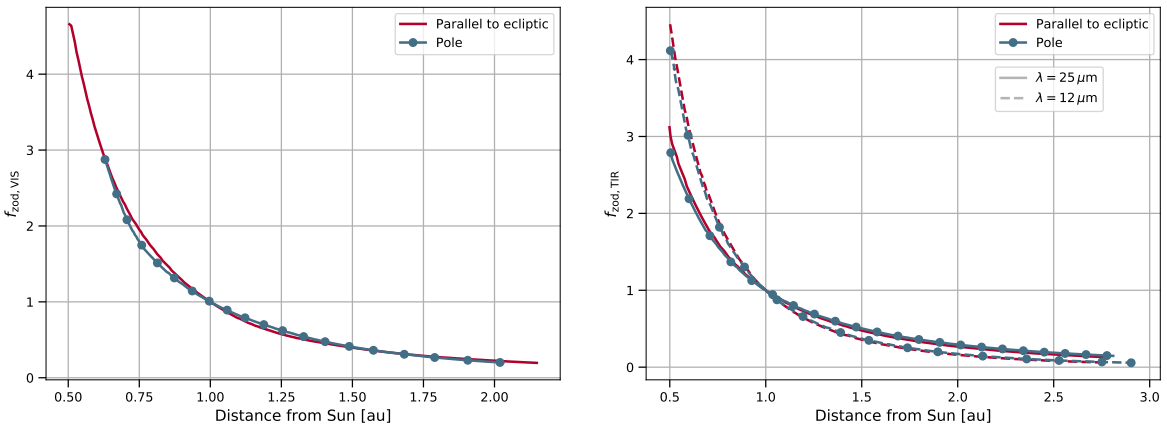

(a) VIS waveband.

(b) TIR waveband.

Figure A.9: Correction factors as a function of the heliocentric distance R_0 of the observer.

A.4. INTEGRATION OF THE SPACE-BASED SURVEY SIMULATION TOOL

The space-based survey simulation tool consists of:

- A space-based survey model.
- The orbits of each NEO in the Earth impactor population.
- The orbits of each space-based telescope considered.

Since this software tool has been developed during the one-year internship executed at the Planetary Defence Office within the SSA programme of ESA, it has been implemented using the Mission Analysis Software based on orbit facility (ORBSW), which was provided by the flight dynamics division at ESOC. Fortunately,

this software also contains a complete orbit propagation tool, which is thus used to determine the orbits of NEOs. Unfortunately, the two orbit candidates for the space-based telescope have been designed within the dynamical framework of the ER3BP. This implies that the orbits of the space-based telescopes must be imported in the ORBSW in order to have a fully-integrated space-based survey simulation tool.

A.4.1. IMPORT AND INTERPOLATION OF THE TELESCOPE'S STATE VECTORS

The orbits of both NEOs and space-based telescopes are determined considering the Sun and Earth's point-gravity acceleration. However, while the operational orbits have been designed in the pulsating-rotating reference frame, the orbit propagation tool in the ORBSW uses a more accurate ephemerides model (DE438s). This implies that, if the initial conditions of the telescope's orbits were propagated using this tool, there is a slight chance that the orbit would start diverting away from the desired path. Therefore, it has been assumed that the designed orbits are already a good approximation to the real orbits in the full DE438 model, and have been directly imported into the ORBSW software.

Instead of propagating the orbits of the space-based telescopes, the space-based survey simulation tool then uses an interpolation method to compute the state vector of the telescope at the requested epoch. The selected interpolation method is provided by the Python library 'SciPy', which has implemented a cubic spline data interpolated[4]. This assumption not only facilitates the integration of the tool, but also significantly decreases the computational time of the simulation of the space-based surveys.

To this aim, the orbits of the space-based telescopes were first propagated in the ER3BP for one revolution, and then exported to a .csv file. This file contains a total of $N = 1000$ state vectors, which was decided after analysing the error between the interpolated state vectors and the numerically integrated state vectors, as shown in Fig. A.10 for the SE orbit candidate, for different number of time steps N. For $N = 1000$, the error is kept within $10{\cdot}10^{-11}$ in both position and velocity, which corresponds to 1.5 m and $0.3{\cdot}10^{-3}$ mm/s, respectively. The same error analysis was done also for the SV candidate.

Once the files containing the ephemerides of the telescopes are created, the space-based survey simulation tool imports these files into the 'universe', treating thus the space-based telescopes as 'artificial' celestial objects.

A.4.2. TRANSFER TRAJECTORY DESIGN

The first phase of the transfer trajectory consists of an un-propelled shared-transfer phase, where the solar-sail spacecraft travels together with ESA's Euclid spacecraft along an asymptotic trajectory defined by the stable manifold associated to a halo orbit around the SE L_2 point that intersects with the vicinity of Earth. The second phase is simply a solar-sail propelled phase, where the motion is described by the equations of motion of the CR3BP, which have already been verified in Section A.1.1. The verification of the generation of invariant manifolds (IM) is a two-step process: first, the computation of IMs associated to equilibrium points is verified in Section A.4.2, and then the computation of IMs associated to periodic orbits is verified in

[4] SciPy - Interpolation. URL https://docs.scipy.org/doc/scipy/reference/interpolate.html (Access date 2019-09-25)

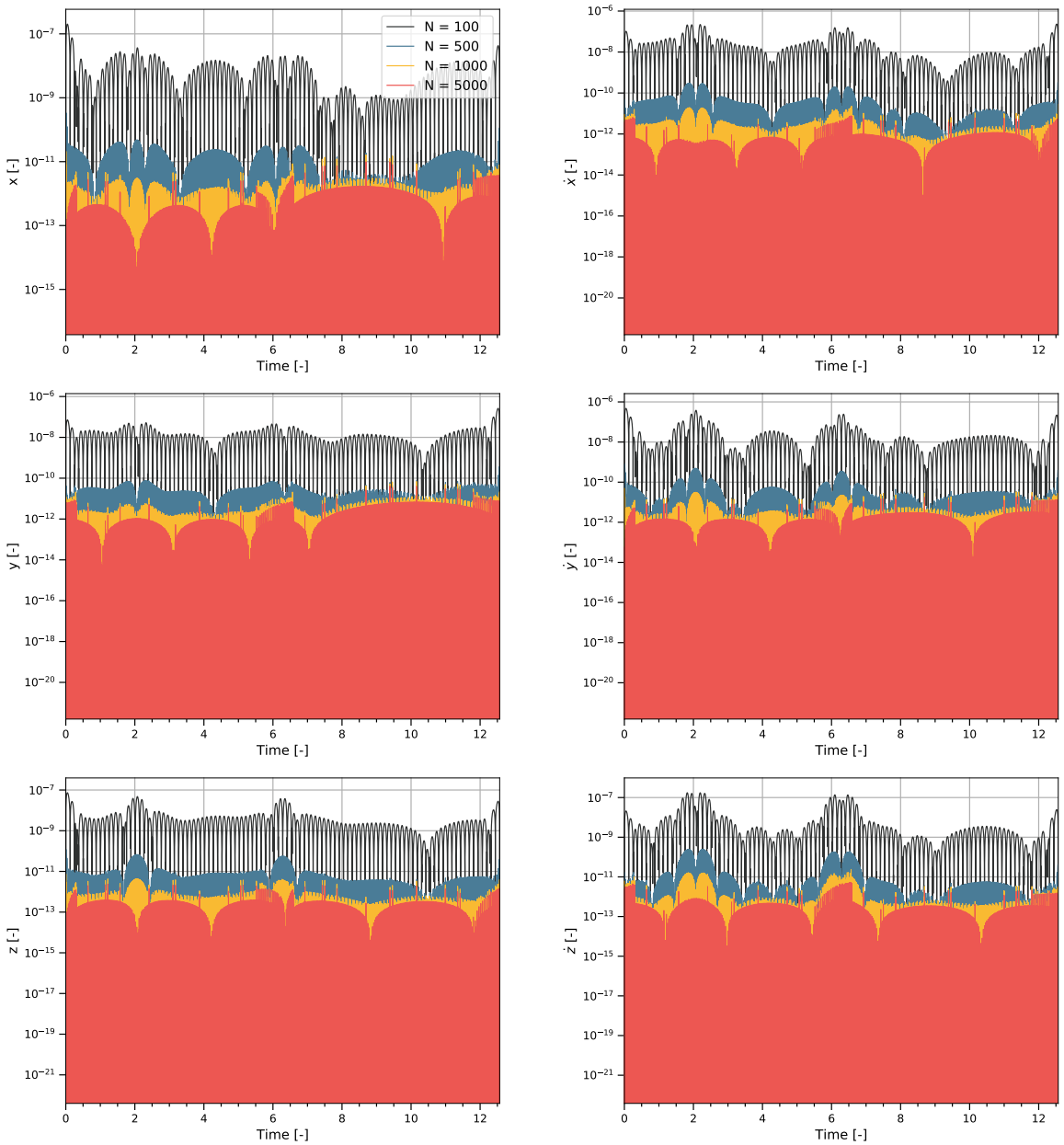

Figure A.10: Error between the interpolated state vectors and the numerically integrated state vectors for each component in the state vector, during one revolution of the space-based telescope at the SE sub−L_1 point.

Section A.4.2.

INVARIANT MANIFOLDS ASSOCIATED TO EQUILIBRIUM POINTS

First, the computation of IMs associated to equilibrium points in the solar-sail CR3BP is verified by comparing the obtained stable and unstable IMs associated to the solar-sail displaced collinear equilibrium points L_1 and L_2 for different values of lightness number β, as shown in Fig. A.11b, with the reference (Fernández Mora, 2019) (see Fig. A.11a). Although it is not possible to quantify the difference in the results, the scale and shape of the plots obtained are identical to the ones from the reference, and it can thus be assumed that the computation of IMs associated to AEPs is verified.

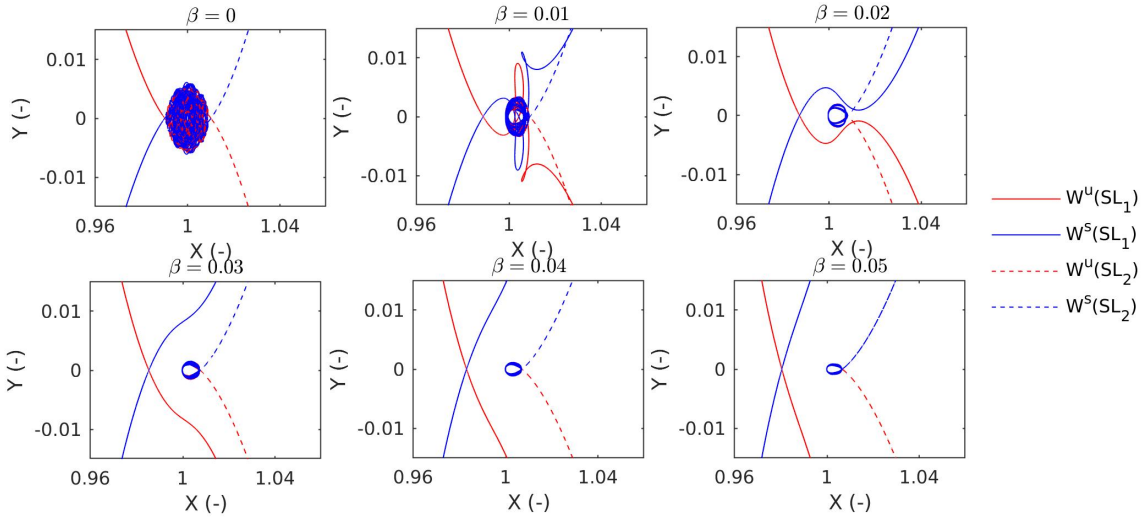

(a) Reference (Fernández Mora, 2019).

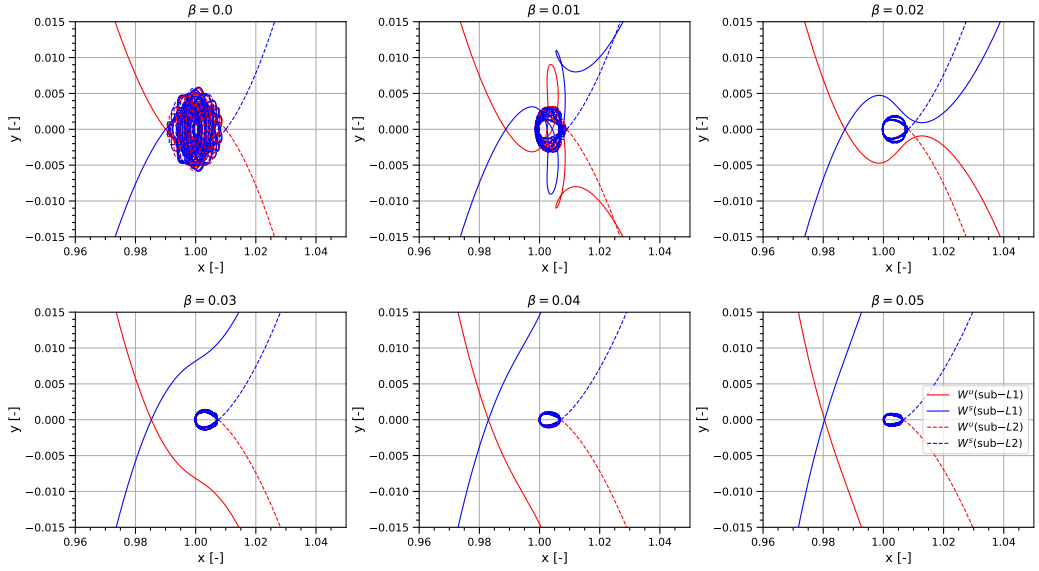

(b) Computed.

Figure A.11: Stable and unstable invariant manifolds associated to the collinear equilibrium points L_1 and L_2 in the vicinity of Earth for $\beta \in \{0, 0.01, 0.02, \cdots, 0.05\}$.

INVARIANT MANIFOLDS ASSOCIATED TO PERIODIC ORBITS

The verification of IMs associated to periodic orbits is also done by comparison between plots due to the absence of initial conditions for the periodic orbits found in literature. Therefore, the verification is done based on the IM associated to the halo orbit around the L_2 point in the Sun-Earth CR3BP, that was created in the research work with the aim of simulating ESA's Euclid operational orbit. As shown in Fig. 20, the obtained stable manifold associated to this orbit is very similar to what is found in the reference (Renk and Landgraf, 2014), in Fig. 19. Figure A.12 also shows both the stable and unstable IMs associated to that orbit. It is thus concluded

that the computation of IMs associated to periodic orbits is done correctly, as the stable IM obtained follows the same trend as the one found in the reference, and the unstable IM obtained presents the characteristic symmetry with the stable IM that is observed in literature (Topputo et al., 2004).

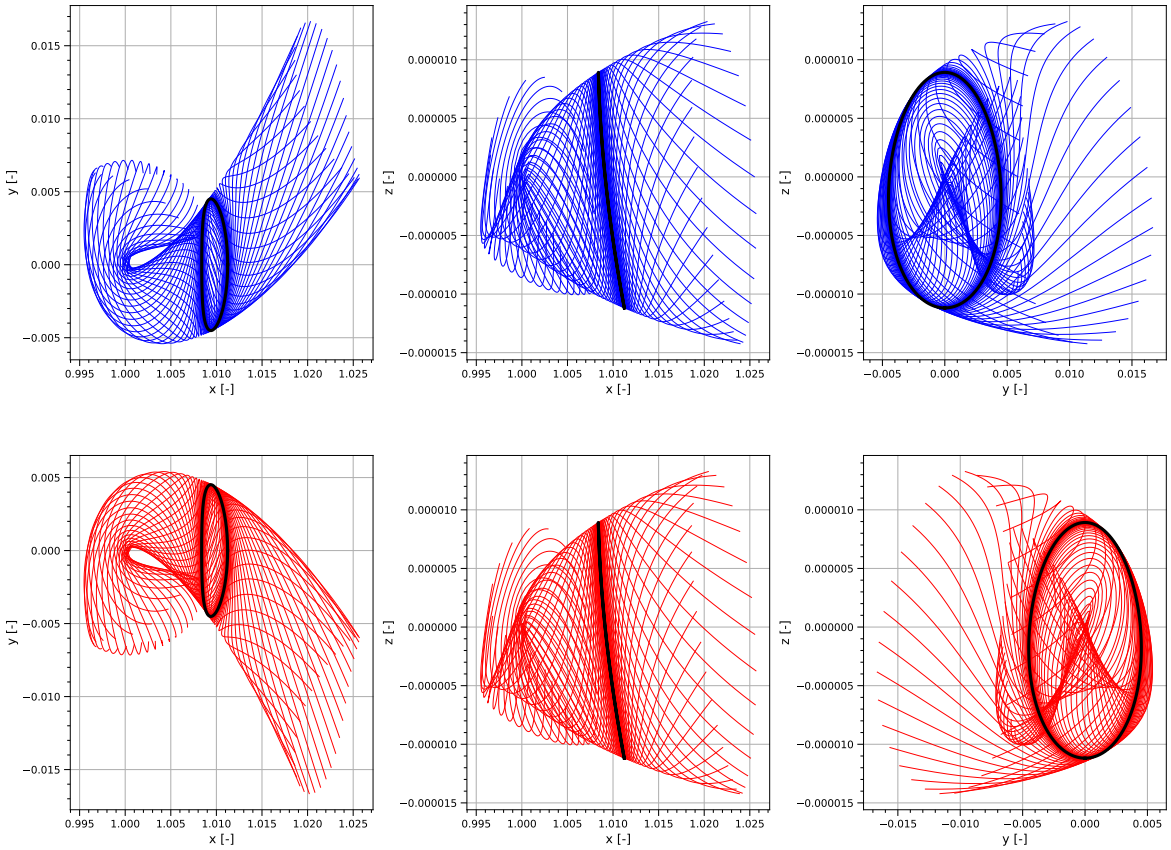

Figure A.12: Stable (top) and unstable (bottom) invariant manifolds associated to a halo orbit around the L_2 in the Sun-Earth CR3BP, similar to Euclid's operational orbit.

BIBLIOGRAPHY

Abbasi, V., Thorsteinson, S., Balam, D., Rowe, J., Laurin, D., Scott, L., and Doyon, M. The NEOSSat experience: 5 years in the life of Canada's space surveillance telescope. In *Proc. 1st NEO and Debris Detection Conference (Darmstadt, Germany, 22-24 January 2019)*. ESA Space Safety Programme Office, 2019. URL https://conference.sdo.esoc.esa.int/proceedings/neosst1/paper/494/NEOSST1-paper494.pdf.

Baoyin, H. and McInnes, C. R. Solar sail equilibria in the elliptical restricted three-body problem. *Journal of Guidance, Control, and Dynamics*, 29(3):538–543, 2006.

Biggs, J. D., McInnes, C. R., and Waters, T. Control of solar sail periodic orbits in the elliptic three-body problem. *Journal of Guidance, Control, and Dynamics*, 32(1):318–320, 2009.

Bottke, W. F., Morbidelli, A., Jedicke, R., Petit, J.-M., Levison, H. F., Michel, P., and Metcalfe, T. S. Debiased orbital and absolute magnitude distribution of the near-earth objects. *Icarus*, 156(2):399 – 433, 2002. ISSN 0019-1035. doi: https://doi.org/10.1006/icar.2001.6788. URL http://www.sciencedirect.com/science/article/pii/S0019103501967880.

Chesley, S. R. and Spahr, T. B. Earth impactors: orbital characteristics and warning times. *Mitigation of Hazardous Comets and Asteroids*, 22, 2004.

Daniels, G. M. A night sky model for satellite search systems. *Optical Engineering*, 16(1):160166, 1977.

Farnocchia, D., Bernardi, F., and Valsecchi, G. B. Efficiency of a wide-area survey in achieving short-and long-term warning for small impactors. *Icarus*, 219(1):41–47, 2012.

Fernández Mora, A. Solar-sail invariant objects in the Sun-Earth system and transfers to the L5 region. Master's thesis, Delft University of Technology, Delft, The Netherlands, February 2019.

Granvik, M., Morbidelli, A., Jedicke, R., Bolin, B., Bottke, W. F., Beshore, E., Vokrouhlický, D., Nesvorný, D., and Michel, P. Debiased orbit and absolute-magnitude distributions for near-earth objects. *Icarus*, 312: 181 – 207, 2018. ISSN 0019-1035. doi: https://doi.org/10.1016/j.icarus.2018.04.018. URL http://www.sciencedirect.com/science/article/pii/S0019103517307017.

Grav, T., Mainzer, A., Spahr, T., Masiero, J., Bauer, J. M., Cutri, R. M., Kramer, E., and Sonnett, S. NEOCam Survey Cadence and Simulation. In *50th Lunar and Planetary Science Conference 2019 (LPI Contrib. No. 2132) (The Woodlands, Texas, March 1822, 2019)*. 2019.

Harris, A. W. and Lagerros, J. S. Asteroids in the thermal infrared. *Asteroids III*, 205, 2002.

Harris, A. W., Delbó, M., Binzel, R. P., Davies, J. K., Roberts, J., Tholen, D. J., and Whiteley, R. J. Visible to thermal-infrared spectrophotometry of a possible inactive cometary nucleus. *Icarus*, 153(2):332–337, 2001.

Heiligers, J., Diedrich, B., Derbes, W., and McInnes, C. R. Sunjammer: preliminary end-to-end mission design. In *AIAA/AAS Astrodynamics Specialist Conference*, page 4127, 2014.

Howell, K. C. Three-dimensional, periodic, 'halo' orbits. *Celestial mechanics*, 32(1):53–71, 1984.

Kelsall, T., Weiland, J., Franz, B., Reach, W., Arendt, R., Dwek, E., Freudenreich, H., Hauser, M., Moseley, S., Odegard, N., et al. The cobe diffuse infrared background experiment search for the cosmic infrared background. ii. model of the interplanetary dust cloud. *The Astrophysical Journal*, 508(1):44, 1998.

Leinert, C., Bowyer, S., Haikala, L., Hanner, M., Hauser, M., Levasseur-Regourd, A.-C., Mann, I., Mattila, K., Reach, W., Schlosser, W., et al. The 1997 reference of diffuse night sky brightness. *Astronomy and Astrophysics Supplement Series*, 127(1):1–99, 1998.

Lissauer, J. J. and De Pater, I. *Fundamental planetary science: physics, chemistry and habitability*. Cambridge University Press, 2013.

Mainzer, A., Bauer, J., Grav, T., Masiero, J., Cutri, R., Dailey, J., Eisenhardt, P., McMillan, R., Wright, E., Walker, R., et al. Preliminary results from NEOWISE: an enhancement to the wide-field infrared survey explorer for solar system science. *The Astrophysical Journal*, 731(1):53, 2011a.

Mainzer, A., Grav, T., Masiero, J., Bauer, J., Wright, E., Cutri, R., McMillan, R., Cohen, M., Ressler, M., and Eisenhardt, P. Thermal model calibration for minor planets observed with wide-field infrared survey explorer/NEOWISE. *The Astrophysical Journal*, 736(2):100, 2011b.

Mainzer, A., Grav, T., Bauer, J., Conrow, T., Cutri, R., Dailey, J., Fowler, J., Giorgini, J., Jarrett, T., Masiero, J., et al. Survey simulations of a new near-Earth asteroid detection system. *The Astronomical Journal*, 149(5):172, 2015.

McInnes, A. I. Strategies for solar sail mission design in the circular restricted three-body problem. *MSE Thesis, School of Aeronautics and Astronautics, Purdue University*, 2000.

Milam, S., Hammel, H., Bauer, J. M., Brozovic, M., Grav, T., Holler, B. J., Mainzer, A. K., Reddy, V., Schwamb, M. E., Spahr, T. B., et al. Emerging capabilities for detection and characterization of near-earth objects (neos). In *Bulletin of the American Astronomical Society*, volume 51, 2019a.

Milam, S., Hammel, H., Bauer, J. M., Brozovic, M., Grav, T., Holler, B. J., Mainzer, A. K., Reddy, V., Schwamb, M. E., Spahr, T. B., et al. Emerging capabilities for detection and characterization of near-earth objects (neos). In *Bulletin of the American Astronomical Society*, May 2019b. Vol.51, No.3.

Müller, M. Surface properties of asteroids from mid-infrared observations and thermophysical modeling. *arXiv preprint arXiv:1208.3993*, 2012.

Ramirez Torralba, O., Jehn, R., Koschny, D., Frühauf, M., Jehn, L., and Praus, A. Simulation of sky surveys with the Flyeye telescope. In *Proc. 1st NEO and Debris Detection Conference (Darmstadt, Germany, 22-24 January 2019)*. ESA Space Safety Programme Office, 2019. URL https://conference.sdo.esoc.esa.int/proceedings/neosst1/paper/2/NEOSST1-paper2.pdf.

Ramirez Torralba, Olga. Mission analysis of space-based telescopes to detect near-Earth objects, 2019. Literature Study. Delft University of Technology.

Renk, F. and Landgraf, M. Euclid: Esa's dark energy 3-axis stabilized survey mission at the night-side sun-earth libration point. 2014.

Richardson, D. L. Analytic construction of periodic orbits about the collinear points. *Celestial mechanics*, 22 (3):241–253, 1980.

Rodriguez, J. I. Feasibility of passive cryogenic cooling for solar powered outer planetary missions. 47th International Conference on Environmental Systems, 2017.

Shustov, B., Shugarov, A., Naroenkov, S., and Kovalenko, I. System of observation of day-time asteroids (SODA). In *Proc. 1st NEO and Debris Detection Conference (Darmstadt, Germany, 22-24 January 2019)*. ESA Space Safety Programme Office, 2019. URL https://conference.sdo.esoc.esa.int/proceedings/neosst1/paper/439/NEOSST1-paper439.pdf.

Stokes, G. H., Barbee, B. W., Bottke, W. F., Buie, M. W., Chesley, S. R., Chodas, P. W., Evans, J. B., Gold, R. E., Grav, T., Harris, A. W., Jedicke, R., Mainzer, A. K., Mathias, D. L., Spahr, T. B., and Yeomans, D. K. Update to determine the feasibility of enhancing the search and characterization of NEOs. Report of the near-earth object science definition team (2017), National Aeronautics and Space Administration, 2017. URL https://cneos.jpl.nasa.gov/doc/SDT_report_2017.html. Access date 2019-03-14.

Topputo, F., Vasile, M., and Ercoli, A. An approach to the design of low energy interplanetary transfers exploiting invariant manifolds of the restricted three-body problem. In *14th AAS/AIAA Space Flight Mechanics Meeting*, pages 2229–2248. Univelt, 2004.

Vergaaij, M. Time-optimal solar sail transfers from Earth to pole-sitters at Mars and Venus. March 2018. URL http://resolver.tudelft.nl/uuid:f916326f-364b-4d4c-98c1-5bee07c6f7d2.

Wakker, K. *Fundamentals of astrodynamics*. TU Delft Library, January 2015. ISBN 9789461864192.

Waters, T. J. and McInnes, C. R. Periodic orbits above the ecliptic in the solar-sail restricted three-body problem. *Journal of Guidance, Control, and Dynamics*, 30(3):687–693, 2007.